# DYNAMIC LOAD PREDICTON IN OFFSHORE WIND TURBINES by M.K. Rama Pandian November 12, 2021 Beskells

## DYNAMIC LOAD PREDICTION

## In Offshore Wind Turbines

by

M.K. Rama Pandian

to obtain the degree of Master of Science at the Delft University of Technology, to be defended publicly on November 26, 2021 at 13:00 hours.

Student number: 5132622

Project duration: February 1, 2021 - October 29, 2021

Thesis committee:

Prof. Dr. ir. C.S. Ferreira,
Dr. ir. H. Hendrikse,
Dr. ir. W. Yu,
Ir. W. Luites,
Ir. Abhishek,

Prof. Dr. ir. C.S. Ferreira,
TU Delft, Chairman
TU Delft, Supervisor
Boskalis Offshore Heavy Liftin
Boskalis Offshore Heavy Liftin Boskalis Offshore Heavy Lifting Boskalis Offhosre Heavy Lifting

An electronic version of this thesis is available at http://repository.tudelft.nl/.





## Acknowledgements

Firstly, I would like to sincerely thank Professor C.S. Ferreira for his valuable inputs and patient guidance which greatly helped me during the final stages of my thesis. I am extremely grateful for the guidance provided by my university supervisor Wei Yu as her constant feedback and suggestions helped me gain more insights into my thesis as she also encouraged me to think in new directions. I would also like to thank Hayo Hendrikse for accepting the invite to be a member of my thesis committee.

I would like to express my deepest gratitude to my company supervisors, Wout Luites and Abhishek for devoting their time to help me develop my knowledge and understanding regarding concepts related to structures. Their constant encouragement pushed me to perform better and they also played a crucial role in helping me gain experience in Python, FEMAP and openFAST. I would further like to thank the entire design team of Boskalis, especially the manager of the team Maarten van der Veen for his support and the rest of the colleagues at Boskalis for the friendly and fun working environment.

Finally, this wonderful yet challenging journey would not have been possible without the support of my family and friends. I am extremely grateful to my parents and my sister for playing their part in helping me pursue and achieve my goals and for always believing in me.

M.K. Rama Pandian Delft, November 2021

## **Abstract**

The rapid development of the wind industry over the past few years has pushed turbine manufacturers to meet the growing energy demands by designing and producing large scale wind turbines. This also means development of larger monopile foundations for the foundation designers in the case of offshore wind turbines. Generally, the turbine tower and monopile are modeled together and the loads from the rotor-nacelle assembly are provided by turbine manufacturers. The offshore industry is now showing more interest in extracting the loads from the top mass by developing their own tools in order to reduce the dependency on the manufacturers. In order to aid in this process, the present master thesis aims to develop a linear model based on the concept of Dynamic Substructuring which employs a set of equations to compute the interface forces using the kinematics. Furthermore, the developed prediction model is used to analyze the loads occurring at the interface between the rotor-nacelle assembly and the tower for different wind speeds and wind conditions. Consequentially, the model was found to produce acceptable loads at higher wind speeds for selected degrees of freedom at the interface while failing to do the same for other degrees of freedom. The results in time domain were converted to the frequency domain to analyse the resonance. The influence of resonance on the interface degrees of freedom was found to be higher at wind speed below the rated condtion. These findings can be used as a basis to conduct further investigations into the application of numerical integration concepts to aeroelastic structures.

## Contents

Lis	st of Figures	V
Lis	st of Tables	vii
1	Introduction 1.1 Problem Definition	3 3
2	LITERATURE STUDY  2.1 Dynamic Substructuring	6 7 8 8 8 8
3	Model Development         3.1 Prediction Model	<b>12</b> 13
4	RESULTS AND VALIDATION  4.1 Validation of Prediction Model	17 18 19 20 22 23 24 25 27
5	CONCLUSION & RECOMMENDATIONS  5.1 Conclusion	<b>29</b> 30
Bil	bliography	31
A	Construction of Boolean Matrix	33
В	Impulse Response Model	35
С	Time Integration using Newmark Method	38
D	Tower Information	42
F	Structure used for validation	45

Contents

F	Method for Input Extraction         F.0.1       Extraction of External Aeroelastic Loads	
G	Results for other cases G.1 Case 1.3: Average wind speed 11.40 m/s	54 56

# List of Figures

1.1 1.2 1.3	Expected growth of Offshore Wind [13]	1 2 3
2.1 2.2 2.3 2.4 2.5	Classification of Dynamic Substructuring [27] Assembly Unit Impulse at time t=0 [8] Structure and work flow of openFAST [2] Centers of Mass - RNA	6 7 9 10 11
3.1	Prediction Model algorithm	13
4.1 4.2 4.3	Validation structure	15 16
4.4 4.5 4.6 4.7	from openFAST	18 19 19 20 21
4.11	Frequency Domain - DoF Fy	21 23 23 24
4.13 4.14 4.15 4.16 4.17	External Aeroelastic Load at an average wind speed of 23.64 m/s from openFAST Time Domain - Interface DoF Fy and Mz for 23.64 m/s	24 25 25 26 26 27 28
	Coupling of two substructures [31]	33
B.1	Impulse Response model algorithm [28]	36
C.1	Newmark scheme for linear systems [22]	40
D.2	Finite Element Model - NREL5MW Tower	43 44 44
	Finite Element Model - Validation structure	45 46
F.1 F.2	Process Flowchart	47 49
	Time Domain and Frequency Domain - DoF Fx	52 53

List of Figures vi

G.3	Time D	Domain	and	Frequenc	y Domain	- DoF	Mx									53
G.4	Time D	Domain	and	Frequenc	y Domain	- DoF	Му									54
G.5	Time D	Domain	and	Frequenc	y Domain	- DoF	Fx									54
G.6	Time D	Domain	and	Frequenc	y Domain	- DoF	Fz									55
G.7	Time D	Domain	and	Frequenc	y Domain	- DoF	Mx									55
G.8	Time D	Domain	and	Frequenc	y Domain	- DoF	My									56
G.9	Time D	Domain	and	Frequenc	y Domain	- DoF	Fx									56
G.10	Time D	Domain	and	Frequenc	y Domain	- DoF	Mx									57
G.11	Time D	Domain	and	Frequenc	y Domain	- DoF	My									57
G.12	Time D	Domain	and	Frequenc	y Domain	- DoF	Fx									58
G.13	Time D	Domain	and	Frequency	y Domain	- DoF	Fz									58
G.14	Time D	Domain	and	Frequenc	y Domain	- DoF	Mx									59
G.15	Time D	Domain	and	Frequenc	y Domain	- DoF	My									59

## **List of Tables**

4.1	List of Nodes - Substructures	16
4.2	Validation	17
4.3	Test Case	17
4.4	Statistical comparison : openFAST(orange) vs Prediction Model(blue) - Test Case 1	18
4.5		20
4.6	Statistical comparison : openFAST(orange) vs Prediction Model(blue)	22
4.7		
4.8	Simulation Case parameters	22
C.1	Newmark Family of Methods [10]	39
D.1	List of Nodes - NREL 5MW Tower	42
	List of Elements - NREL 5MW Tower	
E.1	List of Nodes - Hollow Cylinder	46
F.1 F.2	TurbSim parameters for a turbulent wind field with an average wind speed of 11.4 m/s . Linearization parameters for rated wind speed of 11.4 m/s	

## **Abbreviations**

**CMS** Component Mode Synthesis

**DLC** Design Load Case

**DS** Dynamic Substructuring

FBS Frequency Based Substructuring

FD Foundation Designer

FRFs Frequency Response Functions

**IBS** Impulse Based Substructuring

IEC International Electrotechnical Commission

IRFs Impulse Response Functions

MW Mega Watt

NREL National Renewable Energy Laboratory

**OWTs** Offshore Wind Turbines

PDT Python Design Tool

RNA Rotor-Nacelle Assembly

WTM Wind Turbine Manufacturer

# List of Symbols

M Mass matrix  C Damping matrix  K Stiffness matrix  f External force $u, u(t)$ displacement $\dot{u}, \dot{u}(t)$ velocity $\ddot{u}, \ddot{u}(t)$ acceleration $(rna)$ related to RNA $(sub)$ related to tower  B Boolean matrix $u_b, f_b$ Displacement and force at interface node $\dot{u}_b$ Interface force vector $\dot{u}_b$ Impulse Response Matrix(at time t) $\dot{u}_b$ , $\dot{u}_b$ Displacement, velocity and acceleration at $n^{th}$ time step $\dot{u}_n$ , $\dot{u}_n$ , $\dot{u}_n$ Displacement, velocity and acceleration at t=0 $\dot{u}_b$ , $\dot{u}_b$ Dirac-delta function $\dot{u}_b$ , $\dot{u}_b$ Initial displacement, velocity and acceleration at t=0 $\dot{u}_b$ , $\dot{u}_a$ Predicted displacement and velocity at $n^{th}$ time step $\dot{v}_b$ Newmark constants $\dot{u}_n$ Uncoupled displacement at $n^{th}$ time step		
$K$ Stiffness matrix $f$ External force $u,u(t)$ displacement $\dot{u},\dot{u}(t)$ velocity $\ddot{u},\ddot{u}(t)$ velocity $\ddot{u},\ddot{u}(t)$ acceleration related to RNA related to tower $B$ Boolean matrix $u_b,f_b$ Displacement and force at interface node $\lambda$ Interface force vector $H(s)$ Transfer function $s$ Laplace variable $H(t)$ Impulse Response Matrix(at time t) $u_n,\dot{u}_n,\ddot{u}_n$ Displacement, velocity and acceleration at $n^{th}$ time step $H_n$ Impulse Response Matrix at $n^{th}$ time step $h_n$ Force at $n^{th}$ time step $h_n$ Force at $n^{th}$ time step $h_n$ Dirac-delta function $h_n(t)$ Dirac-delta	М	Mass matrix
$f$ External force $u,u(t)$ displacement $\dot{u},\dot{u}(t)$ velocity $\ddot{u},\ddot{u}(t)$ velocity $\ddot{u},\ddot{u}(t)$ acceleration $(rna)$ related to RNA $(sub)$ related to tower $B$ Boolean matrix $u_b,f_b$ Displacement and force at interface node $\lambda$ Interface force vector $H(s)$ Transfer function $s$ Laplace variable $H(t)$ Impulse Response Matrix(at time t) $u_n,\dot{u}_n,\ddot{u}_n$ Displacement, velocity and acceleration at $n^{th}$ time step $H_n$ Impulse Response Matrix at $n^{th}$ time step $f_n$ Force at $n^{th}$ time step $\delta(t)$ Dirac-delta function $u_0,\dot{u}_0,\ddot{u}_0$ Initial displacement, velocity and acceleration at $t=0$ $dt$ Time interval $\dot{u}_n,\dot{u}_n$ Predicted displacement and velocity at $n^{th}$ time step $\gamma,\beta$ Newmark constants	С	Damping matrix
u,u(t) displacement $u,u(t)$ velocity $u,u(t)$ velocity $u,u(t)$ acceleration $u,u(t)$ acceleration related to RNA related to tower $u,u(t)$ Displacement and force at interface node $u,u(t)$ Interface force vector $u,u(t)$ Impulse Response Matrix(at time t) $u,u(t)$ Displacement, velocity and acceleration at $u,u(t)$ Impulse Response Matrix at $u,u($	K	Stiffness matrix
$\ddot{u}, \ddot{u}(t)$ velocity $\ddot{u}, \ddot{u}(t)$ acceleration (rna) related to RNA (sub) related to tower B Boolean matrix $u_b, f_b$ Displacement and force at interface node $\lambda$ Interface force vector $H(s)$ Transfer function $s$ Laplace variable $H(t)$ Impulse Response Matrix(at time t) $u_n, \dot{u}_n, \ddot{u}_n$ Displacement, velocity and acceleration at $n^{th}$ time step $f_n$ Force at $n^{th}$ time step $\delta(t)$ Dirac-delta function $u_0, \dot{u}_0, \ddot{u}_0$ Initial displacement, velocity and acceleration at $t=0$ $t$	f	External force
$\ddot{u},\ddot{u}(t)$ acceleration $(rna)$ related to RNA $(sub)$ related to tower $B$ Boolean matrix $u_b,f_b$ Displacement and force at interface node $\lambda$ Interface force vector $H(s)$ Transfer function $s$ Laplace variable $H(t)$ Impulse Response Matrix(at time t) $u_n,\ddot{u}_n,\ddot{u}_n$ Displacement, velocity and acceleration at $n^{th}$ time step $H_n$ Impulse Response Matrix at $n^{th}$ time step $f_n$ Force at $n^{th}$ time step $\delta(t)$ Dirac-delta function $u_0,\ddot{u}_0,\ddot{u}_0$ Initial displacement, velocity and acceleration at $t=0$ $dt$ Time interval $\dot{u}_n,\dot{u}_n$ Predicted displacement and velocity at $n^{th}$ time step $\gamma,\beta$ Newmark constants	u,u(t)	displacement
related to RNA  (sub) related to tower  B Boolean matrix $u_b, f_b$ Displacement and force at interface node $\lambda$ Interface force vector $H(s)$ Transfer function $s$ Laplace variable $H(t)$ Impulse Response Matrix(at time t) $u_n, \dot{u}_n, \ddot{u}_n$ Displacement, velocity and acceleration at $n^{th}$ time step $H_n$ Impulse Response Matrix at $n^{th}$ time step $f_n$ Force at $n^{th}$ time step $\delta(t)$ Dirac-delta function $u_0, \dot{u}_0, \ddot{u}_0$ Initial displacement, velocity and acceleration at $t=0$ $dt$ Time interval $\dot{u}_n, \dot{u}_n$ Predicted displacement and velocity at $n^{th}$ time step $\gamma, \beta$ Newmark constants	$\dot{u},\dot{u}(t)$	velocity
related to tower $B$ Boolean matrix $u_b, f_b$ Displacement and force at interface node $\lambda$ Interface force vector $H(s)$ Transfer function $s$ Laplace variable $H(t)$ Impulse Response Matrix(at time t) $u_n, \dot{u}_n, \ddot{u}_n$ Displacement, velocity and acceleration at $n^{th}$ time step $H_n$ Impulse Response Matrix at $n^{th}$ time step $f_n$ Force at $n^{th}$ time step $\delta(t)$ Dirac-delta function $u_0, \dot{u}_0, \ddot{u}_0$ Initial displacement, velocity and acceleration at $t=0$ $dt$ Time interval $\dot{u}_n, \dot{u}_n$ Predicted displacement and velocity at $n^{th}$ time step $\gamma, \beta$ Newmark constants	$\ddot{u},\ddot{u}(t)$	acceleration
B Boolean matrix $u_b, f_b$ Displacement and force at interface node $\lambda$ Interface force vector $H(s)$ Transfer function $s$ Laplace variable $H(t)$ Impulse Response Matrix(at time t) $u_n, \hat{u}_n, \hat{u}_n$ Displacement, velocity and acceleration at $n^{th}$ time step $H_n$ Impulse Response Matrix at $n^{th}$ time step $f_n$ Force at $n^{th}$ time step $\delta(t)$ Dirac-delta function $u_0, \hat{u}_0, \hat{u}_0$ Initial displacement, velocity and acceleration at t=0 $dt$ Time interval $\hat{u}_n, \hat{u}_n$ Predicted displacement and velocity at $n^{th}$ time step $\gamma, \beta$ Newmark constants	(rna)	related to RNA
$\begin{array}{lll} u_b, f_b & \text{Displacement and force at interface node} \\ \lambda & \text{Interface force vector} \\ H(s) & \text{Transfer function} \\ s & \text{Laplace variable} \\ H(t) & \text{Impulse Response Matrix(at time t)} \\ u_n, \dot{u}_n, \ddot{u}_n & \text{Displacement, velocity and acceleration at } n^{th} \text{ time step} \\ H_n & \text{Impulse Response Matrix at } n^{th} \text{ time step} \\ f_n & \text{Force at } n^{th} \text{ time step} \\ \delta(t) & \text{Dirac-delta function} \\ u_0, \dot{u}_0, \ddot{u}_0 & \text{Initial displacement, velocity and acceleration at t=0} \\ dt & \text{Time interval} \\ \dot{u}_n, \dot{u}_n & \text{Predicted displacement and velocity at } n^{th} \text{ time step} \\ \gamma, \beta & \text{Newmark constants} \\ \end{array}$	(sub)	related to tower
$\begin{array}{lll} \lambda & & \text{Interface force vector} \\ H(s) & & \text{Transfer function} \\ s & & \text{Laplace variable} \\ H(t) & & \text{Impulse Response Matrix(at time t)} \\ u_n, \dot{u}_n, \ddot{u}_n & & \text{Displacement, velocity and acceleration at } n^{th} \text{ time step} \\ H_n & & \text{Impulse Response Matrix at } n^{th} \text{ time step} \\ f_n & & \text{Force at } n^{th} \text{ time step} \\ \delta(t) & & \text{Dirac-delta function} \\ u_0, \dot{u}_0, \ddot{u}_0 & & \text{Initial displacement, velocity and acceleration at t=0} \\ dt & & \text{Time interval} \\ \dot{u}_n, \dot{u}_n & & \text{Predicted displacement and velocity at } n^{th} \text{ time step} \\ \gamma, \beta & & \text{Newmark constants} \\ \end{array}$	В	Boolean matrix
$H(s)$ Transfer function $s$ Laplace variable $H(t)$ Impulse Response Matrix(at time t) $u_n, \dot{u}_n, \ddot{u}_n$ Displacement, velocity and acceleration at $n^{th}$ time step $H_n$ Impulse Response Matrix at $n^{th}$ time step $f_n$ Force at $n^{th}$ time step $\delta(t)$ Dirac-delta function $u_0, \dot{u}_0, \ddot{u}_0$ Initial displacement, velocity and acceleration at t=0 $dt$ Time interval $\hat{u}_n, \hat{u}_n$ Predicted displacement and velocity at $n^{th}$ time step $\gamma, \beta$ Newmark constants	$u_b$ , $f_b$	Displacement and force at interface node
$ \begin{array}{lll} s & \text{Laplace variable} \\ H(t) & \text{Impulse Response Matrix(at time t)} \\ u_n, \dot{u}_n, \ddot{u}_n & \text{Displacement, velocity and acceleration at } n^{th} \text{ time step} \\ H_n & \text{Impulse Response Matrix at } n^{th} \text{ time step} \\ f_n & \text{Force at } n^{th} \text{ time step} \\ \delta(t) & \text{Dirac-delta function} \\ u_0, \dot{u}_0, \ddot{u}_0 & \text{Initial displacement, velocity and acceleration at t=0} \\ dt & \text{Time interval} \\ \dot{u}_n, \dot{u}_n & \text{Predicted displacement and velocity at } n^{th} \text{ time step} \\ \gamma, \beta & \text{Newmark constants} \\ \end{array} $	λ	Interface force vector
$H(t) \qquad \text{Impulse Response Matrix} (\text{at time t}) \\ u_n, \dot{u}_n, \ddot{u}_n \qquad \text{Displacement, velocity and acceleration at } n^{th} \text{ time step} \\ H_n \qquad \text{Impulse Response Matrix at } n^{th} \text{ time step} \\ f_n \qquad \text{Force at } n^{th} \text{ time step} \\ \delta(t) \qquad \text{Dirac-delta function} \\ u_0, \dot{u}_0, \ddot{u}_0 \qquad \text{Initial displacement, velocity and acceleration at t=0} \\ dt \qquad \text{Time interval} \\ \dot{u}_n, \dot{u}_n \qquad \text{Predicted displacement and velocity at } n^{th} \text{ time step} \\ \gamma, \beta \qquad \text{Newmark constants} \\ \vdots$	H(s)	Transfer function
$u_n, \dot{u}_n, \ddot{u}_n$ Displacement, velocity and acceleration at $n^{th}$ time step $H_n$ Impulse Response Matrix at $n^{th}$ time step $f_n$ Force at $n^{th}$ time step $\delta(t)$ Dirac-delta function $u_0, \dot{u}_0, \ddot{u}_0$ Initial displacement, velocity and acceleration at t=0 $dt$ Time interval $\hat{u}_n, \hat{u}_n$ Predicted displacement and velocity at $n^{th}$ time step $\gamma, \beta$ Newmark constants	S	Laplace variable
$H_n$ Impulse Response Matrix at $n^{th}$ time step $f_n$ Force at $n^{th}$ time step $\delta(t)$ Dirac-delta function $u_0, \dot{u}_0, \ddot{u}_0$ Initial displacement, velocity and acceleration at t=0 $dt$ Time interval $\hat{u}_n, \hat{u}_n$ Predicted displacement and velocity at $n^{th}$ time step $\gamma, \beta$ Newmark constants	H(t)	Impulse Response Matrix(at time t)
$f_n$ Force at $n^{th}$ time step $\delta(t)$ Dirac-delta function $u_0, \dot{u}_0, \ddot{u}_0$ Initial displacement, velocity and acceleration at t=0 $dt$ Time interval $\hat{u}_n, \hat{u}_n$ Predicted displacement and velocity at $n^{th}$ time step $\gamma, \beta$ Newmark constants	$u_n, \dot{u}_n, \ddot{u}_n$	Displacement, velocity and acceleration at $n^{th}$ time step
$\delta(t)$ Dirac-delta function $u_0, \dot{u}_0, \ddot{u}_0$ Initial displacement, velocity and acceleration at t=0 $dt$ Time interval $\hat{u}_n, \hat{u}_n$ Predicted displacement and velocity at $n^{th}$ time step $\gamma, \beta$ Newmark constants	$H_n$	Impulse Response Matrix at $n^{th}$ time step
$u_0, \dot{u}_0, \ddot{u}_0$ Initial displacement, velocity and acceleration at t=0 $dt$ Time interval $\hat{u}_n, \hat{u}_n$ Predicted displacement and velocity at $n^{th}$ time step $\gamma, \beta$ Newmark constants	$f_n$	Force at $n^{th}$ time step
$dt$ Time interval $\hat{u}_n, \hat{u}_n$ Predicted displacement and velocity at $n^{th}$ time step $\gamma, \beta$ Newmark constants	$\delta(t)$	Dirac-delta function
$\hat{u}_n, \hat{u}_n$ Predicted displacement and velocity at $n^{th}$ time step $\gamma, \beta$ Newmark constants	$u_0$ , $\dot{u}_0$ , $\ddot{u}_0$	Initial displacement, velocity and acceleration at t=0
$\gamma, \beta$ Newmark constants	dt	Time interval
	$\hat{u}_n$ , $\hat{\dot{u}}_n$	Predicted displacement and velocity at $n^{th}$ time step
$ ilde{u}_n$ Uncoupled displacement at $n^{th}$ time step	γ,β	Newmark constants
	$ ilde{u}_n$	Uncoupled displacement at $n^{th}$ time step

## Introduction

The wind industry is currently facing rapid development with turbine manufacturers moving to larger scale wind turbines in order to meet the increasing energy demand while achieving the climate goals. Even though the cost of offshore wind may be higher, the availability of space deems it an attractive prospect since more space means larger turbines can be installed. Offshore wind also has its disadvantages in the fact that new infrastructure is required to transmit the electricity produced to the onshore grid and maintenance takes longer as they are relatively harder to perform.

#### Offshore wind Existing | Expected Global weighted average Upcoming turbine models turbine dimensions 20 15-20 MW RD>230.00 m Turbine ratings (MW) 15 12.0 MW RD=220.00 m 10 MW RD=164 00 m 10 5.5 MW RD=148 m 3.0 MW 5 1.6 MW RD=94.43 m RD=43.73 m \* 0 2000 2010 2019-20 2021-25 2025-30

Figure 1.1: Expected growth of Offshore Wind [13]

However, a study conducted by IRENA [13] (*figure 1.1*) shows the progress is on track as turbine manufacturers such as Vestas and Siemens are already moving towards 15MW offshore turbines. Since the rotor diameter and hub height increase with the rated power of the turbine, the challenge with such huge turbines is that they experience higher loads because the wind speeds also increase with increasing heights. Additionally, the gravity loading becomes more dominant since the total mass of the rotor-nacelle assembly(RNA) is larger.

#### 1.1. Problem Definition

Traditionally, the design of offshore wind turbines involves two main parties, the Foundation Designer (FD) and the Wind Turbine Manufacturer (WTM). The WTM is responsible for running simulations for the wind turbine model and the FD runs simulations on models of the foundation structures, with both parties requiring environmental site data at the specified location. According to [20], the simulations performed

1.1. Problem Definition 2

by the WTM involve a simplified version of the rotor-nacelle assembly (RNA) while the WTM runs simulations with a simplified representation of the foundation. This typical process is further elaborated in [30] as :

- The FD creates an initial design of the support structure based on soil data, water depth and the generic loads provided by the WTM.
- The initial design is then passed on to the WTM along with associated wave loads. The WTM
  couples the initial foundation design with the offshore wind turbine to run an integrated aeroelastic simulation for various load cases.
- Based on the obtained results, the tower design is updated if needed, based on the extent to which it meets the design criteria and finally, the extracted interface forces and displacements are passed on to the FD.
- The FD applies these load and displacement values accompanied with wave loads to check if it satisfies the design criteria. If the design fails to satisfy the criteria, the foundation design is modified and leads to a repetition of the above steps. This is shown in figure 1.2.

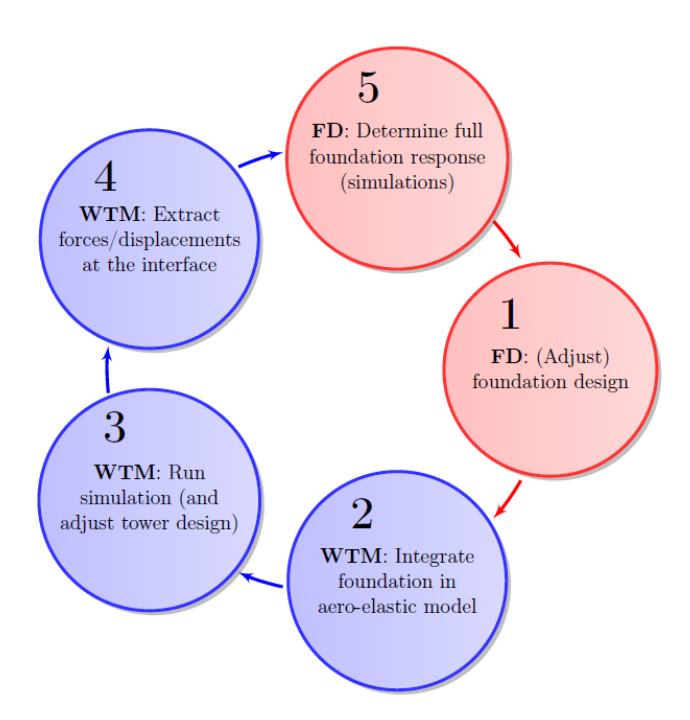


Figure 1.2: Typical Design Cycle of OWTs Foundation [30]

The procedure mentioned in the above figure could lead to issues or complications during the project. They may result from the following actions :

- Unwillingness of both parties to share confidential or intellectual information about their design or design tools.
- The interaction between the parties is time-consuming and there is a high probability for errors to occur.
- The softwares used by the parties might be incompatible and if that is the case, the project might be delayed.

Additionally, with the market becoming more competitive with growing investments in renewable energy sources and with WTMs moving towards larger turbines, the application of generic loads to design foundations, as mentioned in the above design cycle becomes highly error prone. Therefore, a need

1.2. Goals 3

arises to develop a better approach or a model to help predict the loads and displacements at the interface with certain level of accuracy so that the WTM can save more time during the design process and need not depend on the WTM for the data.

#### 1.2. Goals

This study aims to solve the aforementioned problems by developing a model that predicts the load at the interface. The model is further used to predict the load levels for different wind speeds and wind conditions at the interface and assess the effect of resonance at the interface degrees of freedom. In order to achieve these goals, the NREL 5MW wind turbine is chosen in this research.

#### 1.3. Proposed Approach

Generally, openFAST is one of the widely used softwares in academia for analysing and conducting research on wind turbines as it is open-source and reliable. It consists of complex algorithms that are used to compute the dynamic behavior of turbines for different load cases.

The model is constructed based on the concept of Dynamic Substructuring which works on the principle of decoupling a structure into two or more substructures and computing their responses, both uncoupled and coupled in addition to the forces at the interface. The point of decoupling depends on the interface position.

There are many interfaces in a wind turbine between various components, but the one considered in this study is present at the top between the RNA and tower as shown in figure 1.3, which suggests that the RNA is taken as a separate substructure and the tower as a second substructure.



Figure 1.3: Interface Position [1]

Once the model is validated, it is employed in the second phase of the project where load levels at the interface position are analyzed for different wind speeds and wind conditions during which only external aeroelastic loads due to the wind is taken into account. Furthermore, the inputs related to the RNA are extracted from openFAST.

1.4. Overview 4

#### 1.4. Overview



• Chapter 2 provides a brief introduction to the method of Dynamic Substructuring and presents information about concepts related to the model.

- Chapter 3 discusses the development of the model based on the literature and also provides insight into the procedure followed to extract inputs related to both the substructures.
- Chapter 4 presents the resulting load levels at different wind conditions and a discussion of their outlook is carried out.
- Chapter 5 highlights the conclusion based on the observed results and suggests recommendations for further research.

### LITERATURE STUDY



This chapter presents supporting literature for model development discussed in the later stages. It introduces the concept of Dynamic Substructuring. Firstly, it gives a basic description of Dynamic Substructuring and the various advantages that come with employing this approach. Secondly, it lists out the different domains in which this methodology is used and finally, the general procedure for chosen approach within the DS method is explained. Finally,the role of openFAST in this research is also highlighted.

#### 2.1. Dynamic Substructuring

Dynamic Substructuring (DS) is a method that is used to compute the dynamic behaviour of a structure by decoupling it into two or more substructures. It has a great significance in the field of Structural Dynamics as it includes a collection of various sub-methods to study the dynamic behavior of complex structures by dividing them into substructures. These substructures are assessed independently to get their dynamic properties and then re-assembled to analyze the dynamic behavior of the total structure as shown in [23] and [31]. The DS analyses is carried out by using either experimental data or numerical models of the system. The reasons why DS is a suitable method for studying complex systems under dynamic conditions are as follows [30]:

- It gives insight into the dynamic behavior of local components and their effect on the total system which allows for better optimization.
- It enables modelling and analysis of large structures that are difficult to simulate as a whole.
- It allows for the possibility to combine numerical or analytical models with experimental data.
- · More importantly, it allows sharing of substructures between different parties.

According to [8], the origins of dynamic substructuring are related to the field of domain decomposition, where the complex problems are divided into problems of its individual components and finding the interface solution. The DS approach anatomically comprises analyses in four distinct domains namely the :

**Physical Domain**: The structure is represented by its equation of motion where it is characterized by its mass, stiffness and damping matrices.

**Frequency Domain :** The structure is modelled in terms of its Frequency Response Functions (FRFs). This is explained further in Section 2.3.1

**Modal Domain :** The dynamic response of the structure is interpreted based on its modal responses, i. e. the contribution of different mode shapes to the response and amplitude of each mode shape. This is elaborated upon in Section 2.3.2

**Time Domain :** The response of the structure is analyzed using Impulse Response Functions (IRFs) and is expanded in Section 2.3.3

An added advantage of using the DS approach is that it is flexible in the sense that the analysis between the different domains is interchangeable or to be more exact, compatible. For example, the FRFs in Frequency domain are transformed into IRFs in Time Domain by taking the inverse Laplace or Fourier transform of the FRFs [26], [25].

#### 2.2. General Procedure for DS Analysis

This section gives an overview regarding the general procedure that is relative to all the various methods discussed in the next section.

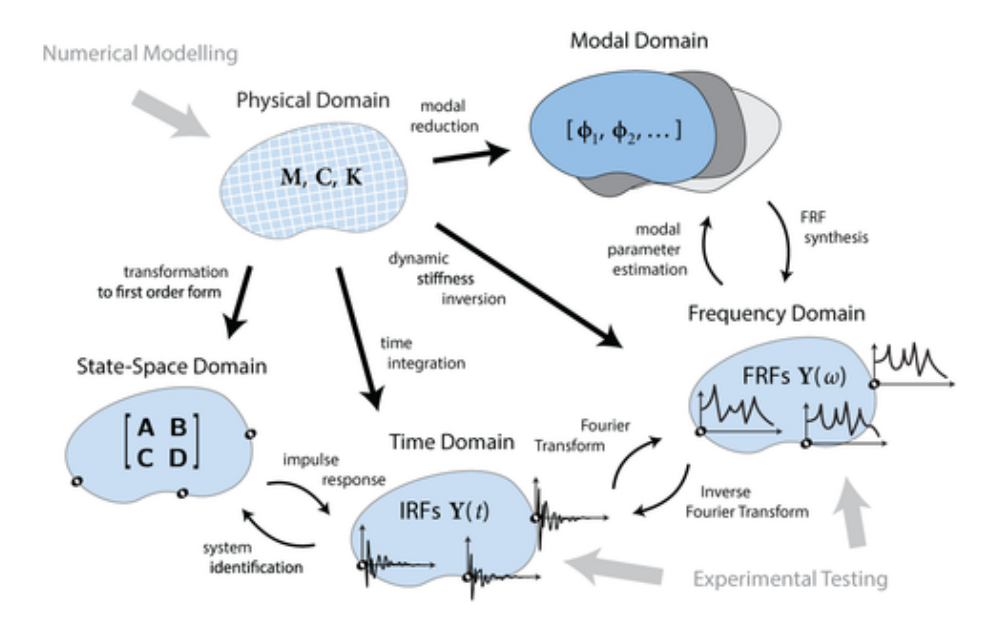


Figure 2.1: Classification of Dynamic Substructuring [27]

Figure 2.1 shows the various approaches using the DS methodology. It also justifies the flexibility of the method mentioned in the previous section, showing that a problem in one domain can be transformed into a problem in another domain. This section further explains the procedure that is usually followed during the implementation of this approach. The selected domain to perform the analysis in this study is the time domain.

#### 2.2.1. Equation of Motion

The first step in the analysis begins with the linear equations of motion of the substructures. For a linear structure, this is in the form of :

$$M\ddot{u} + C\dot{u} + Ku = f(t) \tag{2.1}$$

Where M, C and K denote the mass, damping and stiffness matrices and f represents the external excitation force acting on the system. The reason for opting for a linear system is due to the simplicity of computation.

#### 2.2.2. Conditions

Once the required equations of the substructures are in place, the second step is to ensure that the interface of the substructures satisfy the following conditions :

**Compatibility condition:** It states that the displacement of the interface nodes of substructures must be equal (refer Appendix A), implying that there should be no gap between the substructures [29]:

$$u_b^r = u_b^s \tag{2.2}$$

where [b] denotes the interface nodes. This requirement is expressed using signed Boolean operators which represent the interface DoFs [29] such that :

$$\begin{bmatrix} B^{(rna)} & B^{(sub)} \end{bmatrix} \begin{bmatrix} u^{(rna)} \\ u^{(sub)} \end{bmatrix} = Bu = 0$$
 (2.3)

where  $B^{(rna)}$  and  $B^{(sub)}$  represent the Boolean matrices related to the RNA and tower respectively.

**Equilibrium condition**: The equilibrium condition requires that the sum of forces at the connecting interface nodes must be equal to zero [29], meaning the forces must be equal in magnitude but opposite in direction or sign:

$$f_b^{(rna)} + f_b^{(sub)} = 0 (2.4)$$

Similar to compatibility, this is expressed in Boolean form as:

$$\begin{bmatrix} f_b^{(rna)} \\ f_b^{(sub)} \end{bmatrix} = -B^T \lambda$$
(2.5)

where  $\lambda$  known as Lagrange Multipliers denote the magnitude of the interface forces. The purpose of integrating these conditions in the analysis makes sure the substructures are firmly attached to each other during the coupling process which ensures accurate response of the total system.

The construction of Boolean matrices is included in Appendix A.

#### 2.2.3. Assembly

The (re-)assembly of the substructure equations of motion consists of two types: Primal assembly and Dual assembly. The assembling step is carried out after deriving the Boolean matrix at the interface. The primal assembly is mainly based on the Compatibility equation where the displacement vector consists of only the interface degrees of freedom. In the case of dual assembly, the equilibrium condition also comes into play and the dual assembled system accounts for both the interface forces and displacement by retaining the global set of DoFs of a substructure [8].

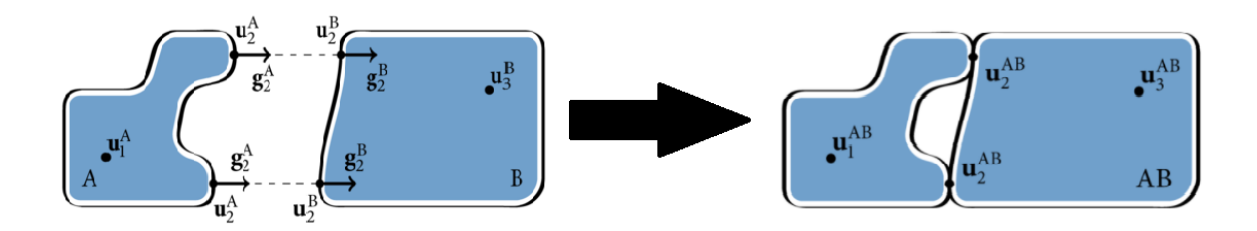


Figure 2.2: Assembly

The final step before running the simulation involves coupling the substructures as shown in figure 2.2. It displays decoupled substructures on the left where  $u_2^A$  and  $u_2^B$  are the interface nodes on either side

with  $g_2^A$  and  $g_2^B$  being the interface degrees of freedom that need to be considered based on equation (2.3) to arrive at the coupled structure on the right. The coupling process depends on the domain in which the problem is initially formulated in and it is further discussed later in section 2.3.3.

#### 2.3. Methods of Dynamic Substructuring

The various concepts of subsystem coupling that exist in DS are classified into three types based on the domain they are performed in. The current section gives a basic overview into the analysis performed in all domains except for Impulse Based Substructuring which happens in time domain as this is basis for developing the model. For this reason, the concepts regarding this method are elaborated later.

#### 2.3.1. Frequency Based Substructuring (FBS)

As mentioned earlier, FBS is carried out in the frequency domain using the Frequency Response Functions (FRFs) of the subsystems. This method uses the FRFs to predict the dynamic behavior of a system and is highly used, especially in the case of experimental substructuring since it is advanced and quite efficient [7]. de Klerk and Rixen [7,8,22] further discuss the evolution and classification of various types of FBS methods.

#### 2.3.2. Component Mode Synthesis (CMS)

Component Mode Synthesis, shortly known as CMS, helps to study the system response in the modal domain. It makes use of different mode shapes to characterise the dynamic behavior and is a projection of the physical problem but applies model reduction to limit the number of DoFs considered in the analysis. It also gives insight into the contribution of each mode shape to the total response of the system. van der Valk [30] and He [12] extensively highlight the procedure and methods under CMS of which the Craig-Bampton method is still widely used.

#### 2.3.3. Impulse Based Substructuring

The IBS analysis is possible by directly formulating the problem in time domain or converting it from frequency domain but it requires a large frequency bandwidth to account for the effect of loads on the structure, due to which the entire procedure becomes computationally expensive [11]. In order to overcome this issue, a method known as Impulse Based Substructuring has been developed. The IBS method involves simulations in the time domain where the frequency response functions are converted to Impulse Response Functions (IRFs) by applying inverse Laplace transform of the frequency problem. The principle behind the IBS approach traces back to the concept of Convolution integral which states that an external load on a linear system is considered as a summation of impacts modeled as unit impulses [11].

van den Bosch [25] and He [12] discuss in detail the concepts based on which the convolution integral is derived from the equation of motion as it is represented either analytically or mathematically. Additionally, van der Valk [30] and Haghighat [11] argue that it is preferable to work with the mathematical formulation and establish a basis to derive the expression to compute the displacement.

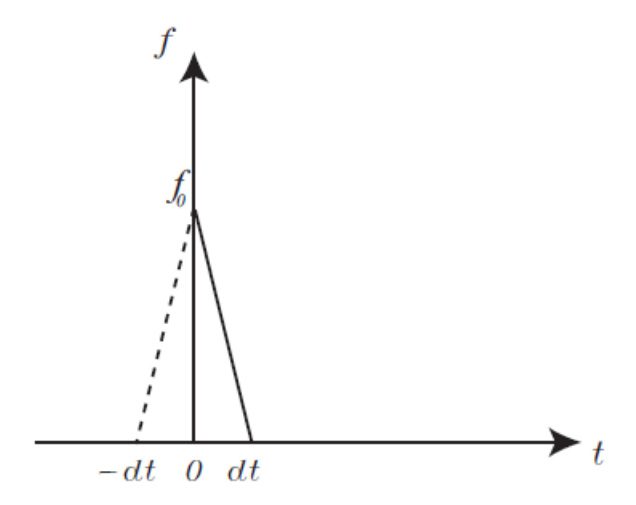


Figure 2.3: Unit Impulse at time t=0 [8]

According to de Klerk [8] and Haghighat [11], the definition of impulse corresponds to figure 2.3 which is used as a reference to devise three different initial conditions namely:

- · Initial velocity
- Initial Applied Force
- Applied Force at Second Time Step

based on which the IBS analysis can be performed. Rixen [22] further employs the approach of Initial Applied Force to present a generalized procedure to assemble the set of equations that enable the computation of displacements and interface forces. Furthermore, Rixen [23] and van der Valk [29] also use another method called Constant Average Acceleration Newmark scheme to compute the kinematics and interface forces as this is relatively more straightforward than convolution integral. The concepts and application behind the Newmark family of methods are further explained by Geradin [10] and Subbaraj [24].

#### 2.4. Linearization in openFAST

openFAST [19] is an open source multi-physics aero-hydro-servo-elastic tool that is used to simulate and analyze the coupled dynamic behavior of wind turbines in both onshore and offshore configurations in time domain. The software consists of various modules that are coupled together in the main driver code and the primary input file(. fst) and aid in computing the aerodynamics related to the blades, hydrodynamics related to the offshore substructures, servo dynamics related to the electrical and control systems and the structural dynamics of the blades, tower and also the foundation in the case of offshore turbines. It can also generate the wind field and wave loading for the Design Load Cases(DLCs).

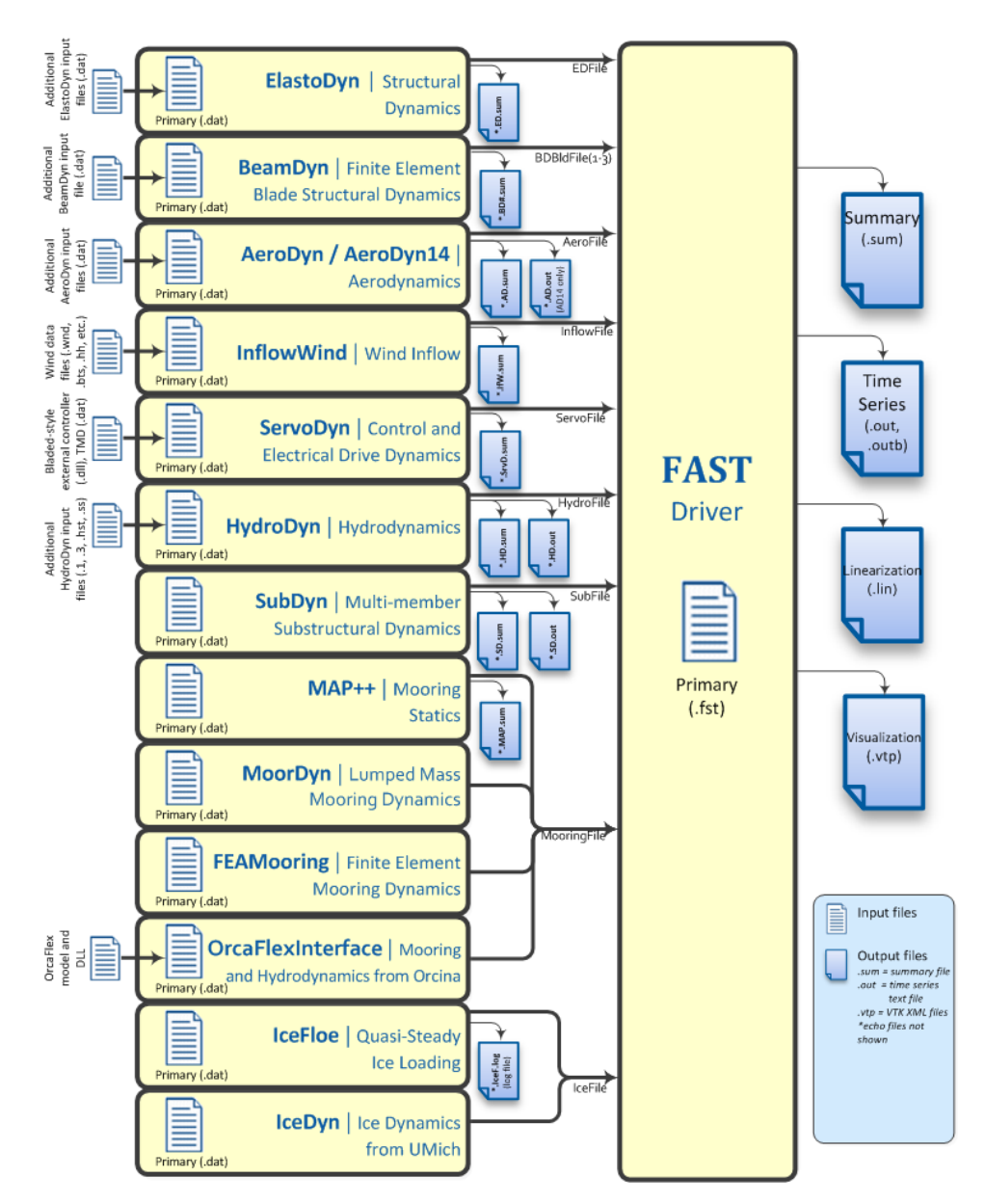


Figure 2.4: Structure and work flow of openFAST [2]

Figure 2.4 shows the various modules present in openFAST. The main modules in focus during the research are the InflowWind [21], AeroDyn [16], ElastoDyn [19] and ServoDyn [19] as they are relevant to the land configuration. Additionally, a stand-alone version of TurbSim [17] is also used to generate the necessary input files for the InflowWind module. Each of these modules contain various input parameters that are adjusted according to the type of simulation being run. In this research, only the land configuration is used since the interface position is at the top and therefore further discussions in this section will provide insight into the four main modules used to simulate the land base turbine.

openFAST also includes a linearization feature apart from non-linear time domain analysis that helps to gain more information about the turbine behavior. The linearization capability enables modal analysis of the turbine while representing it in state-space form by solving complex equations based on different concepts and states as discussed in [14] where the author also states that the process of linearization consists of four steps as follows:

- · Finding an operating point
- · Linearizing the non-linear equation of each module about the operating point

- Linearizing the module-to-module input-output coupling relations in the FAST glue code about the operating point
- · Combining all linearized matrices into a full-system linear state-space model

According to [14], performing linearization with only ElastoDyn module results in structural matrices whereas adding more modules result in matrices with coupled aeroelastics. Furthermore, turning on AeroDyn accounts for the influence of aerodynamic loading. In both cases, the A matrix which is a square matrix among the state-space matrices in the output files contain the mass-generalized stiffness( $M^{-1}K$ ) and mass-generalized damping matrices( $M^{-1}C$ ) as mentioned in [15].

#### 2.5. Construction of Mass Matrix

Based on the discussion in the previous section,the knowledge of mass matrix is required to get the actual stiffness and damping matrices of the RNA. Hence, this section explains the basis on which the mass matrix is formed.

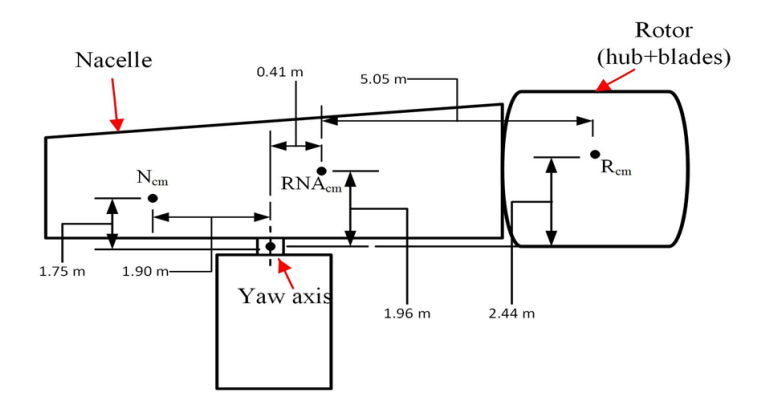


Figure 2.5: Centers of Mass - RNA

The mass matrix is characteristic to a particular structure and they can either be extracted from softwares or be constructed using formulation. The latter approach is chosen in this study as it is relatively straightforward. The formulation for the cross sectional mass matrix based on which the global mass matrix was constructed can be found in equation (4.63) in [19] and [5]:

$$M_{S} = \begin{bmatrix} m & 0 & 0 & 0 & 0 & -mY_{cm} \\ 0 & m & 0 & 0 & 0 & mX_{cm} \\ 0 & 0 & m & mY_{cm} & -mX_{cm} & 0 \\ 0 & 0 & mY_{cm} & I_{xx} & -I_{xy} & 0 \\ 0 & 0 & -mX_{cm} & -I_{xy} & I_{yy} & 0 \\ -mY_{cm} & mX_{cm} & 0 & 0 & 0 & I_{xx} + I_{yy} \end{bmatrix}$$
(2.6)

where m is the mass density in kg/m of the cross section,  $X_{cm}$  and  $Y_{cm}$  are the local coordinates of the sectional center of mass,  $I_{xx}$  and  $I_{yy}$  are the cross section moments of inertia about the x and y axes respectively,  $I_{xy}$  denotes the cross-product between the inertias and  $I_{xx} + I_{yy}$  is the polar moment of inertia.

For the global mass matrix of the RNA, the rotor and hub are considered to be a single element and the nacelle is taken as the second element to form a 9x9 matrix. This approach is used in order to capture the effect of maximum number of DoFs during linearization and to match the size of the mass-generalized matrices. Consequentially,the mass density is replaced with the total mass of the structure while the inertias are calculated about the RNA center of mass in the global coordinate system as shown in figure 2.5. The information on these centers of mass is provided in the turbine document [18].



## Model Development



This chapter provides insight into the evolution of the *Prediction Model* from the Impulse Response Model discussed in Appendix-B.

3.1. Prediction Model 13

#### 3.1. Prediction Model

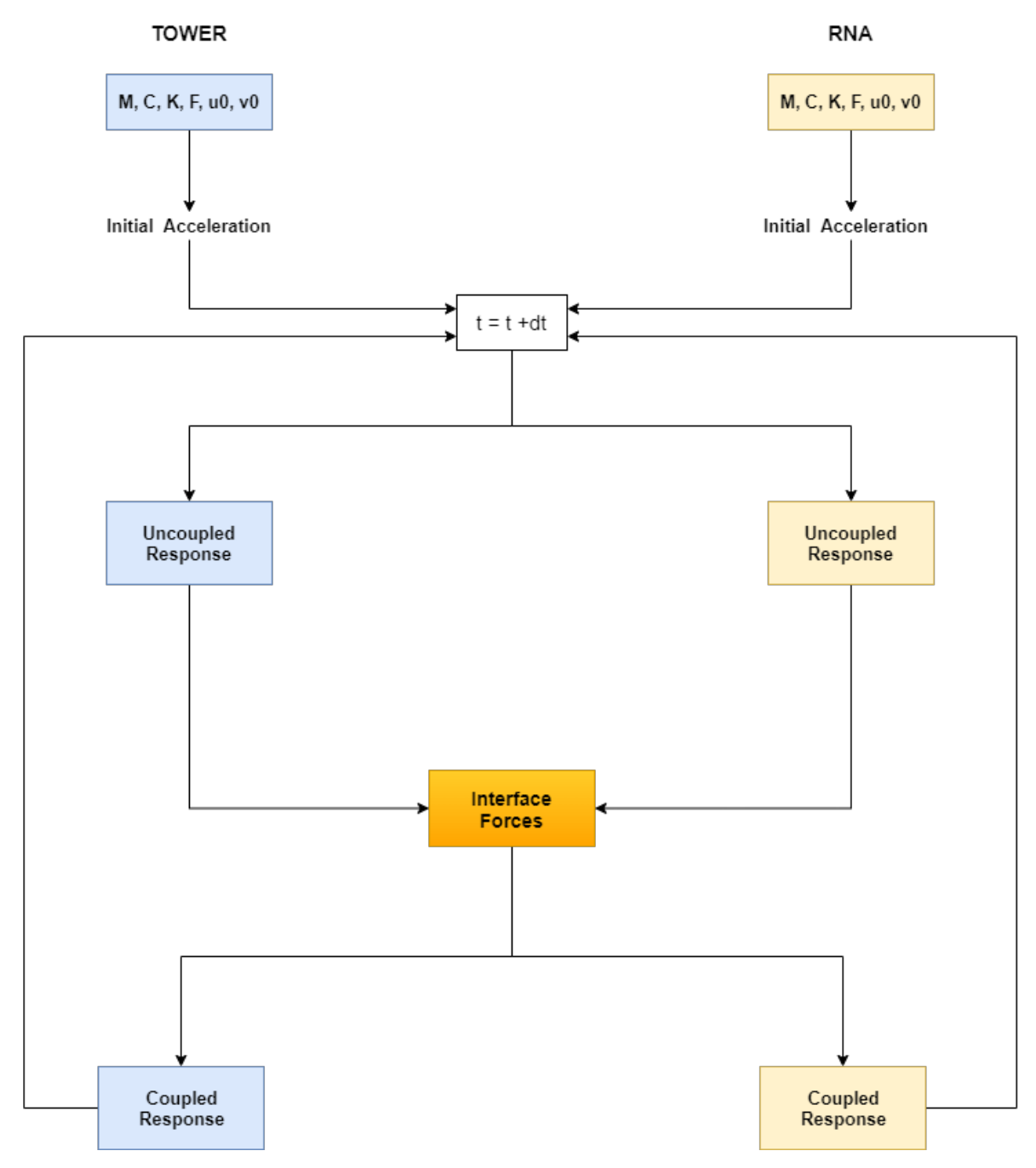


Figure 3.1: Prediction Model algorithm

Contrary to the Impulse Response model discussed in Appendix-B, the prediction model represents both the tower and RNA by Newmark equations. This means the kinematics of the tower is now computed using the Newmark set of equations as shown in Appendix-C, instead of impulse response. As a result, the equations of motion of the two substructures are directly applied in the analysis.

$$\int M^{(sub)} \ddot{u}^{(sub)} + C^{(sub)} \dot{u}^{(sub)} + K^{(sub)} u^{(sub)} = f_n^{(sub)} - B^{(sub)^T} \lambda_n$$
 (3.1)

$$\begin{cases} M^{(rna)} \ddot{u}^{(rna)} + C^{(rna)} \dot{u}^{(rna)} + K^{(rna)} u^{(rna)} = f_n^{(rna)} - B^{(rna)^T} \lambda_n \\ Bu_n = 0 \end{cases}$$
(3.2)

$$Bu_n = 0 (3.3)$$

3.1. Prediction Model 14

The initial accelerations of both substructures at time t=0 are calculated using (C.4). Furthermore, substituting equations (C.2) and (C.3) in the above equations of motion and solving for acceleration results in :

$$\begin{cases}
\ddot{u}_{n}^{(sub)} = S^{(sub)^{-1}} \Big( f_{n}^{(sub)} - C^{(sub)} \hat{u}_{n}^{(sub)} - K^{(sub)} \hat{u}_{n}^{(sub)} \Big) - S^{(sub)^{-1}} \Big( B^{(sub)^{T}} \lambda_{n} \Big) \\
\ddot{u}_{n}^{(rna)} = S^{(rna)^{-1}} \Big( f_{n}^{(rna)} - C^{(rna)} \hat{u}_{n}^{(rna)} - K^{(rna)} \hat{u}_{n}^{(rna)} \Big) - S^{(rna)^{-1}} \Big( B^{(rna)^{T}} \lambda_{n} \Big)
\end{cases}$$
(3.4)

$$\hat{u}_n^{(rna)} = S^{(rna)^{-1}} \left( f_n^{(rna)} - C^{(rna)} \hat{u}_n^{(rna)} - K^{(rna)} \hat{u}_n^{(rna)} \right) - S^{(rna)^{-1}} \left( B^{(rna)^T} \lambda_n \right)$$
(3.5)

where S corresponds to equation (C.5) for both RNA and tower. Initially, the effect of interface forces are not accounted for while computing the uncoupled kinematics of both the substructures. These response estimates are then used to get the interface forces at all DoFs of the interface node at a given time step by replacing the displacements in the Compatibility condition.

$$Bu_n = \begin{bmatrix} B^{(sub)} & B^{(rna)} \end{bmatrix} \begin{bmatrix} u_n^{(sub)} \\ u_n^{(rna)} \end{bmatrix} = 0$$
(3.6)

Solving the above relation leads to equation (B.10) where in this case,

$$W = \begin{bmatrix} \beta dt^2 S^{(sub)^{-1}} & 0\\ 0 & \beta dt^2 S^{(rna)^{-1}} \end{bmatrix}$$
 (3.7)

## RESULTS AND VALIDATION



In this chapter, the prediction model is compared with the reference model. The best option between the two is selected based on the level of accuracy. The model is then used to analyse the wind turbine interface loads for different wind conditions and wind speeds under normal power production case. The obtained results are further compared with the nonlinear time domain aeroelastic simulation results of openFAST to highlight the effect of loss of nonlinear features and finally, a critical review is carried out on the results.

#### 4.1. Validation of Prediction Model

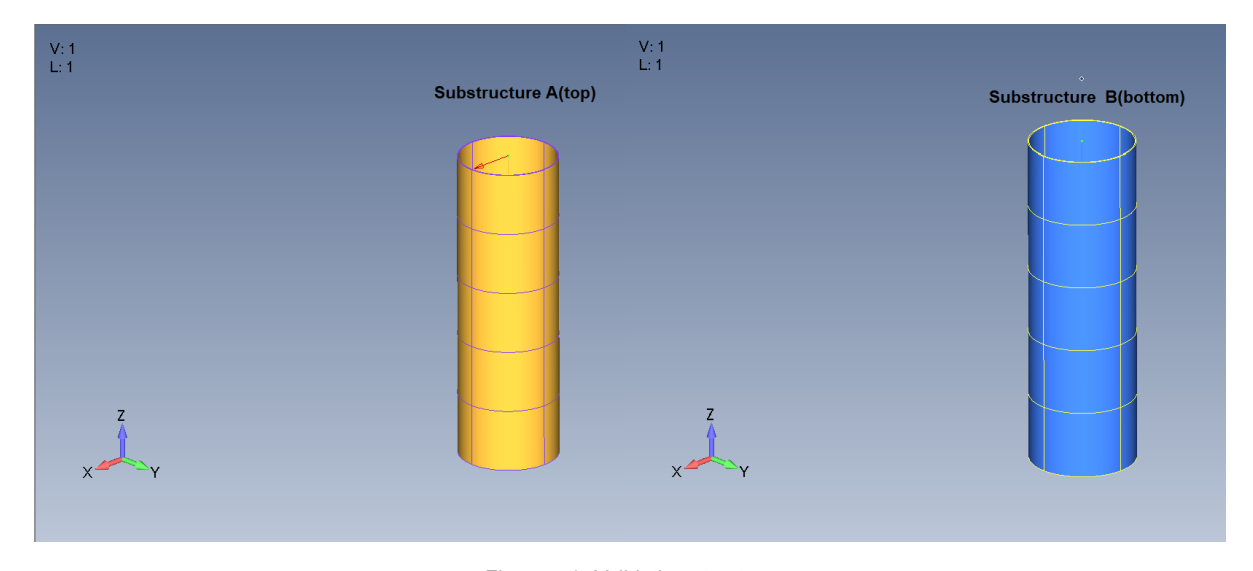


Figure 4.1: Validation structure

This section presents the validation case for the prediction model. Similar to the validation of the reference model in Appendix-D, a simple hollow cylindrical beam with a uniform diameter of 8 meters as shown in table E.1 of Appendix-E is created in *PDT* and is excited by a sinusoidal force at the first node in the x-direction (DoF 1) of node 1 whereas the last node is considered to be fixed to the ground thereby preventing any motion. The kinematics of all the DoFs are then obtained using the *Vibration Toolbox* and are used to validate the prediction model.

	Substructure A									
Node Number	Node ID	X(m)	Y(m)	Z(m)						
1	N_FOU_1000	0	0	20.000						
2	N_FOU_1001	0	0	15.000						
3	N_FOU_1002	0	0	10.000						
4	N_FOU_1003	0	0	5.000						
5	N_FOU_1004	0	0	0.000						
6	N_FOU_1005	0	0	-5.000						
	S	Substructure B								
1	N_FOU_1005	0	0	-5.000						
2	N_FOU_1006	0	0	-10.000						
3	N_FOU_1007	0	0	-15.000						
4	N_FOU_1008	0	0	-20.000						
5	N_FOU_1009	0	0	-25.000						
6	N_FOU_1010	0	0	-30.000						

Table 4.1: List of Nodes - Substructures

The same setup is replicated in the prediction model by decoupling the same structure at node 6 as shown in figure 4.1 in order to extract the coupled kinematics. As a result, substructure A ends at node 6 and substructure B begins at node 6 as depicted in table 4.1 while the location of the external force and constraint are unchanged.

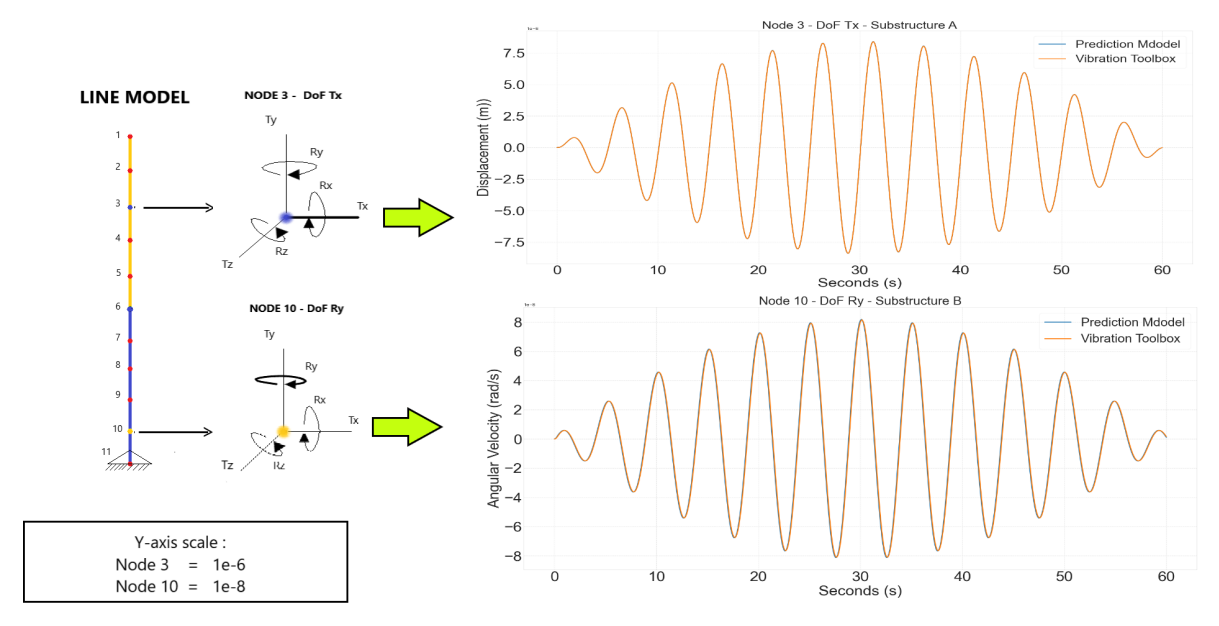


Figure 4.2: Kinematics at node 3(sub. A) and node 5(sub. B)

Figure 4.2 shows the comparison of the kinematics at node 3 and node 10 of the structure obtained from *Vibration Toolbox* with the results from prediction model. Once the structure is split, nodes 3 and 10 fall under substructure A and substructure B respectively. The translation of node 3 corresponds to

displacement in the x-direction whereas the motion of node 10 corresponds to angular velocity in the y-direction.

Model	Noc	le 3 (DoF Tx	<b>(1)</b>	Node 10 (DoF Ry)				
Wiodei	Mean	MSE	SD	Mean	MSE	SD		
Vibration Toolbox	1.2613e-12	3.61e-17	4.34e-06	-3.434e-13	7.06e-18	4.22e-08		
Prediction Model	1.2613e-12	J.016-17	4.546-00	-3.434e-13	7.006-10	4.226-00		

Table 4.2. Validation

Due to the force acting in the x-direction, the results look reasonable such that there is only translation in x-direction and rotation in y-direction. Moreover, table 4.2 shows that the prediction model matches with the results from *Vibration Toolbox* as the mean is same in both cases. It is also found that the correlation coefficient between the two sets of results is 0.99. This holds for all kinematics at all DoFs and suggests that the prediction model shows high conformity with *Vibration Toolbox*. Since the kinematics and interface forces are dependent on each other, it is presumed that the predicted forces at the interface also show the same statistical behavior.

#### 4.2. NREL 5MW Turbine - Test Case

The test cases presented in this section investigate the different module combinations that lead to reasonable load levels using the prediction model, following its validation in the previous section. As discussed in chapter 3,the model requires the mass,stiffness and damping matrices of both substructures in addition to the loads incident on them. In this case,the substructures are the RNA and the tower. Hence, the assumptions and factors considered for the setup to extract the inputs related to these substructures are as follows:

- RNA: Despite the prediction model being linear, the incident aeroelastic loads are extracted from
  nonlinear time domain simulation in openFAST. This is because the aeroelastic loads characteristic
  to a turbulent wind field can only be extracted using nonlinear simulation as the linear model in openFAST only works with steady wind field, thereby excluding any variation in wind speeds. The matrices
  are extracted using the linearization feature in openFAST where the RNA is linearized at the rated
  point. The procedure and setup for extracting the loads and matrices is discussed in Appendix-F.
- **Tower**: The tower is assumed to be externally unloaded because even though there is wind incident on the tower, the magnitude of the external load is small compared to the loads transferred from the RNA. The matrices are obtained using PDT which reads the NREL 5MW tower file in Appendix-D.
- Other Factors: Finally, wind shear and wind direction variation are not included. As a result, pitch control and yaw control are disabled.

Following the extraction of the inputs,three different cases(table 4.3) are analyzed to identify the best combination of modules to be enabled.

Case	Wind Field	Average Wind Speed	Linearization Modules
			ElastoDyn
1	Normal Turbulence	11.40 m/s	ElastoDyn, InflowWind, AeroDyn, ServoDyn
			ElastoDyn, ServoDyn

Table 4.3: Test Case

#### 4.2.1. Test Case 1.: Linearization using ElastoDyn at 11.4 m/s

The rated wind speed of 11.4 m/s is set in the TurbSim module using which the wind field is generated to extract the aeroelastic loads. As for linearization, only the ElastoDyn module is turned on.

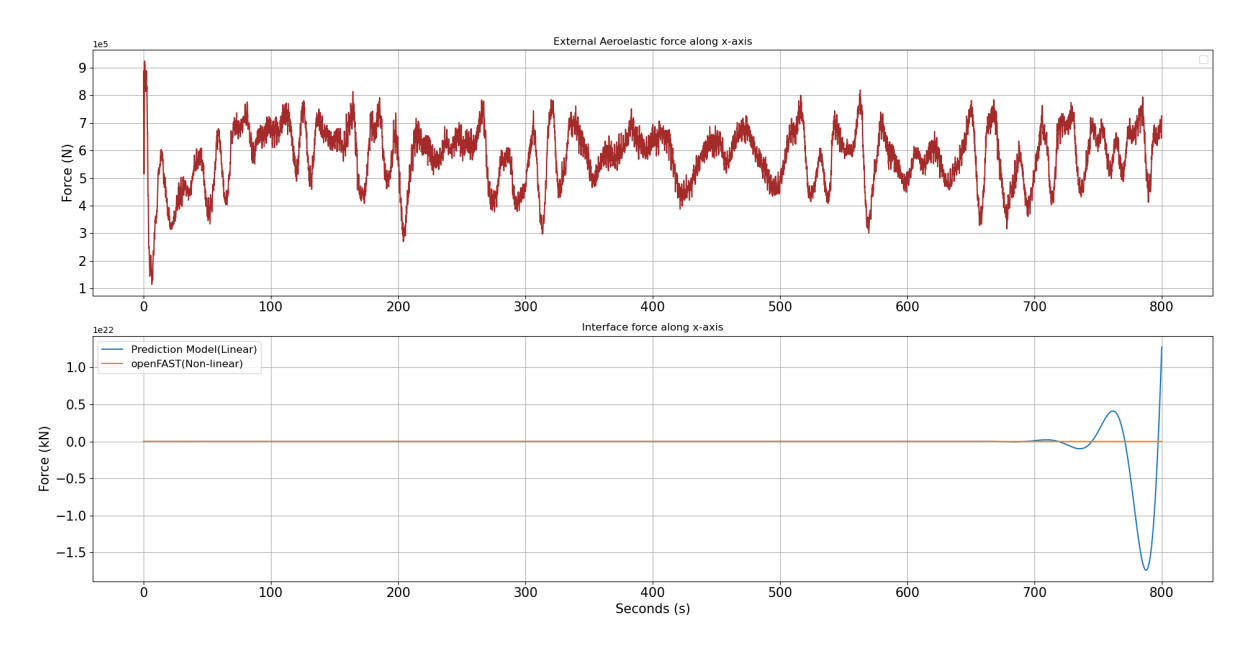


Figure 4.3: External aeroelastic load and Interface force along x-axis at a wind speed of 11.4 m/s from openFAST

Figure 4.3 shows the load incident on the rotor and interface force along the x-axis. It becomes automatically clear that the prediction model highly overestimates the forces at the interface. Table 4.4 contains information that quantifies the behavior of the prediction model when the RNA matrices are obtained using only the ElastoDyn module.

		Interface Degrees of Freedom									
	DoF 1 - Fx	DoF 2 -Fy	DoF 2 -Fy DoF 3 - Fz DoF 4 - Mx DoF 5 -My DoF 6 - Mz								
Mean	596.73	-11.54	-3482.79	3799.9	1228.25	168.28					
	-2.54e+20	1.99e+20	-2.60e+20	3.83e+20	1.30e+22	1.42e+21					
SD	121.33	22.8	20.66	546.98	1409.52	1344.49					
	2.23e+21	1.80e+21	8.3e+22	3.03e+21	1.4e+23	1.22e+22					
Correlation	-0.0486	0.0342	0.0063	0.0251	-0.0260	-0.0154					

Table 4.4: Statistical comparison : openFAST(orange) vs Prediction Model(blue) - Test Case 1.

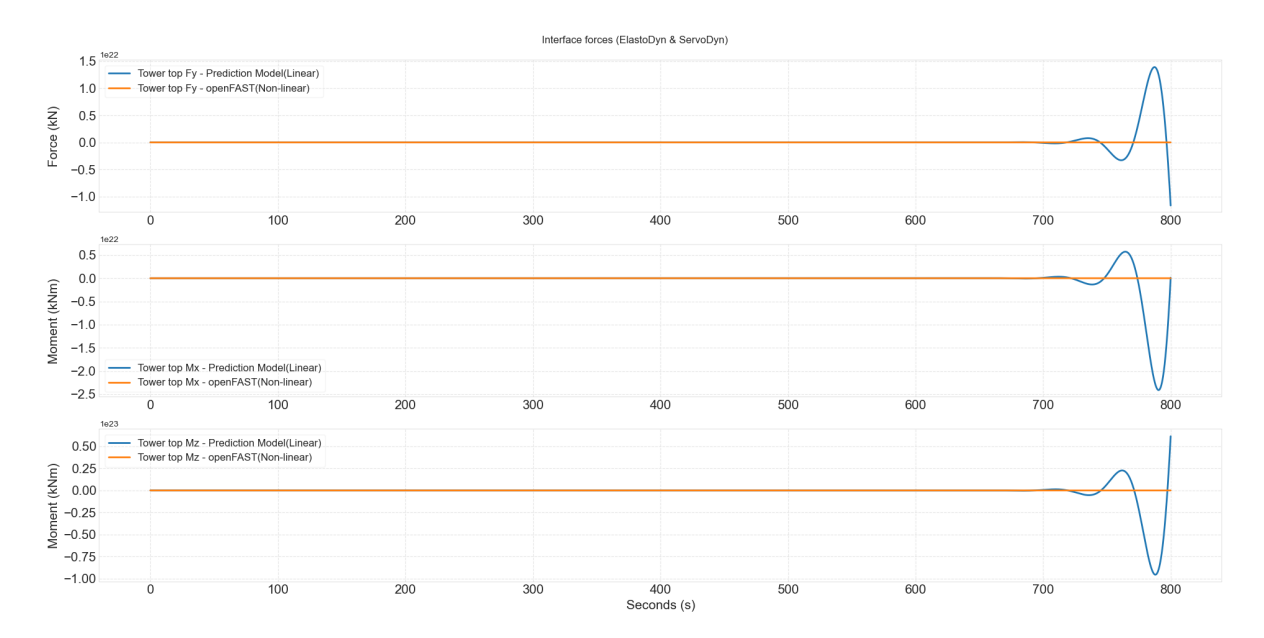


Figure 4.4: Interface Forces - Fy, Mx and Mz (only ElastoDyn module)

Table 4.4 shows that the predicted results drastically deviate from their mean and also show poor correlation with openFAST tower top loads due to the extremely high amplitude. Such high values are not feasible in the real case and therefore, test case 1.2 is established where all modules are enabled during linearization.

#### 4.2.2. Test Case 1.2: Linearization using all modules at 11.4 m/s

In order to improve the quality of the results displayed in the previous section, all the modules: ElastoDyn, InflowWind, ServoDyn and AeroDyn are enabled in this case which takes into account the aeroelastics while computing the state-space matrices of the RNA structure



Figure 4.5: Interface Forces - Fy, Mx and Mz (All 4 modules)

		Interface Degrees of Freedom										
	DoF 1 - Fx	DoF 2 -Fy	2 -Fy DoF 3 - Fz DoF 4 - Mx DoF 5 -My DoF 6 - Mz									
Mean	596.73	-11.54	-3482.79	3799.9	1228.25	168.28						
, mount	170.64	40.92	-45176.67	-5334.45	-10022.97	-4164.24						
SD	121.33	22.8	20.66	546.98	1409.52	1344.49						
	103.87	57.01	10898.23	1598.07	5687.90	974.97						
Correlation	-0.0403	0.03412	0.943	0.0262	0.366	-0.0589						

Table 4.5: Statistical comparison: openFAST(orange) vs Prediction Model(blue) - Test Case 1.2

Similar to the previous case, Figure 4.5 shows a huge improvement in the predicted results when the effect of aeroelastics is included in the linearized matrices. The predicted loads appear to be more stable since the mean and standard deviations have reduced and moved closer to the level of openFAST. But since the aeroelastic loads are being applied separately in the prediction model, the influence of aerodynamics during linearization has to be ignored and this leads to test case 1.3 where AeroDyn and InflowWind are disabled.

# **4.2.3. Test Case 1.3 : Linearization using ElastoDyn and ServoDyn at 11.4 m/s** The turbine is linearized at a rated wind speed of 11.40 m/s, except AeroDyn and InflowWind are disabled to exclude the effect of aerodynamic loading during computation of the state-space matrices.

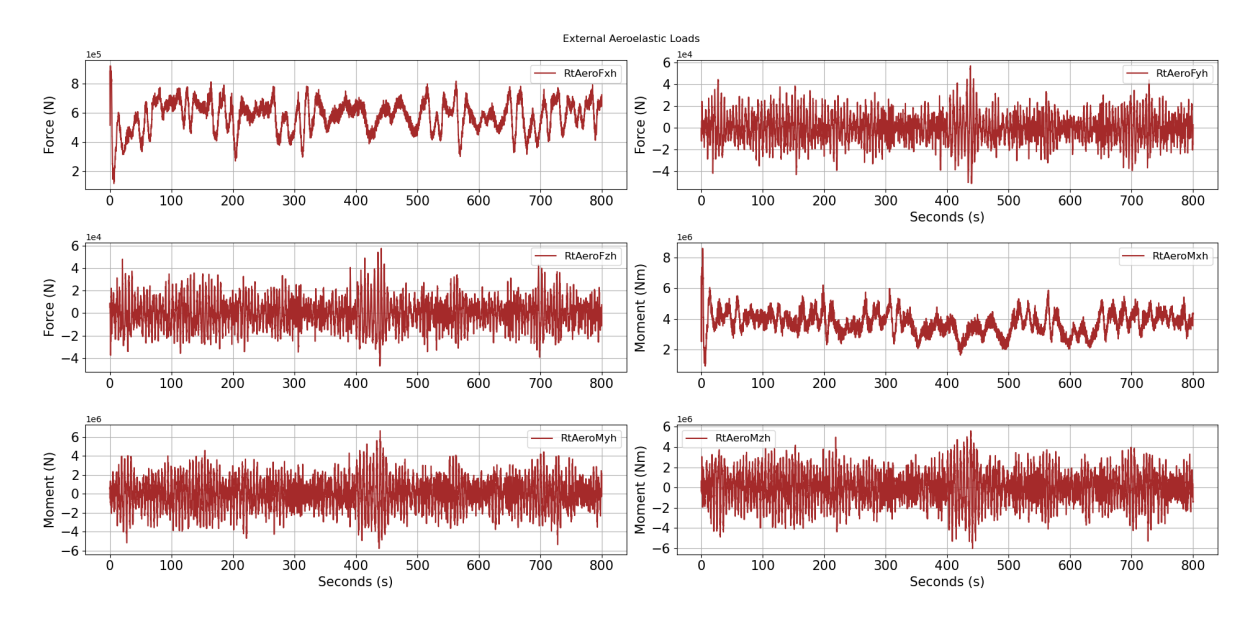


Figure 4.6: External Aeroelastic Load for wind speed of 11.4 m/s from openFAST

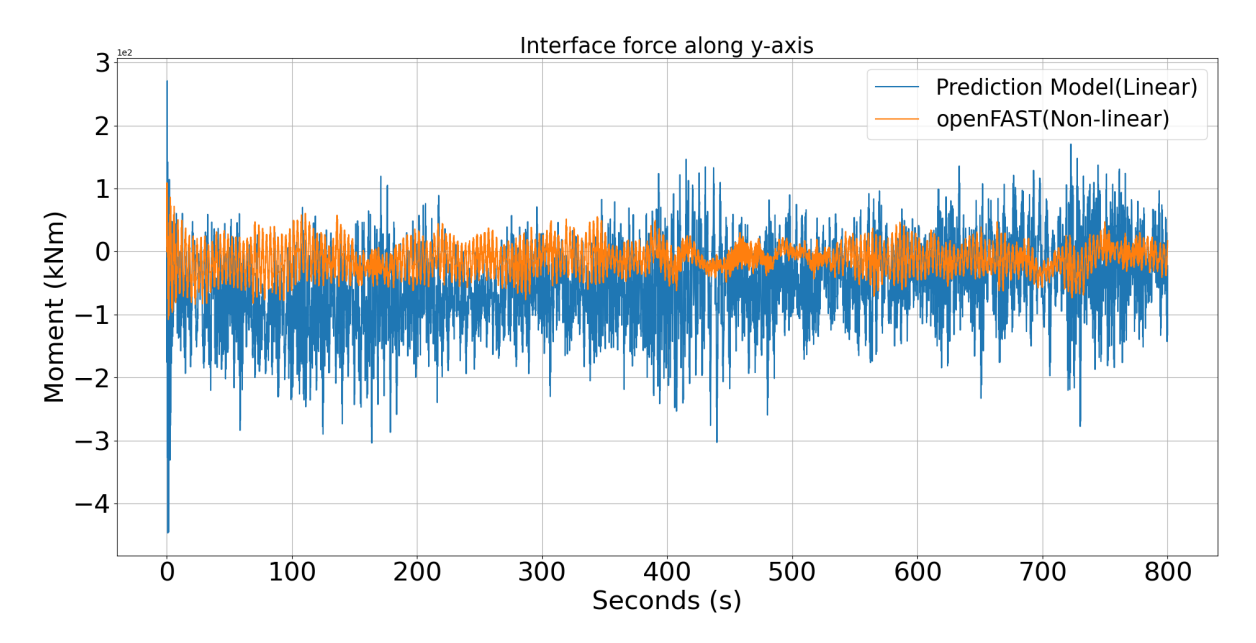


Figure 4.7: Interface force along y-axis at 11.4 m/s

Figure 4.6 displays the load incident on the rotor whereas the interface force in y-axis of the global coordinate system is shown in figure 4.7. Since not many conclusions can be drawn from the time series plot, the interface load at Fy in time domain is translated to the frequency domain.

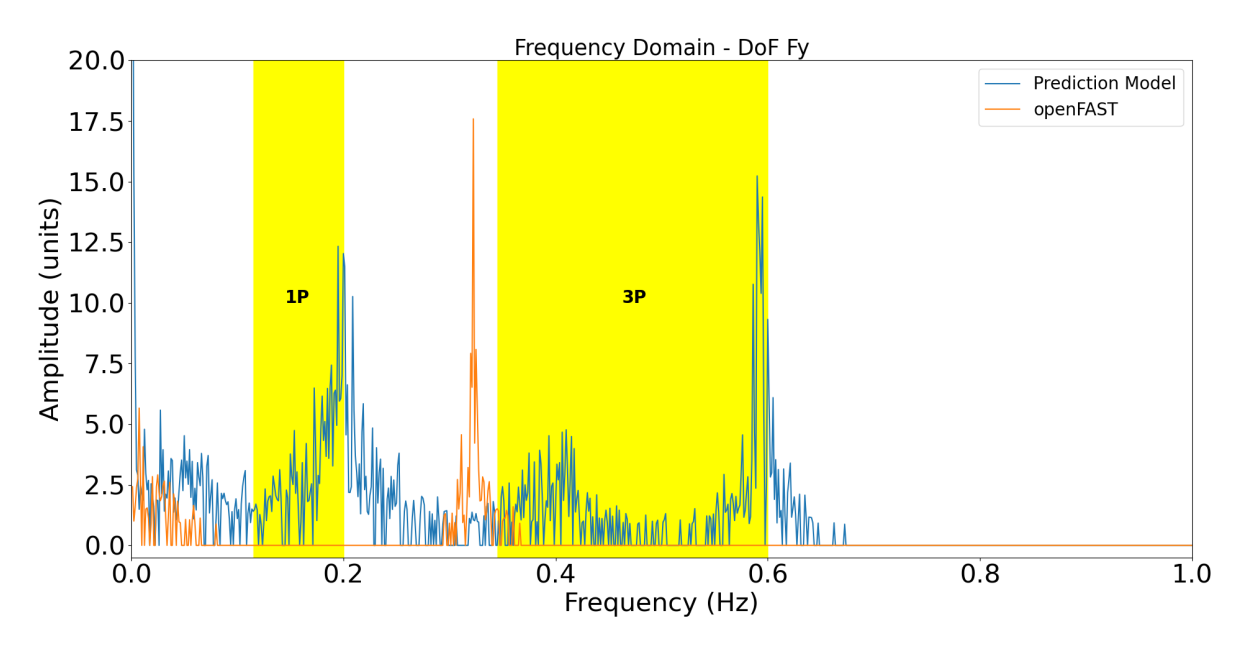


Figure 4.8: Frequency Domain - DoF Fy

Figure 4.8 represents the frequency solution of the load along y-axis. The 1P region denotes the rotor frequency and ranges from 0.115 Hz to 0.2 Hz whereas the 3P region corresponds to 'blade passing frequency' and is from 0.345 Hz to 0.6 Hz [4]. Additionally, a statistical analysis is performed in table 4.6 where the tower top loads from openFAST is compared against the interface force of the prediction model.

		Interface Degrees of Freedom										
	DoF 1 - Fx	DoF 2 -Fy	DoF 3 - Fz DoF 4 - Mx DoF 5 -My DoF 6 - Mz									
Mean	596.73	-11.54	-3482.79	3799.9	1228.25	168.28						
, mount	705.88	-57.03	-89923.4	-4074.95	35469.68	-2910.97						
SD	121.33	22.8	20.66	546.98	1409.52	1344.49						
	553.01	61.96	44602.81	1637.63	27596.80	888.52						
Correlation	0.0046	-0.0009	0.0226	-0.0687	0.330	-0.0514						

Table 4.6: Statistical comparison : openFAST(orange) vs Prediction Model(blue)

The observations deduced from table 4.6 are as follows:

- The Pearson's correlation is used to compare the predicted loads with openFAST results. Ideally, a coefficient of 0.90 to 0.99 suggests a good match as seen in section 4.1 but it is noticeable that the model shows poor correlation with openFAST. DoF 2, DoF 4 and DoF 6 have a low negative correlation which suggests that the solutions move in opposite directions.
- Finally, huge differences in the mean and standard deviation, especially in DoF 3 and DoF 5 are observed as a result of the larger amplitude of the results from the prediction model. This is also evident in table 4.5 and such huge variations occur due to the non-stationary and unstable nature of the predicted loads at these DoFs.

The reason for the observations as seen above will be discussed in the further sections.

#### 4.3. NREL 5MW Turbine - Simulation Cases

Based on the observations of the test cases, further simulations at different wind speeds and wind conditions are performed as shown in table 4.7.

Case	Wind Field	Average Wind Speed
2	Normal Turbulence	9.32 m/s
		23.64 m/s
3	Steady	16.40 m/s

Table 4.7: Simulation Cases

Table 4.7 shows three different cases considered under this section of which one wind speed(9.32 m/s) lies below the rated condition, two wind speeds above the rated condition(16.40 m/s and 23.64m/s). The turbine is linearized at the rated condition and the blades are pitched for above rated wind speeds to keep the rotor speed, generator torque and generator power constant. The combination of parameters related to the respective wind speeds are shown in table 4.8.

Case	Average Wind Speed	Blade pitch angles	Generator Speed
2.	9.32 m/s	0°	768.72 rpm
2.2	23.64 m/s	21.87°	1173.7 rpm
3.	16.40 m/s	13.24°	1173.7 rpm

Table 4.8: Simulation Case parameters

Only the behavior of DoF Fy and DoF Mz are included for each case while the other degrees of freedom are displayed in Appendix-G. Finally, the results are interpreted to understand the behavior of the prediction model under different wind conditions.

#### 4.3.1. Case 2. : Average Wind speed 9.32 m/s

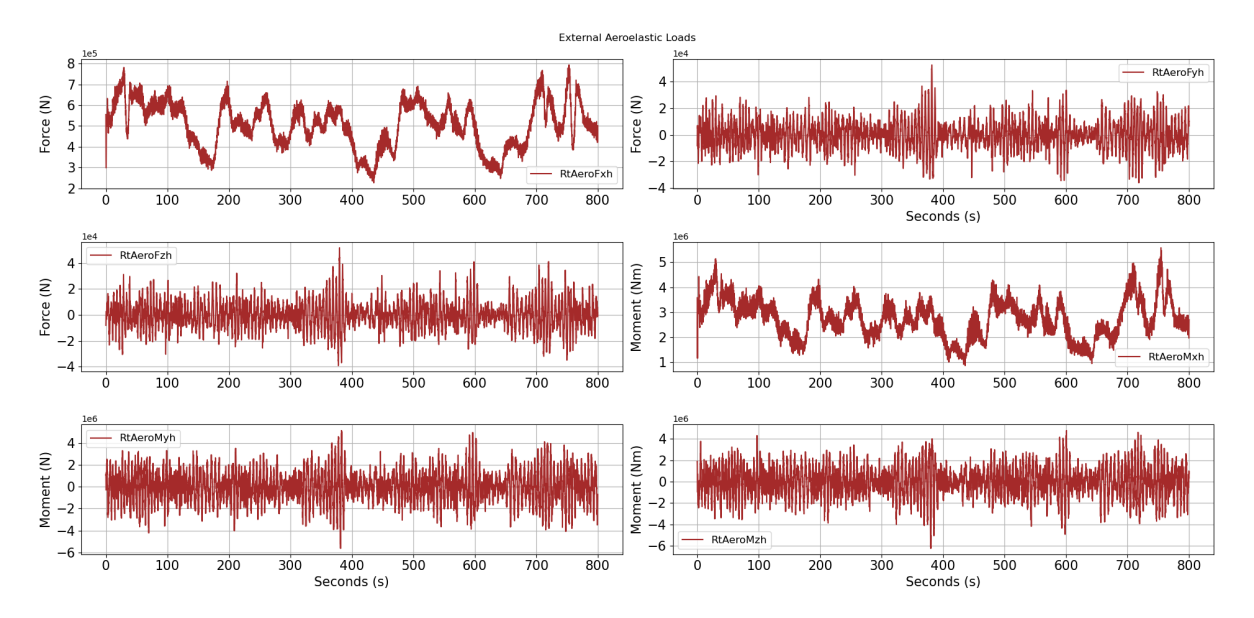


Figure 4.9: External Aeroelastic Loads at an average wind speed of 9.32 m/s from openFAST

The incident aeroelastic loads for a turbulent wind field with an average wind speed of 9.32 m/s is displayed in figure 4.9. The force and moment is the highest in the x-direction since the wind is directly incident on the rotor and no flow angle is considered.

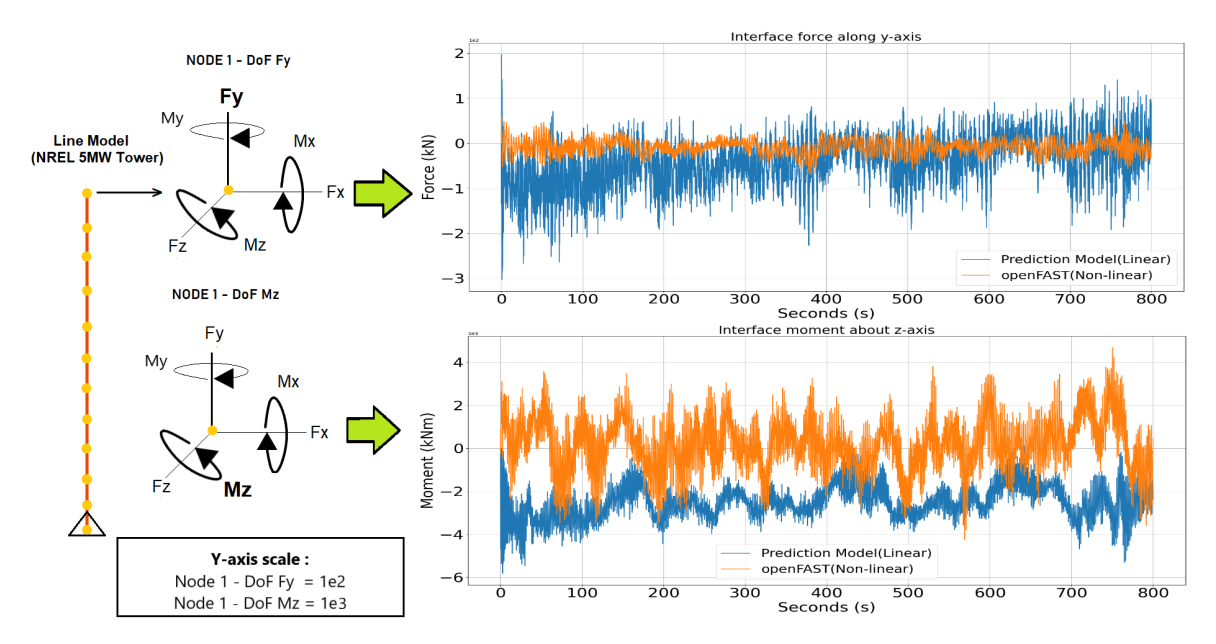


Figure 4.10: Time Domain - Interface DoF Fy and Mz for 9.32 m/s

The resulting interface force along y-axis and moment about z-axis in the time domain is shown in figure 4.10.

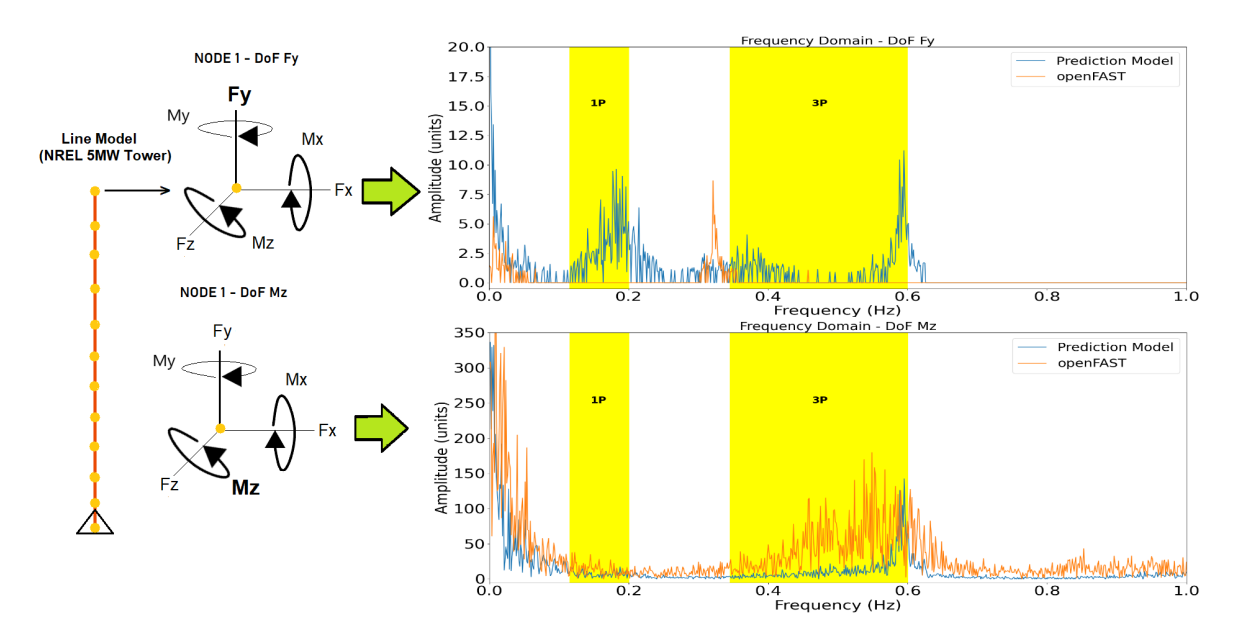


Figure 4.11: Time Domain - Interface DoF Fy and Mz for 9.32 m/s

In figure 4.11, the results in time domain are translated to the frequency domain using Fourier transform. In the frequency domain, the amplitude of the loads are plotted against the frequencies including the the 1P and 3P natural frequency regions of the rotor. The results for other degrees of freedom are provided in section G.2.

#### 4.3.2. Case 2.2 : Average Wind speed 23.64 m/s

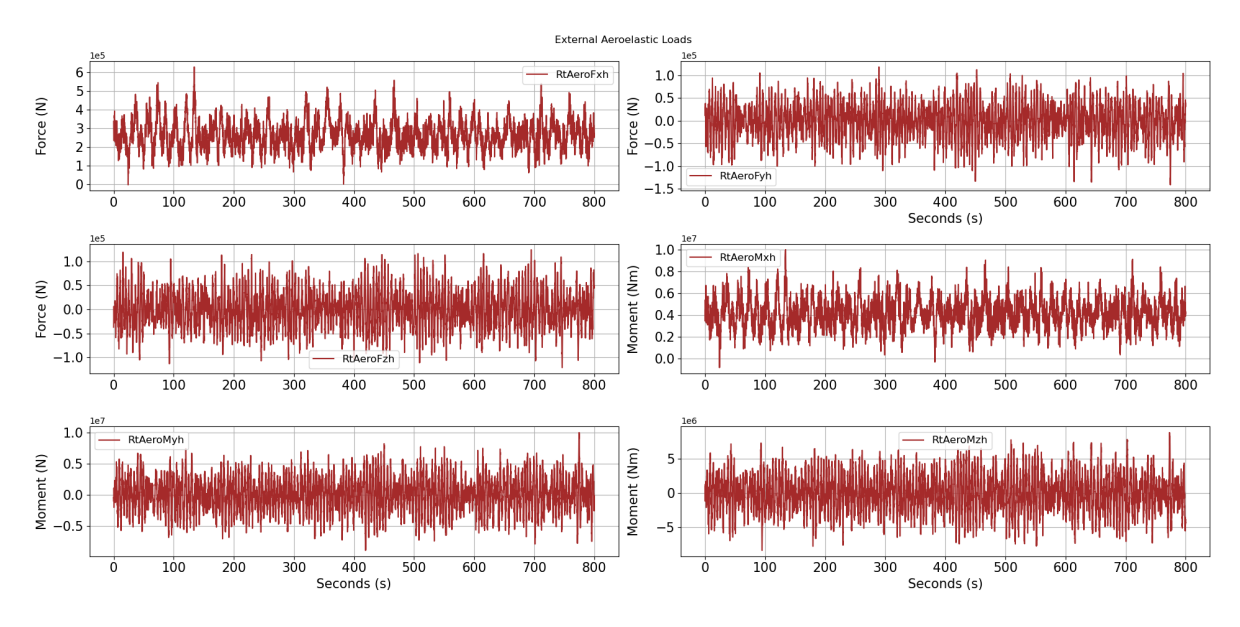


Figure 4.12: External Aeroelastic Load at an average wind speed of 23.64 m/s from openFAST

The incident aeroelastic loads for a turbulent wind field with an average wind speed of 23.64 m/s is evident in figure 4.12. The force and moment is the highest in the x-direction since the wind is directly incident on the rotor and no flow angle is considered.

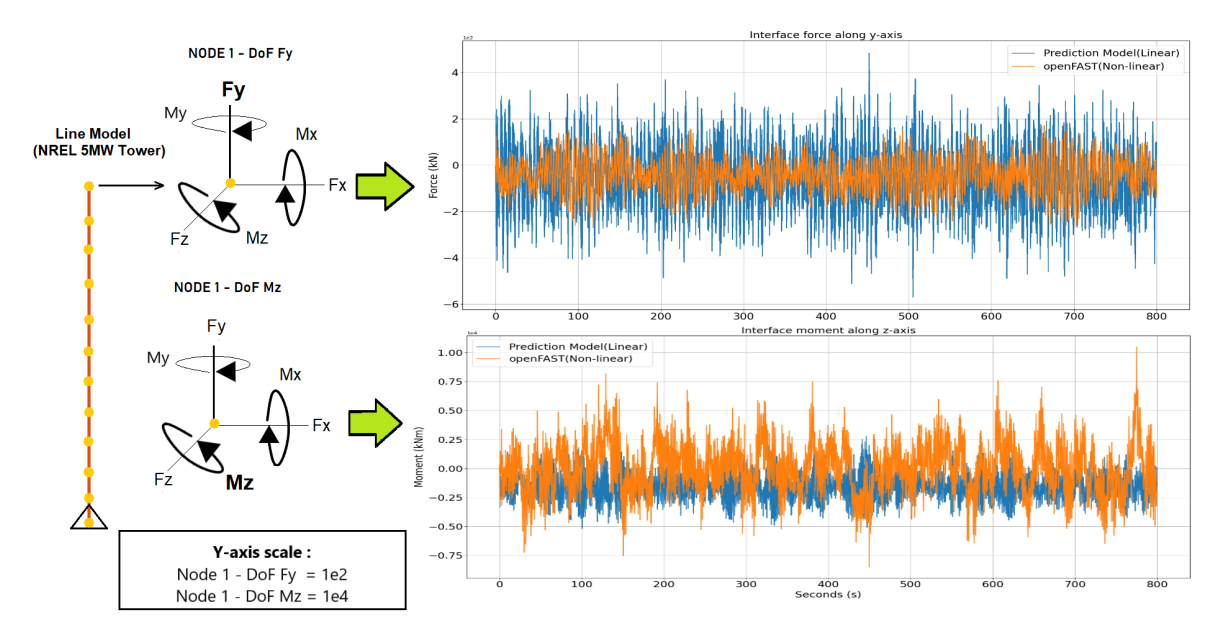


Figure 4.13: Time Domain - Interface DoF Fy and Mz for 23.64 m/s

The application of aeroelastic loads in the prediction model leads to the resulting interface forces and moments in the time domain, as shown in figure 4.13.

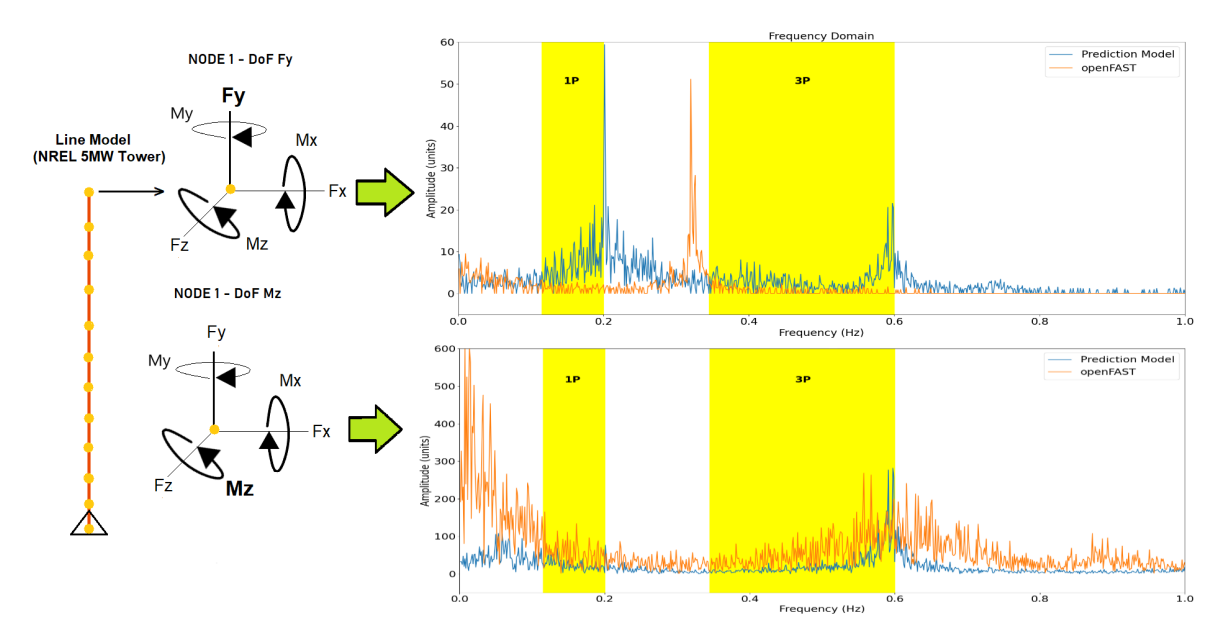


Figure 4.14: Frequency Domain - Interface DoF Fy and Mz

The frequency domain plots in figure 4.14 correspond to the interface DoFs in time domain shown in figure 4.13. The results for other degrees of freedom are displayed in Appendix-G.3.

#### 4.3.3. Case 3. : Steady Wind speed 16.40 m/s

This section discusses the interface loads for the steady wind condition at a wind speed of 16.40 m/s. Similar to the previous the loads are maximum in the x-direction due to the absence of flow angles and wind direction.

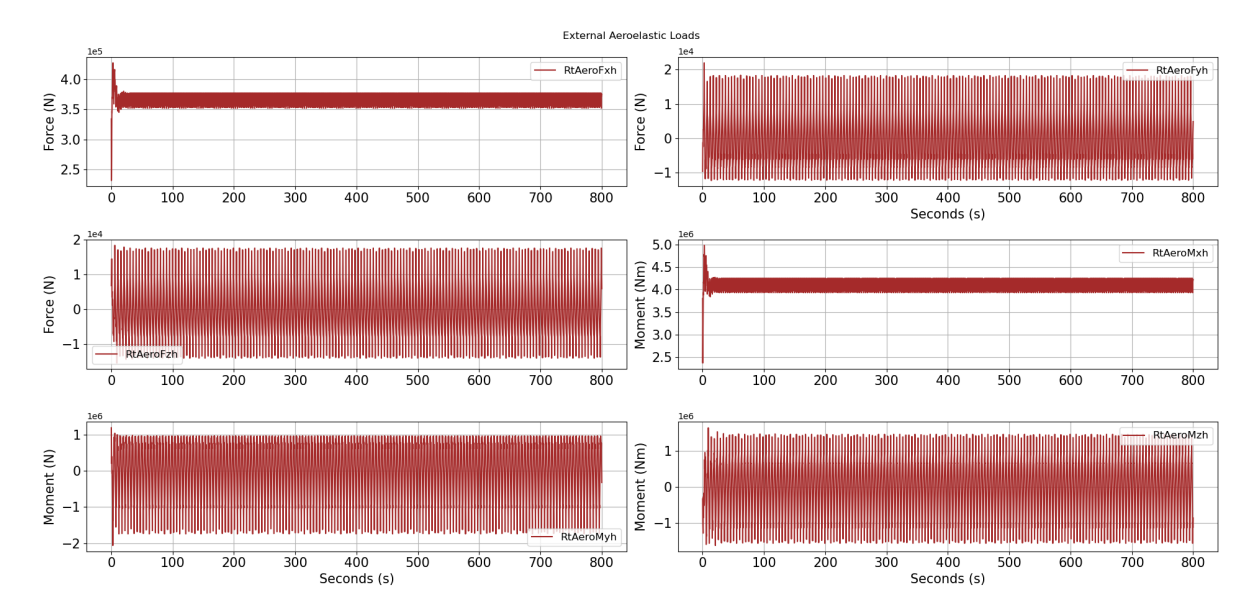


Figure 4.15: External Aeroelastic Loads at steady wind speed of 16.40 m/s from openFAST

Figure 4.15 show similar plots in section 4.3. but in this case, there is constant variation because the wind speed remains the same at all points in the generated wind field.

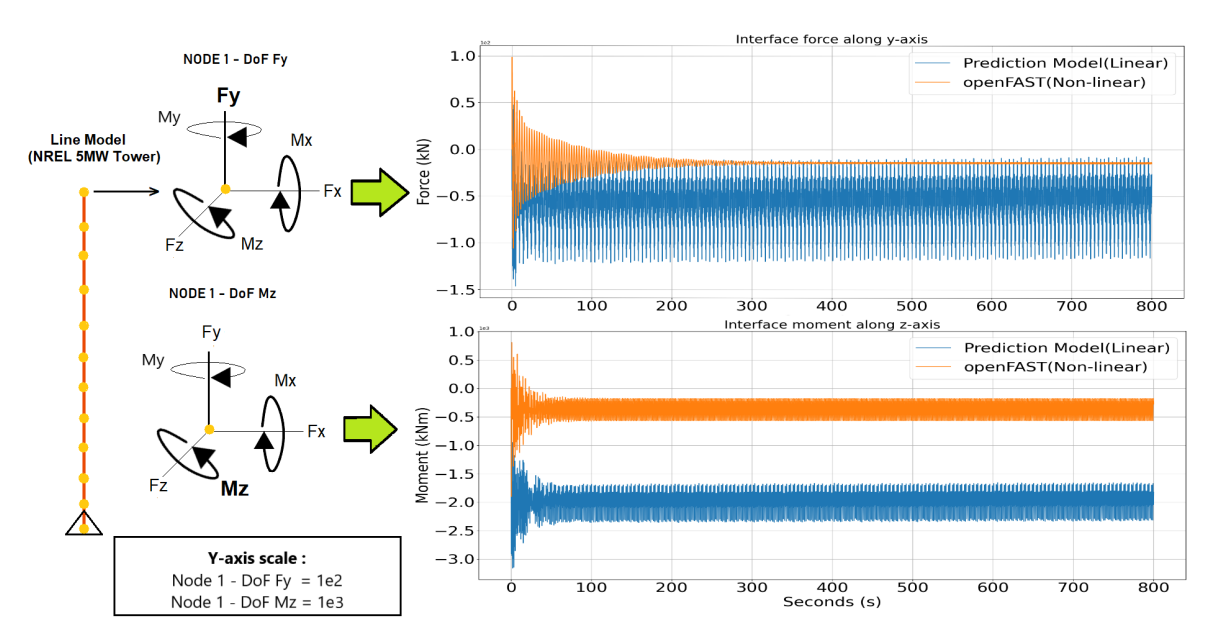


Figure 4.16: Time Domain - Interface DoF Fy and Mz for 16.40 m/s

Consequentially, this also leads to steady loads at the interface as shown in figure 4.16. It is clear that even though the loads are steady, the mean of the predicted loads vary from the openFAST loads.

4.4. Discussion

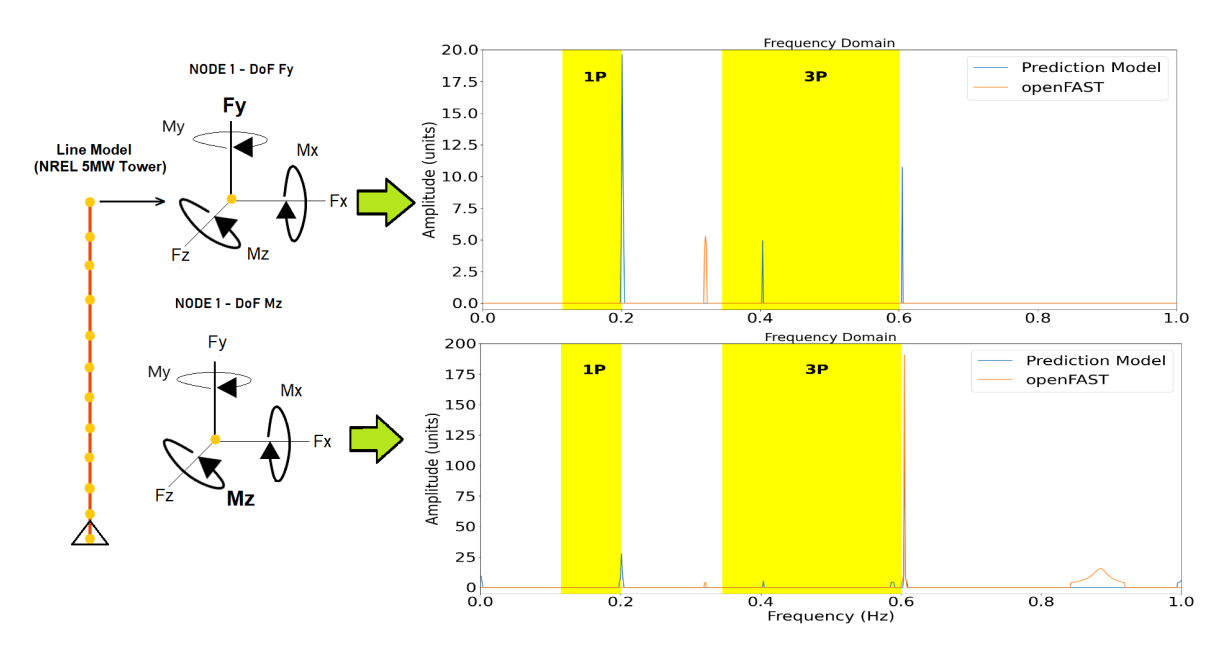


Figure 4.17: Frequency Domain - Interface DoF Fy and Mz for 23.64 m/s

The frequency and amplitude of the interface load at y-axis and moment about z-axis are shown in figure 4.17 respectively.

#### 4.4. Discussion

The results between openFAST and the prediction model presented in sections 4.2.3 to 4.3.3 in addition to the results of other DoFs in Appendix-G is interpreted in this section.

The primary observation deduced from the time domain plots for each interface DoF only suggest that the amplitude of the predicted loads vary from openFAST. This effect is also evident in the frequency domain which provides better insight than the time series. The frequency plots highlight the excitation frequencies in the structure and their effect on the structural behavior.

Firstly,the DoFs presented in the previous sections are discussed. For a turbulent wind field with an average wind speed of 11.4 m/s,figure 4.8 shows substantial amount of peaks with high amplitudes within the 1P and 3P regions which indicates a potential occurrence of resonance. This could be a possible reason as to why the loads at *Fy* begin to become slightly unstable towards the end of the time series as seen in figure 4.7. As a result, there is also a possibility that the loads continue to increase beyond 800 seconds. The same also applies to the turbulent case of 9.32 m/s where the interface force at *Fy* continues to increase.

However,the same observation does not hold for above rated wind speeds as the interface force at *Fy* appears to be stable throughout the time series for 16.40 m/s and 23.64 m/s. This could be attributed to the fact that the number of dominant peaks in the 1P and 3P regions are reduced and their position is shifted towards the edge of these natural frequency regions. For example,in figure 4.14,the first excitation frequency of the prediction model appears at 0.20125 Hz. The amplitude of this peak is clearly higher than that of openFAST which appears at 0.32 Hz. This again indicates a potential occurrence of resonance in the case of predicted loads since the dominant peak appears too close to the 1P natural frequency region of the rotor, which ends at 0.2 Hz. But interestingly,this does not affect the stability of the interface force at *Fy* at these wind speeds. This implies that the influence of the resonance effect on the dynamic behavior of the turbine could be more significant at below rated wind speeds rather than wind speeds higher than 11.4 m/s.

On the other hand, the interface moments at DoFs Mz and Mx (Appendix-G) seem to be stable for all cases even though the peaks fall within the 3P region of the rotor and have lower amplitudes compared

4.5. Limitations 28

to the peaks at other DoFs. This further suggests that the effect of resonance is minimal on these degrees of freedom. Furthermore, the presence of additional peaks in the case of prediction model could be a likely explanation for the higher amplitudes in the time domain and vice versa.

A potential reason for the high amplitudes of the excitation frequencies could be ignorance of aerodynamic stiffness and aerodynamic damping during linearization. This is because disabling AeroDyn not only excludes the influence of aerodynamic loading but also leaves out stiffness and damping that is associated with it. Additionally, centrifugal stiffness which can only be accounted for when the rotor is in the rotational frame, is also excluded. The behavior at other degrees of freedom,namely *Fx,Fz* and *My* fall under the limitations of the prediction model which is discussed in the following section.

#### 4.5. Limitations

Contrary to the DoFs analysed in the previous section, it is possible that Fx, Fz and My are severely affected by the resonance effect as seen in Appendix-G. A short example case is provided below.

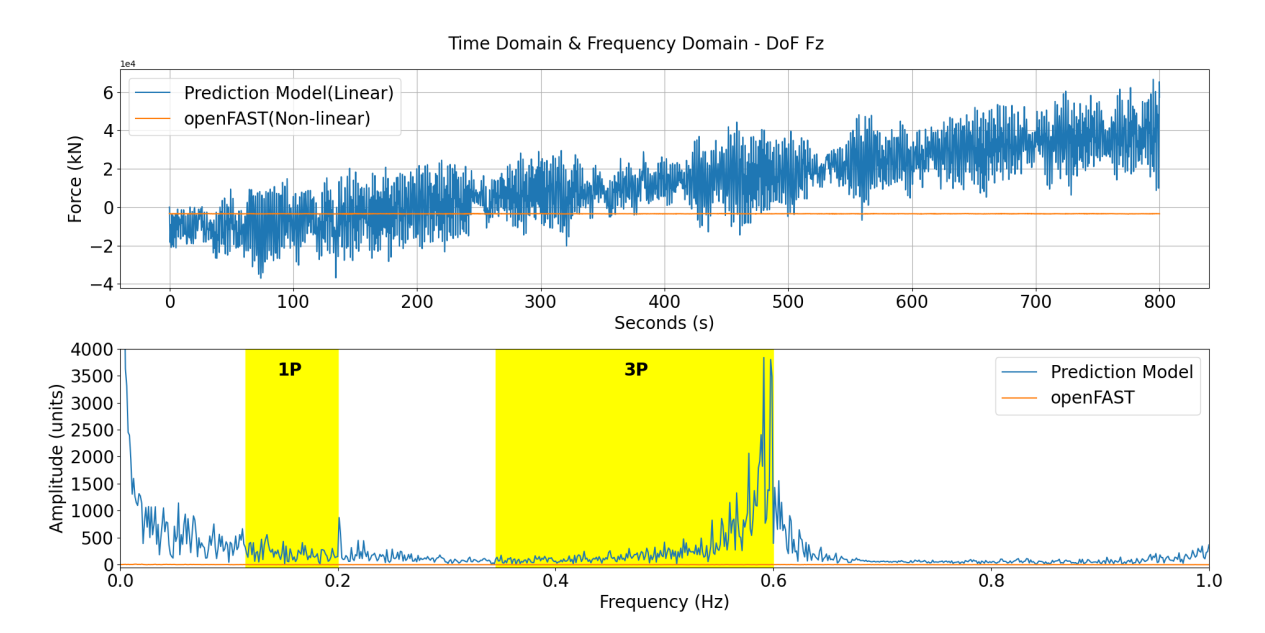


Figure 4.18: Interface force along z-axis for 23.64 m/s

Ideally, the force along z-axis should be minimal for all cases since it corresponds to the height of the tower but this is not the case for the prediction model. More importantly, it is not exactly known why the prediction model captures the effect of frequencies similar to openFAST for DoF My but fails to do the same in the time domain, i.e. the interface loads at My in time domain become unstable while the peaks in frequency domain appear close to that of openFAST as shown in figure. This also happens in DoFs Fx and Fz but in this scenario, there is a mismatch between the peaks from both models in all cases. Hence, this is the reason for the huge deviation in the mean and standard deviation corresponding to these DoFs in table 4.6.

# CONCLUSION & RECOMMENDATIONS



#### 5.1. Conclusion

A model has been developed to enable the FD to compute and predict the loads occurring at the interface between the RNA and the tower using the method of Dynamic Substructuring. The basis of the model was based on a initial combination of impulse response(tower) and Newmark(RNA) methods but eventually, the decision to base it entirely on the Newmark was made as it directly applies the mass, stiffness and damping matrices in the analysis as opposed to the *Impulse Response Model* which uses the matrices to compute the impulse response matrix at each time step. It is also important to note that the presented model is suitable for load case simulations rather than certification analyses.

Furthermore, the NREL 5MW turbine has been selected in this research to perform numerical simulations and analyze the interface load levels at different wind speeds and wind conditions. Due to the linear nature of the prediction model, the RNA was linearized at the rated point using *openFAST* to extract the matrices. Similarly, the tower matrices were obtained using *PDT*. The normal turbulence simulations corresponding to normal power production were performed at 9.32 m/s, 11.4 m/s and 23.64 m/s and steady wind analysis was performed at 16.40 m/s.

The final results provided insight into the magnitude of the interface loads due to the incident aeroelastic forces on the rotor for different wind conditions. Additionally, the results in time domain were converted to frequency domain to analyze the effect of resonance at the interface DoFs. The frequency plots indicated the occurrence of additional peaks in the prediction model, compared to openFAST. It was also found that even though the peaks had high amplitudes, the resonance did not have a significant influence at DoFs Fy, Mx and Mz since the loads remained stable for throughout the time series. On the other hand, extremely high and unstable loads were encountered at DoFs Fx, Fz and My possibly due to the resonance effect.

Overall, the model shows positive scope since it captures the dynamic behavior at certain DoFs to a certain extent compared to openFAST. But it is concluded that just a standalone version of a model based on Newmark equations is not sufficient to analyze the dynamic behavior of aeroelastic structures as the methodology followed in this research fails to account for factors such as aerodynamic damping and aerodynamic stiffness.

5.2. Recommendations 30

#### 5.2. Recommendations

Since the loads incident on the rotor are extracted using nonlinear time domain simulation, there is a possibility that the effect of inertial, elastic forces is already considered in the computation of aeroelastic loads as for aeroelastic structures, a good solution depends on the interactions between the elastic, inertial and aerodynamic forces. If that is indeed the case, a likely area to explore involves developing methods that counteract these forces. Additionally, the incorporating filters as in the case of openFAST could further help reduce the amplitude of the solution in the prediction model.

# Bibliography

- [1] Haliade x-14 mw. URL: https://www.ge.com/renewableenergy/wind-energy/offshore-wind/haliade-x-offshore-turbine.
- [2] openfast architecture. URL: https://raf-openfast.readthedocs.io/en/docs-fast8readme/source/user/openfast/input files.html.
- [3] Vibration toolbox. URL: https://github.com/vibrationtoolbox/vibration toolbox.
- [4] S. Bhattacharya, N. Nikitas, J. Garnsey, J. Cox, D. Lombardi, N.A. Alexander, and D. Muir Wood. Observed dynamic soil—structure interaction in scale testing of offshore wind turbine foundations. *Soil Dynamics and Earthquake Engineering*, 2013. URL: https://doi.org/10.1016/j.soildyn.2013.07.012.
- [5] J.P.A.A. Blasques. User's manual for becas: A cross section analysis tool for anisotropic and inhomogeneous beam sections of arbitrary geometry. Technical report, 2012. URL: https://backend.orbit.dtu.dk/ws/portalfiles/portal/7711204/ris r 1785.pdf.
- [6] International Electrotechnical Commission. International standard iec 61400-1, 2005-08. URL: https://webstore.iec.ch/preview/info iec61400-1%7Bed3.0%7Den.pdf.
- [7] D. de Klerk, D.J. Rixen, and J. de Jong. The frequency based substructuring (fbs) method reformulated according to the dual domain decomposition method. Proceedings of the XXIV International Modal Analysis Conference, 2006. URL: https://www.researchgate.net/publication/265790826\_The\_Frequency\_Based\_Substructuring\_Method\_reformulated according to the Dual Domain Decomposition Method.
- [8] D. de Klerk, D.J. Rixen, and S.N. Voormeeren. General framework for dynamic substructuring: History, review, and classification of techniques. *AIAA*, pages 1169–1181, 2008. URL: https://arc.aiaa.org/doi/10.2514/1.33274.
- [9] DNVGL. Standard dnvgl-st-0437: Loads and site conditions for wind turbines, 2016. URL: https://rules.dnv.com/docs/pdf/DNV/ST/2016-11/DNVGL-ST-0437.pdf.
- [10] M. Geradin and D. J. Rixen. Mechanical vibrations: Theory and application to structural dynamics 3rd edition. *The Aeronautical Journal*, 122:857, 2015. doi:10.1017/aer.2018.27.
- [11] N. Haghighat. Impulse based substructuring: Theory, improvement, and its implementation on real problems, 2011. URL: https://repository.tudelft.nl/islandora/object/uuid%3Ad1143b64-43fd-4dca-b5ce-7e9ea77260ea.
- [12] J. He and Z.-F. Fu. Modal Analysis. 2001.
- [13] IRENA. Future of wind: Deployment, investment, technology, grid integration and socio-economic aspects(a global energy transformation paper). https://www.irena.org/-/media/files/irena/agency/publication/2019/oct/irena future of wind 2019.pdf, 2019.
- [14] J. Jason and B. Jonkman. Fast modularization framework for wind turbine simulation: full-system linearization, 2016. URL: https://www.nrel.gov/docs/fy19osti/71865.pdf.
- [15] B. Jonkman. Re: Openfast: Linearization of nrel 5mw onshore turbine [discussion post], 2021. URL: https://wind.nrel.gov/forum/wind/viewtopic.php?f=4&t=2823&p=18214&hilit=second+order+stiffness+and+damping#p18157.
- [16] B. Jonkman, J. Jonkman, G.J. Hayman, R.R. Damiani, and R.E. Murray. Aerodyn v15 user's guide and theory manual. URL: https://www.nrel.gov/wind/nwtc/assets/pdfs/ aerodyn-manual.pdf.

Bibliography 32

[17] B. Jonkman and L. Kilcher. Turbsim user's guide: version 1.06.00, 2012. URL: https://www.nrel.gov/wind/nwtc/assets/pdfs/turbsim.pdf.

- [18] J. Jonkman, S. Butterfield, W. Musial, and G. Scott. Definition of a 5-mw reference wind turbine for offshore system development. Technical report, 2009. URL: https://www.nrel.gov/docs/fy09osti/38060.pdf.
- [19] National Renewable Energy Laboratory. openfast documentation: release v2.5.0, 2021. URL: https://ebranlard-openfast.readthedocs.io/\_/downloads/en/f-driver-ua/pdf/.
- [20] P. Passon and K. Branner. Load calculation methods for offshore wind turbine foundations. *Ships and Offshore Structures*, 9(4):433–449, 2013. doi:10.1080/17445302.2013.820108.
- [21] A. Platt, B. Jonkman, and J. Jonkman. Inflowwind user's guide, 2016. URL: https://www.nrel.gov/wind/nwtc/assets/downloads/InflowWind/InflowWind\_Manual.pdf.
- [22] D.J. Rixen. A substructuring technique based on measured and computed impulse response functions of components. *Proceedings of ISMA*, pages 1939–1954, 2010. URL: http://past.isma-isaac.be/downloads/isma2010/papers/isma2010 0405.pdf.
- [23] D.J. Rixen and P.L. van der Valk. An impulse based substructuring approach for impact analysis and load case simulations. *Journal of Sound and Vibration*, pages 7174–7190, 2013. doi: 10.1016/j.jsv.2013.08.004.
- [24] K. Subbaraj and M. Dokainish. A survey of direct time-integration methods in computational structural dynamics ii. implicit methods. *Computers and Structures*, 32(6):1387–1401, 1989. doi:10.1016/0045-7949(89)90315-5.
- [25] D. D. van den Bosch. *IMPULSE BASED SUBSTRUCTURING UNRAVELLED: Simulation and Coupling of Structural Dynamics in the time domain*. PhD thesis, Delft University of Technology, 2014.
- [26] M. van der Seijs and D.J. Rixen. Efficient impulse based substructuring using truncated impulse response functions and mode superposition. *Proceeding of ISMA*, pages 3487–3500, 2012. URL: http://past.ismaisaac.be/downloads/isma2012/papers/isma2012 0864.pdf.
- [27] Maarten van der Seijs. Experimental dynamic substructuring: Analysis and design strategies for vehicle development. 2016. URL: https://www.semanticscholar.org/paper/Experimental-dynamic-substructuring-%3A-Analysis-and-Seijs/c38c06cb4215381b92c1683f12286b262e979dbb.
- [28] P. van der Valk and D.J Rixen. An effective method for assembling impulse response functions to linear and non-linear finite element models, 2012. URL: https://www.researchgate.net/publication/288047894\_An\_Effective\_Method\_for\_Assembling\_Impulse\_Response Functions to Linear and Non-linear Finite Element Models.
- [29] P. van der Valk and D.J. Rixen. Impulse based substructuring for coupling offshore structures and wind turbines in aero-elastic simulations, 2012. URL: https://www.researchgate.net/publication/268478610\_Impulse\_Based\_Substructuring\_for\_Coupling\_Offshore Structures and Wind Turbines in Aero-Elastic Simulations.
- [30] P.L. van der Valk. Coupled simulations of wind turbines and offshore support structures: Strategies based on the dynamic substructuring paradigm, 2014. URL: https://www.researchgate.net/publication/275213625\_Coupled\_Simulations\_of\_Wind\_Turbines\_and\_Offshore\_Support\_Structures\_Strategies\_based\_on\_the Dynamic Substructuring Paradigm.
- [31] S. Voormeeren, P. van der Valk, and D.J. Rixen. Practical aspects of dynamic substructuring in wind turbine engineering. Structural Dynamics and Renewable Energy, 1:163-185, 2011. URL: https://www.researchgate.net/publication/227134717\_Practical\_Aspects\_of\_Dynamic\_Substructuring\_in\_Wind\_Turbine\_Engineering.



### **Construction of Boolean Matrix**

This part of the Appendix demonstrates an example on how to obtain the Boolean matrix at the interface of two substructures. The Boolean matrix was introduced in section 2.2.2

This example is entirely presented from and referred to [4]. Consider a system with two substructures as shown below. In total, each substructure consists of 3 nodes but only 2 out of those 3 nodes interact at the interface during coupling.

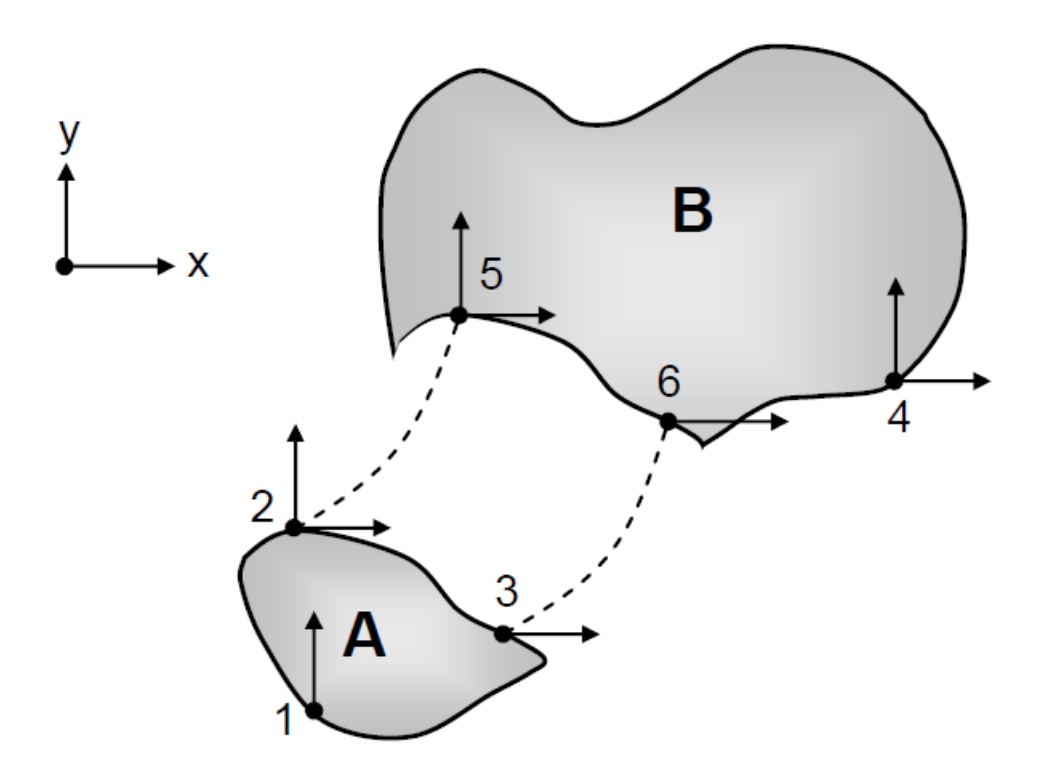


Figure A.1: Coupling of two substructures [31]

Substructure A has 4 DoFs in total while substructure B has 5 DoFs totally. During assembly, nodes 2 couples with node 5 and node 3 with node 6. Hence, three compatibility conditions should be satisfied .

$$u_{2x} = u_{5x}$$
 (A.1)

$$u_{2y} = u_{5y}$$
 (A.2)

$$u_{3x} = u_{6x} \tag{A.3}$$

In order to compute the signed Boolean matrix to include in the equation (1.3), Bu = 0, first consider the vector containing all the DoFs of the system. It is given by the vector:

$$u = \begin{bmatrix} u_{1y} & u_{2x} & u_{2y} & u_{3x} & u_{4x} & u_{4y} & u_{5x} & u_{5y} & u_{6x} \end{bmatrix}^T$$
 (A.4)

Based on the coefficients in (A.1) in the form of  $u_1 - u_2 = 0$ , the signed Boolean matrix is formed as :

$$B = \begin{bmatrix} 0 & 1 & 0 & 0 & 0 & 0 & -1 & 0 & 0 \\ 0 & 0 & 1 & 0 & 0 & 0 & 0 & -1 & 0 \\ 0 & 0 & 0 & 1 & 0 & 0 & 0 & 0 & -1 \end{bmatrix}$$
 (A.5)

It is evident from (A.5) that every coupling term or compatibility equation in (A.1) corresponds to a row in the Boolean matrix. The order of this matrix for a system with m interface DoFs and n system DoFs can be generally represented as mxn.



# Impulse Response Model

This section discusses the development of the Impulse Response model based on the concepts explained in the previous chapter. It further highlights the application of IBS concept to OWTs where the tower and RNA are characterized by impulse response and Newmark methods respectively. The IBS method is carried out for the linear case as shown in figure B.1.The work presented here is based on [28].

The primary step begins with the equations of motion of the two substructures, namely the tower in terms of its IRF and the entire RNA in its linearized form. It is known that the IRFs depend on the initial conditions discussed earlier and therefore the Initial Applied Force approach is considered for which the IRF is represented by equation (B.1). The RNA is denoted with superscript rna and the tower is denoted with superscript sub. Additionally, the Compatibility equation (2.3) and Equilibrium condition (2.5) are incorporated in order to assemble the equations of motion and the resulting equations are:

$$\begin{cases} u_n^{(sub)} = \frac{dt}{2} \sum_{i=0}^{n-1} H_{n-i}^{(sub)} \left( f_i^{(sub)} + f_{i+1}^{(sub)} - B^{(sub)^T} \left( \lambda_i + \lambda_{i+1} \right) \right) \\ M^{(rna)} \ddot{u}^{(rna)} + C^{(rna)} \dot{u}^{(rna)} + K^{(rna)} u^{(rna)} = f_n^{(rna)} - B^{(rna)^T} \lambda_n \end{cases}$$
(B.2)

$$M^{(rna)}\ddot{u}^{(rna)} + C^{(rna)}\dot{u}^{(rna)} + K^{(rna)}u^{(rna)} = f_n^{(rna)} - B^{(rna)^T}\lambda_n$$
 (B.2)

$$Bu_n = 0 (B.3)$$

Before moving to the solution of the coupled problem, the uncoupled response of both the substructures should be obtained. For the RNA, this is done using equations (C.2) and (C.3) where the acceleration is determined from equation (C.9).Due to the introduction of interface force  $\lambda_n$  in this case, equation (C.9) is modified to:

$$S^{(rna)}\dot{u}_{n}^{(rna)} = f_{n}^{(rna)} - B^{(rna)^{T}}\lambda_{n} - C^{(rna)}\dot{u}^{(rna)} - K^{(rna)}u^{(T)}$$
(B.4)

$$\Rightarrow \ddot{u}_{n}^{(rna)} = S^{(rna)^{-1}} \left( f_{n}^{(rna)} - B^{(rna)^{T}} \lambda_{n} - C^{(rna)} \hat{u}_{n}^{(rna)} - K^{(rna)} \hat{u}_{n}^{(rna)} \right)$$
(B.5)

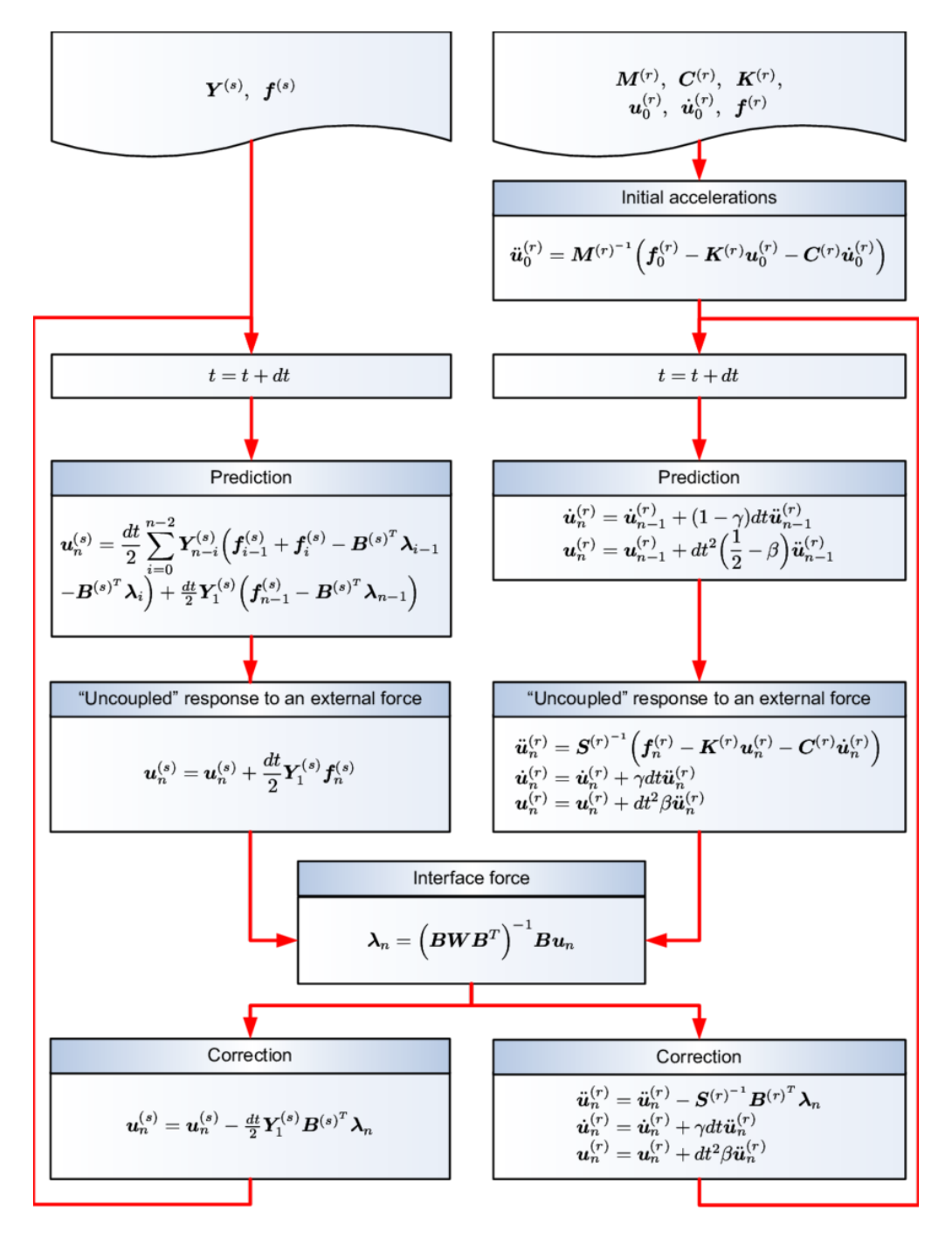


Figure B.1: Impulse Response model algorithm [28]

Solving equation (C.9) and substituting in (C.3) results in the following expression for computing displacements :

$$u_n^{(rna)} = \tilde{u}_n^{(rna)} - \beta dt^2 S^{(rna)^{-1}} B^{(rna)^T} \lambda_n$$
 (B.6)

where,

$$\tilde{u}_{n}^{(rna)} = \hat{u}_{n}^{(rna)} + \beta dt^{2} S^{(rna)^{-1}} \left( f_{n}^{(rna)} - C^{(rna)} \hat{u}_{n}^{(rna)} - K^{(rna)} \hat{u}_{n}^{(rna)} \right) \tag{B.7}$$

Similarly, the uncoupled response of the tower is obtained using the discretized formulation of Duhamel's integral as discussed in section 2.4.1. Recalling equation (B.1) and rearranging to obtain an expression similar in form to equation B.6:

$$u_n^{(sub)} = \tilde{u}_n^{(sub)} - \frac{dt}{2} H_1^{(sub)} B^{(sub)^T} \lambda_n$$
(B.8)

where, predictor  $\tilde{u}_n^{(S)}$  is represented by :

$$\tilde{u}_{n}^{(sub)} = \frac{dt}{2} \sum_{i=0}^{n-2} H_{n-i}^{(sub)} \left( f_{i}^{(sub)} + f_{i+1}^{(sub)} - B^{(sub)^{T}} \left( \lambda_{i} + \lambda_{i+1} \right) \right) + \frac{dt}{2} H_{1} \left( f_{n-1}^{(sub)} + f_{n}^{(sub)} - B^{(sub)^{T}} \lambda_{n-1} \right)$$
(B.9)

As stated earlier, all the terms in a predictor are known beforehand and are therefore easily recalled or calculated. Eventually, the only unknowns that still remain in equations (B.6) and (B.8) are  $u_n^{(rna)}$ ,  $u_n^{(sub)}$  and  $\lambda_n$ . Looking back at the compatibility condition which states that the displacements at the interface are equal, the above mentioned equations are substituted in the Compatibility condition (2.3). This leads to the calculation of the forces occurring at the interface at the current time step, in the form of :

$$\lambda_n = (BWB^T)^{-1}B\tilde{u}_n \tag{B.10}$$

where,

$$W = \begin{bmatrix} \frac{dt}{2} H_1^{(sub)} & 0\\ 0 & \beta dt^2 S^{(rna)^{-1}} \end{bmatrix}$$
 (B.11)

Equation (B.10) gives the interface force of the coupled model and is substituted in equations (3.8), (3.6) and (C.2) to get the final displacements, velocities and accelerations at time  $t_n$  which serve as the input for analyzing the coupled response at the next time step  $t_{n+1}$ .



# Time Integration using Newmark Method

The Newmark Time Integration method is a one-step integration method which was originally introduced by N.M.Newmark in the year 1959. It was developed with the aim to analyze both linear and non-linear second-order systems in the field of structural dynamics. It establishes a relation that allows for the evaluation of displacement and velocity in terms of acceleration by applying Taylor expansion to the state vector at a given time step, for which the general expression is shown below:

$$f(t_{n+1}) = f(t_n) + hf'(t_n) + \frac{h^2}{2}f''(t_n) + \dots + \frac{h^s}{s!}f^{(s)}(t_n) + R_s$$
 (C.1)

Where  $R_s$  is the remainder of the development to the order s. To summarize equation (C.1), it uses the known state vector at the current time  $t_n$  to calculate the state vector at the further time instances  $t_{n+dt}$ , where dt denotes time interval between two subsequent time steps. Therefore, for smaller time interval values, more accurate results are obtained. Note that in this research, the displacement, velocity and acceleration are denoted by  $u_n$ ,  $\dot{u}_n$  and  $\ddot{u}_n$  respectively instead of  $q_n$ ,  $\dot{q}_n$  and  $\ddot{q}_n$  as shown in [10]. This becomes more clear when assuming n = n-1, then the expressions for velocity and displacement in terms of acceleration at time  $t_n$  becomes :

$$\dot{u}_n = \dot{u}_{n-1} + (1 - \gamma)dt\ddot{u}_{n-1} + \gamma dt\ddot{u}_n$$
 (C.2)

$$u_n = u_{n-1} + dt\dot{u}_{n-1} + \left(\frac{1}{2} - \beta\right)dt^2\ddot{u}_{n-1} + \beta dt^2\ddot{u}_n \tag{C.3}$$

where the  $\gamma$  and  $\beta$  parameters are constants which are associated with the numerical quadrature scheme and determine the stability of the solution [10]. The values of these parameters vary based on the algorithm that is being employed in the Newmark scheme as shown in Table C.1.

Algorithm	γ	β	Stability Limit	Numerical Damping Ratio	periodicity error $\frac{\Delta T}{T}$
Purely explicit	0	0	0	$-\omega h/4$	-
Central Difference	1/2	0	2	0	$-\frac{\omega^2 h^2}{24}$
Fox & Goodwin	1/2	1/12	2.45	0	$O(\omega^4 h^4)$
Linear Acceleration	1/2	1/6	3.46	0	$\frac{\omega^2 h^2}{24}$
Constant Average Acceleration	1/2	1/4	∞	0	$\frac{-\omega^2 h^2}{12}$
Constant Average Acceleration (with damping)	1/2 + α	$\frac{(1+\alpha)^2}{4}$	8	$\frac{\alpha}{2}\omega h$	$\left(\frac{1}{12} + \frac{\alpha^2}{4}\right) \omega^2 h^2$

Table C.1: Newmark Family of Methods [10]

Of these methods, all algorithms excluding Fox & Goodwin and Linear acceleration are mainly used in structural dynamics to compute the response of the system. The Purely Explicit and Central Difference methods are applied to non-linear systems in combination with Constant Average Acceleration method which is employed for linear system. Figure C.1 displays the flow process for linear systems under Newmark scheme where the primary step is the selection of the initial conditions. Based on the displacement and velocity values in these conditions, the initial acceleration is determined from :

$$\ddot{u}_0 = M^{-1}(f_0 - C\dot{u}_0 - Ku_0) \tag{C.4}$$

which arises from the need to ensure that dynamic equilibrium is maintained in the system during the simulation. Once the inputs have been fed, the time integration scheme begins and the displacements, velocities and accelerations are computed for the subsequent time steps or time intervals. Substituting equations (C.2) and (C.3) in the linear equation of motion (2.1) results in the following relation:

$$S\ddot{u}_{n} = f_{n} - C[\dot{u}_{n-1} + (1 - \gamma)dt\ddot{u}_{n-1}] - K[u_{n-1} + dt\dot{u}_{n-1} + \left(\frac{1}{2} - \beta\right)dt^{2}\ddot{u}_{n-1}]$$
 (C.5)

$$S = [M + \gamma dtC + \beta dt^2 K]$$
 (C.6)

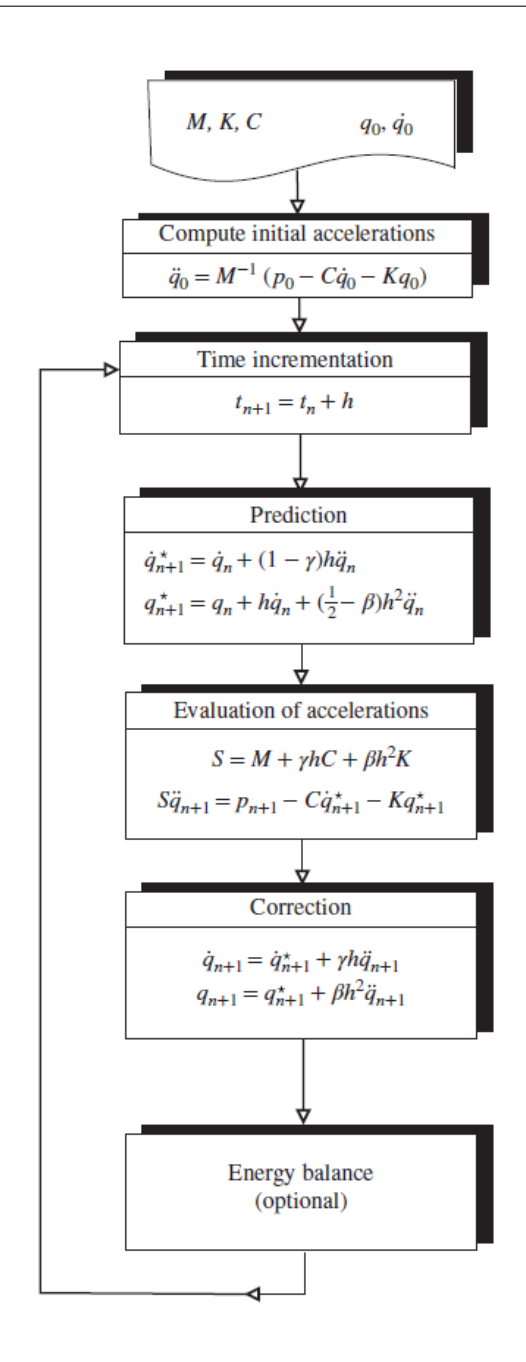


Figure C.1: Newmark scheme for linear systems [22]

The matrix S denotes the factorization matrix which is symmetric and positive definite depending on M,C and K. This matrix has to be factorized only once for the entirety of the simulation and once it has been calculated, the acceleration  $\ddot{u}_n$  that is obtained from equation (C.5) is further used to deduce the velocity and displacements from equations (C.2) and (C.3). The predictor terms  $\hat{u}_n$  and u mentioned under "Prediction" in the flowchart(see fig C.1) constitute all the terms respectively in equations (C.2) and (C.3), except for the final term, i.e.:

$$\hat{u}_n = \dot{u}_{n-1} + (1 - \gamma)dt\ddot{u}_{n-1} \implies \dot{u}_n = \hat{u}_n + \gamma dt\ddot{u}_n \tag{C.7}$$

$$\hat{u}_n = u_{n-1} + dt \dot{u}_{n-1} + \left(\frac{1}{2} - \beta\right) dt^2 \ddot{u}_{n-1} \implies u_n = \hat{u}_n + \beta dt^2 \ddot{u}_n \tag{C.8}$$

Owing to these relations, equation (C.5) is modified to :

$$S\ddot{u}_n = f_n - C\hat{u}_n - K\hat{u}_n \tag{C.9}$$

The predictors are computed from values that are already known and available as a result of the calculation in previous time steps. In the final step, the predicted values are corrected by using the corrected accelerations as applied in equations (2.43) and (2.44).



# **Tower Information**

The NREL 5MW tower file contains 12 nodes and 11 elements. A node is basically a point in space that has 6 DoFs in total, 3 translational DoFs and 3 rotational DoFs. An element connect two given nodes and consists of properties and dimensions based on the type, geometry and material.

Node Number	Node ID	X(m)	Y(m)	Z(m)
0	NFOU0000	0	0	87.600
1	NFOU0001	0	0	85.270
2	NFOU0002	0	0	76.740
3	NFOU0003	0	0	68.210
4	NFOU0004	0	0	58.690
5	NFOU0005	0	0	51.160
6	NFOU0006	0	0	42.630
7	NFOU0007	0	0	34.110
8	NFOU0008	0	0	25.580
9	NFOU0009	0	0	17.050
10	NFOU0010	0	0	8.530
11	NFOU0011	0	0	0.00

Table D.1: List of Nodes - NREL 5MW Tower

Element Number	Element ID	Top Node	Bottom Node	Top node Diame- ter(m)	Bottom node Diam- eter(m)
0	EFOU0000	0	1	3.87	3.87
1	EFOU0001	1	2	3.87	4.08
2	EFOU0002	2	3	4.08	4.30
3	EFOU0003	3	4	4.30	4.51
4	EFOU0004	4	5	4.51	4.72
5	EFOU0005	5	6	4.72	4.94
6	EFOU0006	6	7	4.94	5.15
7	EFOU0007	7	8	5.15	5.36
8	EFOU0008	8	9	5.36	5.57
9	EFOU0009	9	10	5.57	5.79
10	EFOU0010	10	11	5.79	6.00

Table D.2: List of Elements - NREL 5MW Tower

Table D.1 shows the coordinate of each node whereas table D.2 shares information about the nodes that each element connects in addition to the diameter at the two ends of the element.

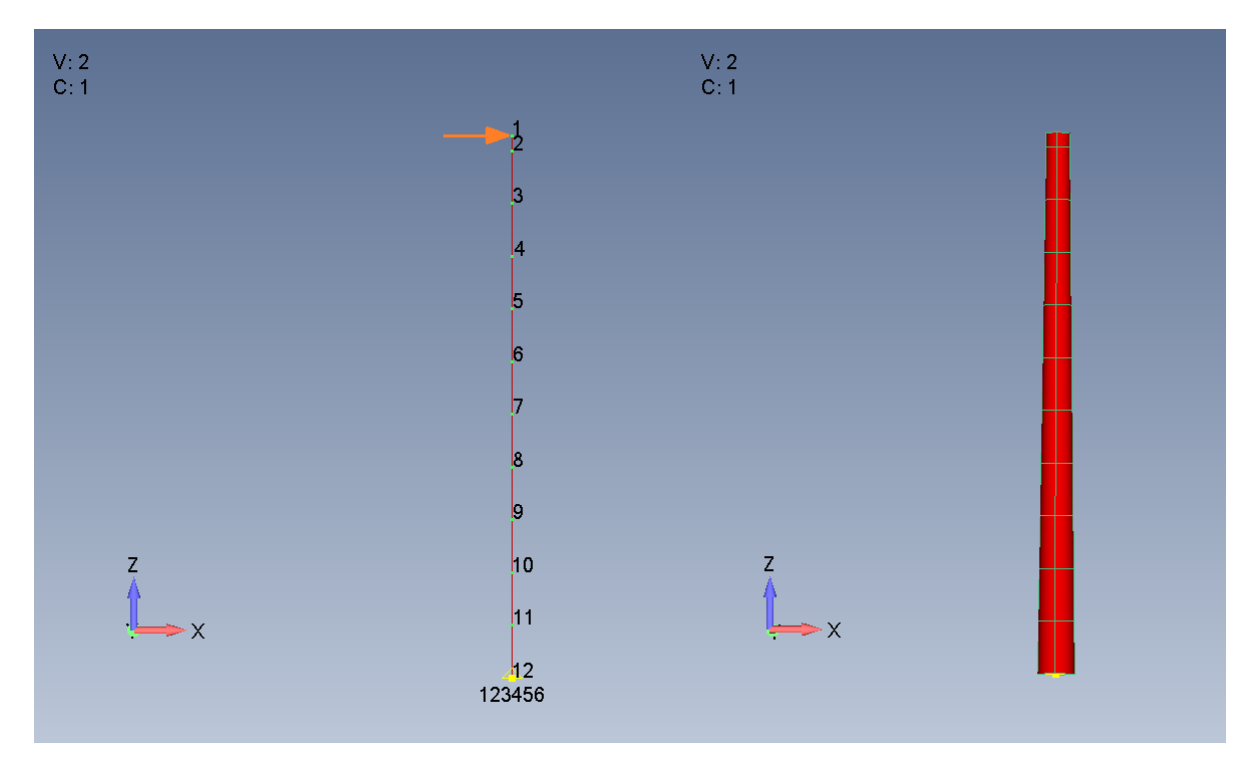


Figure D.1: Finite Element Model - NREL5MW Tower

The information in tables D.1 and D.2 correspond to figure D.1. The reference model named *Vibration Toolbox* was obtained from Github [3]. It is an open-source toolbox that contains multiple functions and can be used to perform modal, frequency and time domain analyses to compute mode shapes, magnitude and phase of the FRFs, and displacements of the structure respectively for both single and multiple degrees of freedom systems.

In order to validate the toolbox, the NREL 5MW tower is modeled in FEMAP and the characteristic mass, stiffness and damping matrices were extracted using Boskalis' in-house tool *PDT*. The above tables share information about the tower structure which is subjected to a random force as shown in figure D.2 at the top node in x-direction (DoF 1). The same setup is replicated using the *Vibration Toolbox* and the outputs from both models were plotted against each other as shown in figure D.3

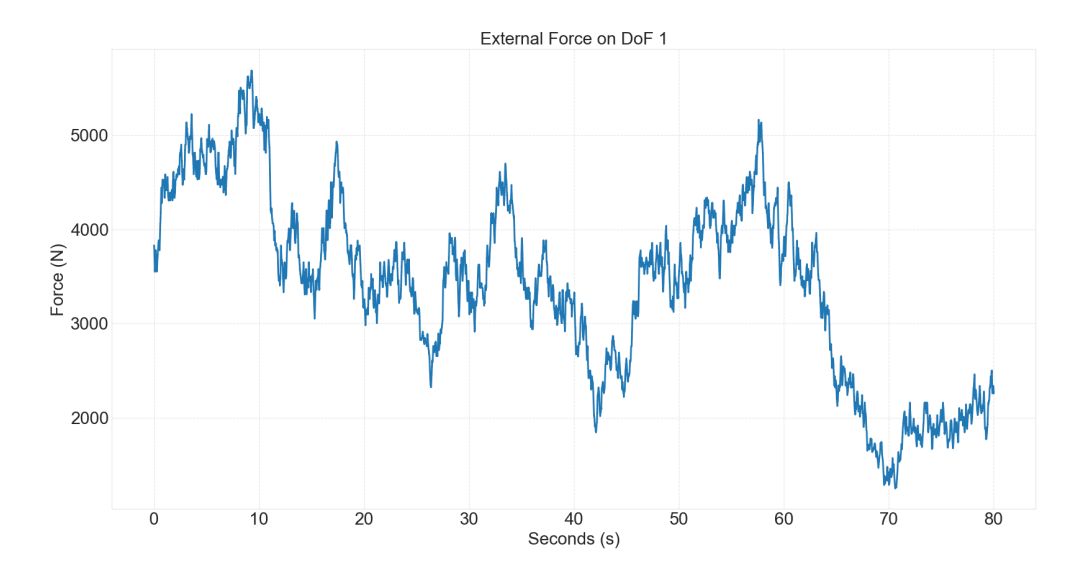


Figure D.2: External Excitation Force

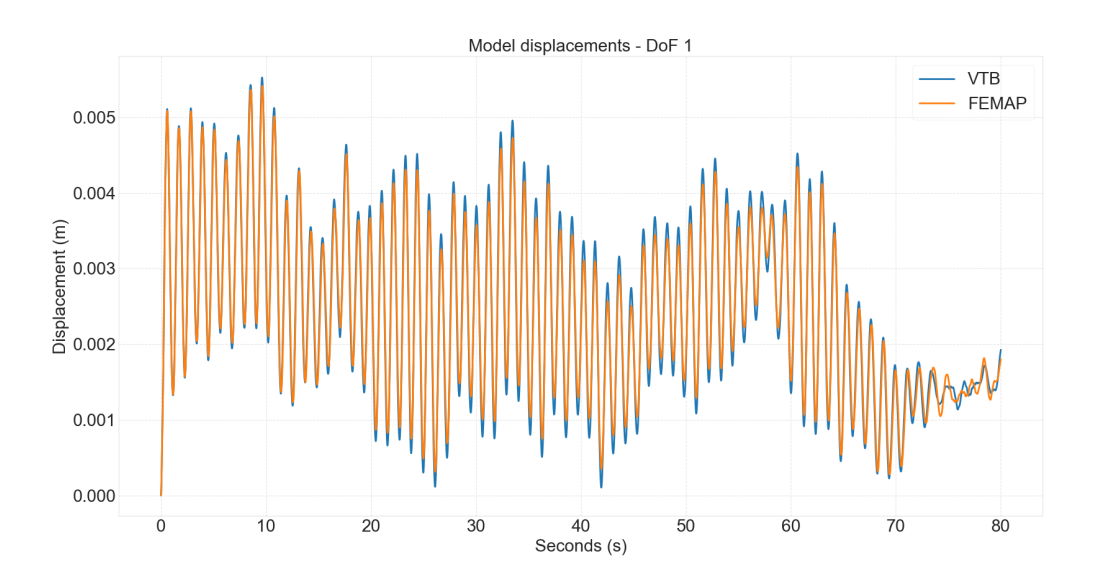
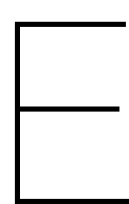


Figure D.3: Displacement at DoF 1

It is clearly evident from figure D.3 that the toolbox produces accurate results that correlate with results produced by FEMAP. The slight overestimation may be accredited to the precision format being used, i.e.rounding off of values after the decimal point. Therefore, based on this observation, the *Vibration Toolbox* is chosen as the reference model and serves as the basis to validate the developed models.



### Structure used for validation

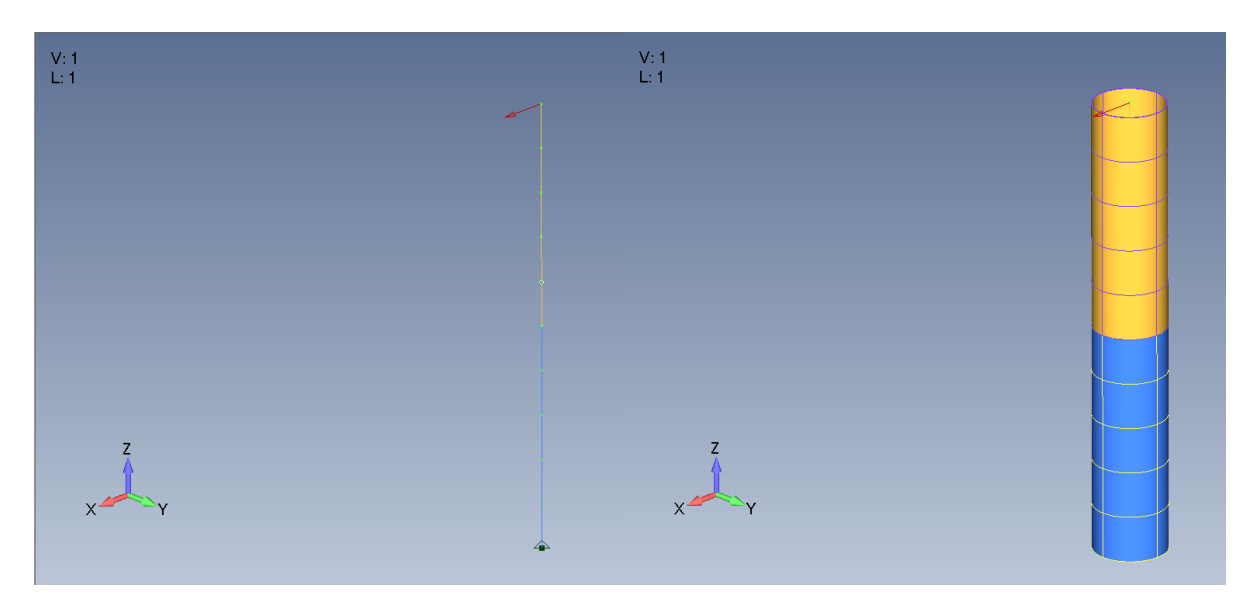


Figure E.1: Finite Element Model - Validation structure

Figure E.1 shows the structure that is used to validate the prediction model discussed in section 4.1. The structure with a uniform diameter of 8 meters consists of 11 nodes in total. The sinusoidal force(*figure E.2* is incident on the first DoF of Node 1(i.e in x-direction corresponding to translation). The final is fixed such that all motions are constrained. The information on the nodes is provided in table E.1. The structure is decoupled at node 5 and therefore, substructure A ends at node 5 and substructure B begins at node 5 as shown in table 4.1.

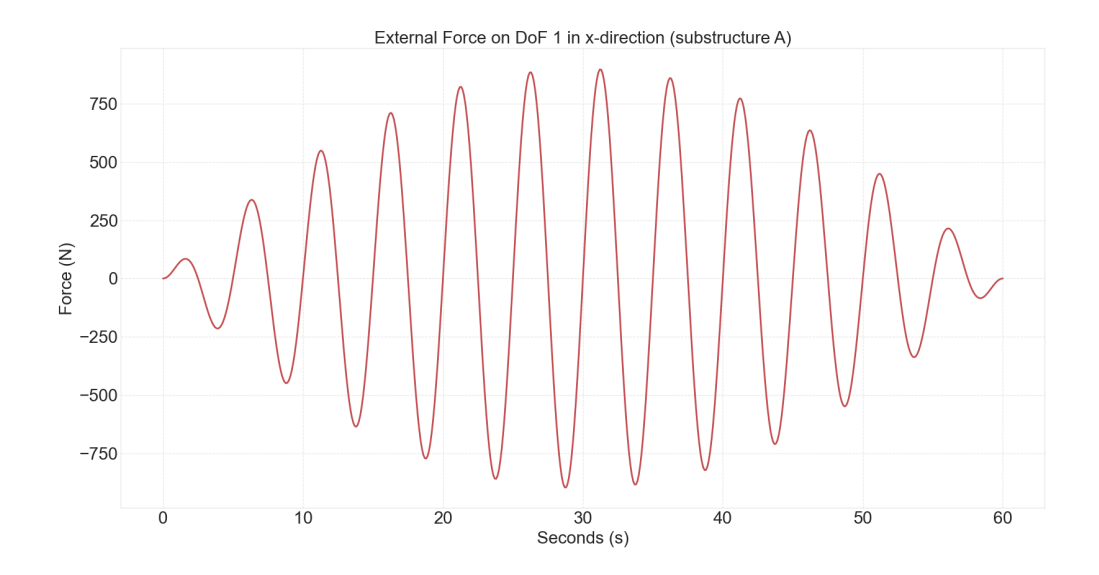
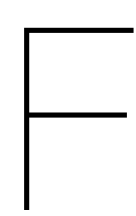


Figure E.2: Sinusoidal excitation force

Node Number	Node ID	X(m)	Y(m)	Z(m)
1	N_FOU_1000	0	0	20.000
2	N_FOU_1001	0	0	15.000
3	N_FOU_1002	0	0	10.000
4	N_FOU_1003	0	0	5.000
5	N_FOU_1004	0	0	0.000
6	N_FOU_1005	0	0	-5.000
7	N_FOU_1006	0	0	-10.000
8	N_FOU_1007	0	0	-15.000
9	N_FOU_1008	0	0	-20.000
10	N_FOU_1009	0	0	-25.000
11	N_FOU_1010	0	0	-30.000

Table E.1: List of Nodes - Hollow Cylinder



### Method for Input Extraction

It is clearly evident from the chapter 3 that the inputs required to run the model include the mass, stiffness and damping matrices of both the RNA and the tower in addition to the external forces incident on them. Since the interest lies in the interface loads at the top, the land configuration of the NREL5MW turbine is chosen for the analyses. Therefore, the objective of this section is to convey the setup and procedure followed in *openFAST* and *PDT* to extract the input parameters related to the rotor-nacelle assembly and tower respectively.

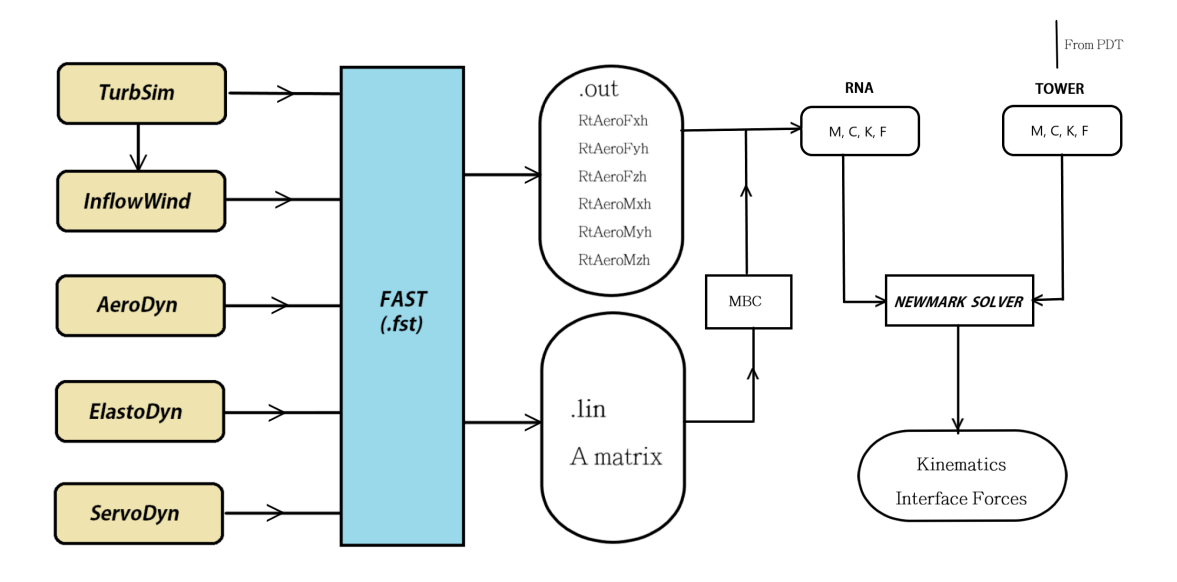


Figure F.1: Process Flowchart

The method followed in this study is condensed in figure F.1 which shows the process flow. In summary, the left side of the flowchart suggests two separate simulations are run in openFAST to extract the inputs of RNA:

- Time domain simulation to obtain the external aeroelastic loads.
- · Linearization to extract matrices of RNA.

#### F.0.1. Extraction of External Aeroelastic Loads

The idea in this step is to extract the external aeroelastic loads on the rotor by performing a non-linear time domain analysis in openFAST for a given wind condition. The analyses are performed at different wind conditions, one of which is the rated condition that refer to the optimal performance of the turbine

and includes parameters such as rated wind speed, rater rotor speed, rated power and rated torque. The rated region for the NREL5MW turbine lies between the rated wind speed of 11.4 m/s and the cut-out wind speed of is 25 m/s on the wind speed spectrum. The cut-in wind speed at which the rotor starts rotating is 3 m/s.

#### (a) TurbSim

The Normal Turbulence Model chosen for this study is generated using TurbSim. It is vital to get the parameters related to the wind field correct in order to avoid any errors during the openFAST simulation. The important parameters that need to be altered are shown in tables F.1. The input file is also set up to produce the required output files to be fed into the InflowWind file. The preferred output format for a turbulent wind field is the .bts format which stands for TurbSim binary file.

Variable	Unit	Description	Value
HubHt	meter	Hub Height of the turbine	84.30
GridHeight	meter	Grid Height	160.0
GridWidth	meter	Grid Width (should be >= 2*(Rotor Radius + shaft length)	160.0
AnalysisTime	seconds	Length of analysis time series	1000
UsableTime	seconds	Length of analysis time series	1000
IECturbC	-	IEC Turbulence characteristic	Α
IEC_WindType	-	IEC turbulence type	NTM
WindProfileType	-	Velocity profile	PL
RefHt	meters	Height of URef	84.30
URef	m/s	Mean wind speed at RefHt	11.4
Z0	meter	surface roughness length	default

Table F.1: TurbSim parameters for a turbulent wind field with an average wind speed of 11.4 m/s

Additionally, table F.1 also establishes some important observations that must be fulfilled:

- The *Grid Height* and *Grid Width* represent the dimensions of the wind field and have to be initialized such that all the blade nodes and tower nodes fall inside the wind field to prevent any errors from occurring during the simulation.
- The *AnalysisTime* has to be atleast 600 seconds and is usually 800 seconds for simulating different wind speeds under Normal Turbulence condition whereas *UsableTime* is the actual length of the time series for which the wind field data is generated. As a result, it is important to always have *Analysis-Time* close to or same as the *UsableTime* in TurbSim. In addition, if *TMax* in the main input(.fst) file is greater than the *UsableTime*, the simulation would fail when coupled with openFAST since it would then exceed the length of the time series for which the wind field data is generated.
- The choice of *IECWindType* varies based on the DLC and this is listed by the International Electrotechnical Commission(IEC) 61400-1 standards which contain the design requirements for offshore and onshore wind turbines that include information on DLCs and turbulence models related to the wind conditions [6, 9].
- The *IECturbc* parameter depends on the wind turbine class which is defined by tubine manufacturer. For hub heights higher than 60 meters, the power law is chosen method to compute the wind speeds

and the surface roughness length varies based on the terrain where the turbine is going to be installed.

#### (b) AeroDyn

Secondly, the necessary settings are updated in AeroDyn module in order to aid with the aerodynamic analysis of each blade node.

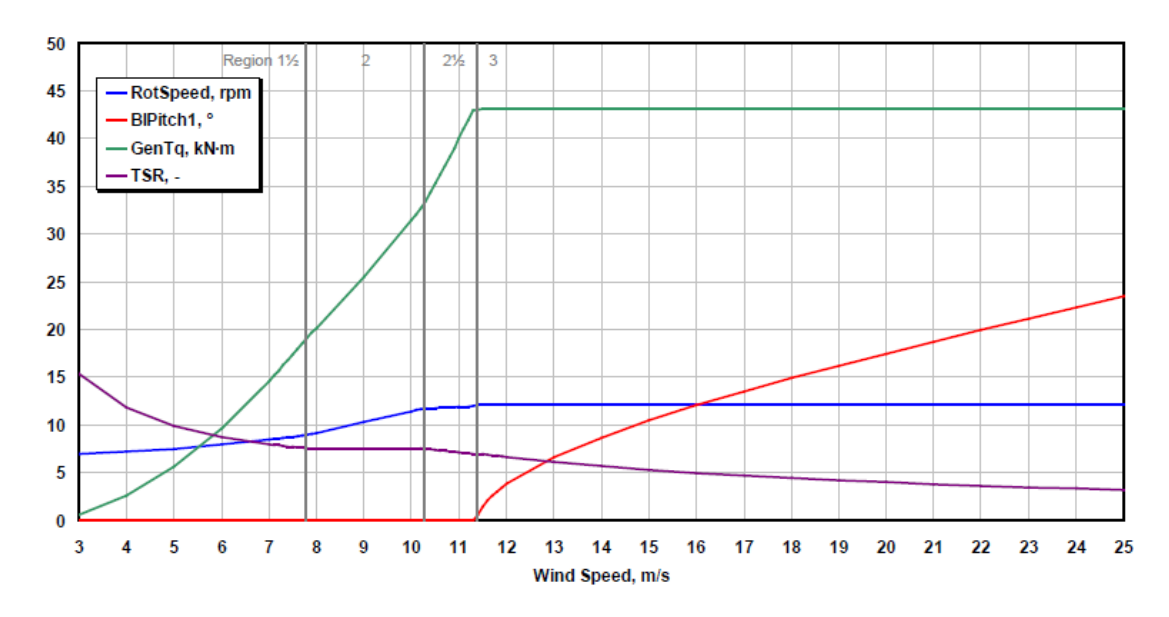


Figure F.2: Generator Torque curve of NREL 5MW turbine [18]

Figure F.2 show the variation of different operation parameters at different wind speeds. The graphs are divided into five regions in total :

- **Region 1**(not shown) is known as the idling region as no power is produced even though the rotor idles at a low speed.
- **Region** 1<sup>1/2</sup> is considered as the transition region as it connects Region 1 with region 2. It consists of the cut-in wind speed at which the power production begins to occur.
- Region 2 is the partial load control region where the goal is to maximise the amount power being produced.
- **Region**  $2^{1/2}$  is again a transition region that connects region 2 with region 3.
- **Region 3** is called the full load region as the turbine reaches its maximum operating potential in this region. The goal is to achieve constant power by pitching the blades to maintain a constant angle of attack. As a result, the rotational speed of the rotor does not exceed its rated value due to which the power, torque and speed related to the rotor and generator remain constant.

#### (c) ElastoDyn

The corresponding *Initial Conditions* related to the average wind speed are set and this includes the rotor speed, the pitch angles and deflection of the blades from figure F.2. This is an important step while simulating for a particular wind speed setting as the wrong initial conditions may cause the blade to hit the tower due to large deflections, eventually causing failure. The blades are pitched at a particular angle above the rated wind speed to prevent the rotor from spinning too fast, i.e.above the rated speed and to alleviate the occurrence of high aerodynamic load levels in the rotor.

(d) **ServoDyn**Finally, the control parameters are declared in the ServoDyn module based on the type of control mechanism chosen.

This resulting output (.out) file contains the rotor aeroelastic loads **RtAeroFxh**, **RtAeroFyh**, **RtAeroMxh**, **RtAeroMyh**, **RtAeroMxh** for the entire time series which serve as the force vector for the prediction model.

#### F.0.2. Extraction of Mass, Stiffness and Damping Matrices of RNA

The second step involves the extraction of second order mass, stiffness and damping matrices from openFAST by linearizing the turbine. This can be directly done in older versions of FAST but the latest versions only give out the mass-generalized stiffness( $M^{-1}K$ ) and mass-generalized damping( $M^{-1}C$ ) matrices contained in the first-order system which makes it slightly complicated as the knowledge of the mass matrix is needed to extract the actual stiffness and damping matrices. The linearization is performed by enabling all or any of the four modules for the land configuration in the main input file. This section explains the linearization setup which is rather straightforward compared to the non-linear time domain simulation.

The settings in each module that enable linearization are mentioned in table F.2:

	InflowWind					
Variable	Unit	Description	Value			
HWindSpeed	m/s	Horizontal wind speed at hub height	11.4			
RefHt	meter	Reference Height	84.30			
PLExp	-	Power Law exponent	0.143			
	AeroDyn					
AFAeroMod	-	Blade airfoil aerodynamics model	1 (steady model)			
	ElastoDyn					
RotSpeed	rpm	Rotor speed	12.1			
BIPitch	degree	Blade pitch angles	0°			
	ServoDyn					
VS_RtGnSp	rpm	Rated generator speed	1173.7			
VS_RtTq	Nm	Rated generator torque/constant generator torque in Region 3	43093.55			
VS_Rgn2K	Nm/(rpm) <sup>2</sup>	Generator torque constant in Region 2	0.0255764			
VS_SIPc	%	Rated generator slip percentage in Region 2 1/2				

Table F.2: Linearization parameters for rated wind speed of 11.4 m/s

- InflowWind: In the case of linearization, the steady wind parameters have to be set in the InflowWind module. This means that any variation in the wind speed is not considered and the wind speed remains constant for the entire time series.
- **AeroDyn**: Since linearization is performed only for steady wind, the UA models are ineffective and therefore have to be disabled by switching to a steady aerodynamics model by setting *AFAeroMod* to **1**.
- ElastoDyn: The ElastoDyn module determines the size of the matrices based on the DoFs that are being enabled. Since the focus is on the RNA, only the DoFs related to the RNA are enabled. This is followed by setting the appropriate initial conditions that are characteristic to the wind speed for which the RNA is being linearized.

• **ServoDyn**: The final module to be altered is related to controls. The pitch and yaw controls are disabled which implies that only drive-train control was considered. A simple variable-speed torque control mechanism was chosen to keep track of the rotor speed once the steady-state has been reached.

The resulting output files contain information about various states, their operating point and state-space matrices. The A matrix is extracted from the output data as it is a square matrix that contains the second order stiffness and damping matrices in the form  $M^{-1}K$  and  $M^{-1}C$  respectively [15].



# Results for other cases

This appendix corresponds to sections 4.2.3, 4.3.1, 4.3.2 and 4.3.3.

### G.1. Case 1.3: Average wind speed 11.40 m/s

In section 4.2.3, the interface loads along y-axis was presented. The interface loads for the remaining degrees of freedom is displayed in this section in addition to the frequency domain representation.

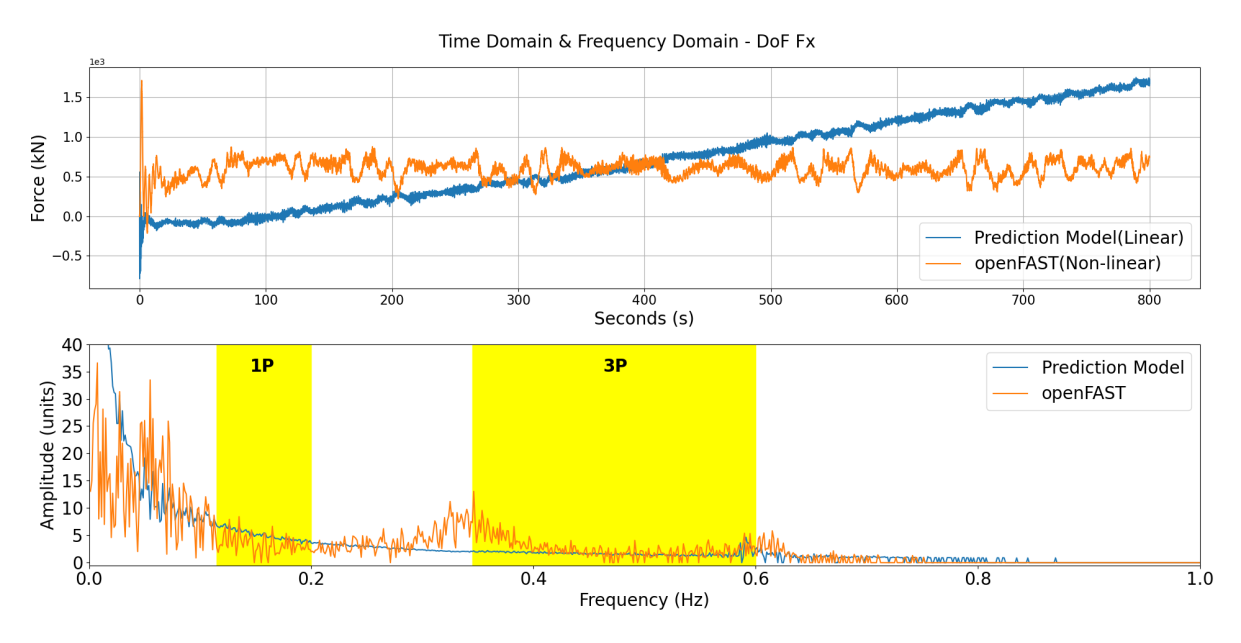


Figure G.1: Time Domain and Frequency Domain - DoF Fx

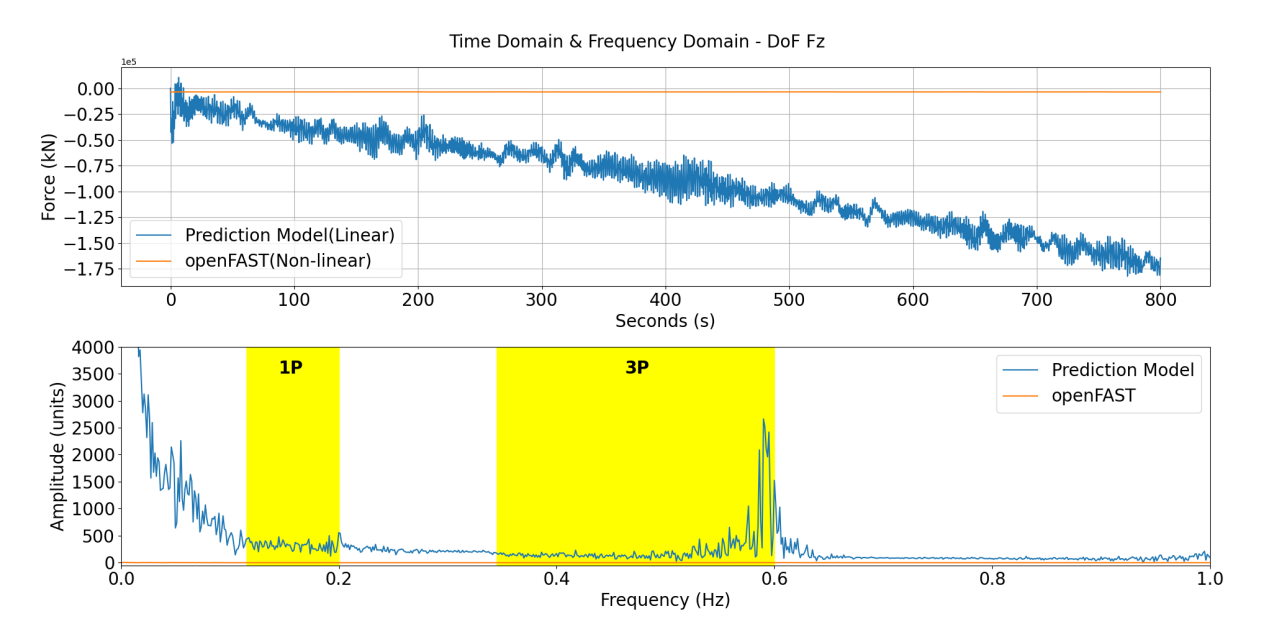


Figure G.2: Time Domain and Frequency Domain - DoF Fz

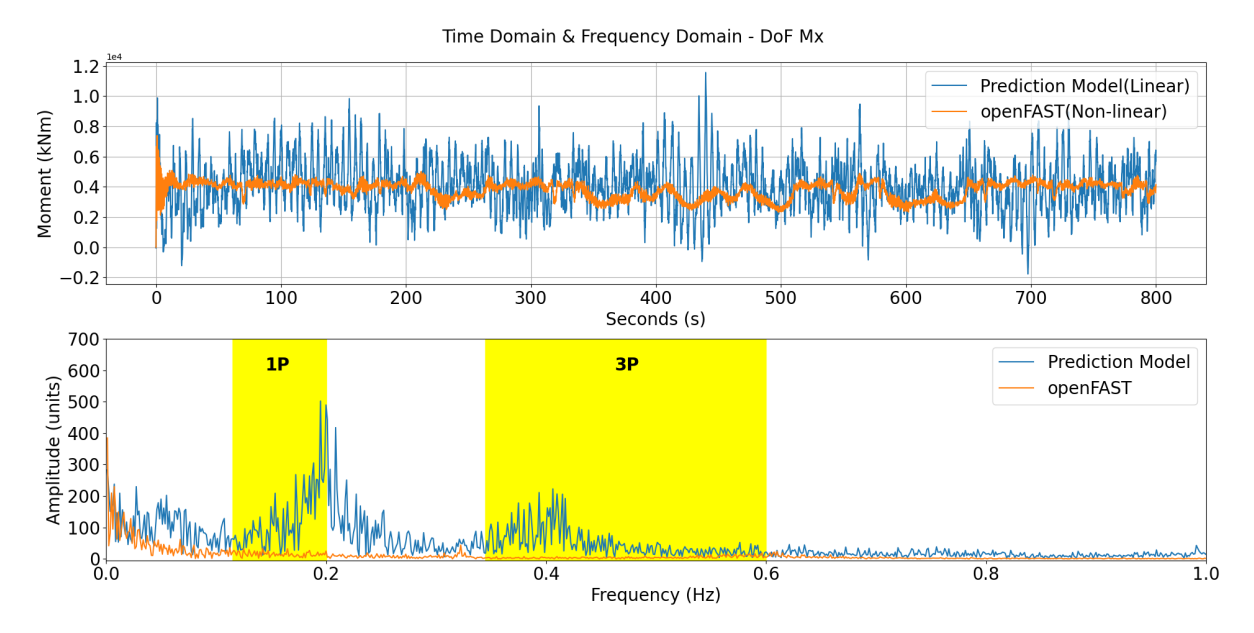


Figure G.3: Time Domain and Frequency Domain - DoF Mx

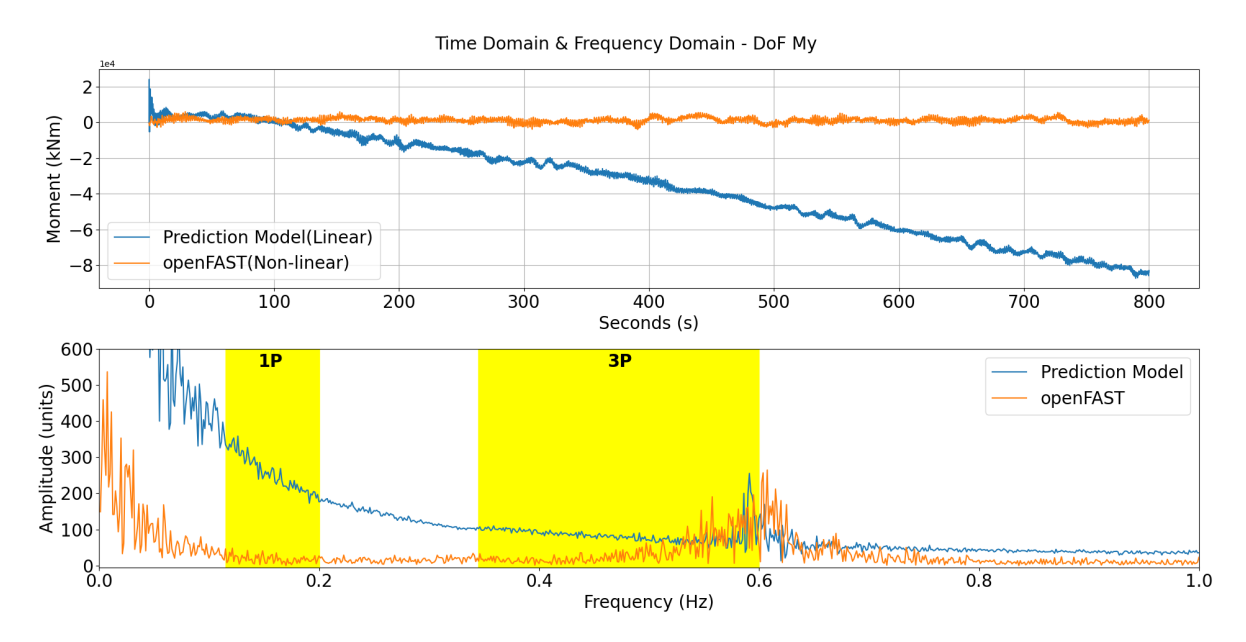


Figure G.4: Time Domain and Frequency Domain - DoF My

### G.2. Case 2.1 : Wind speed 9.32 m/s

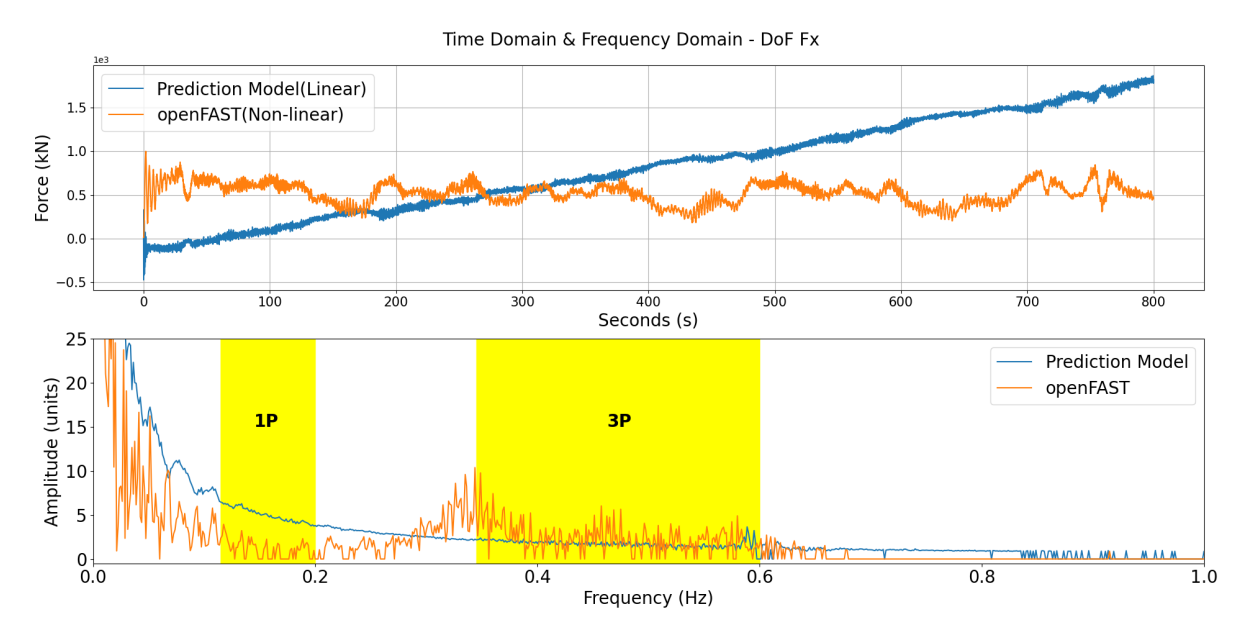


Figure G.5: Time Domain and Frequency Domain - DoF Fx

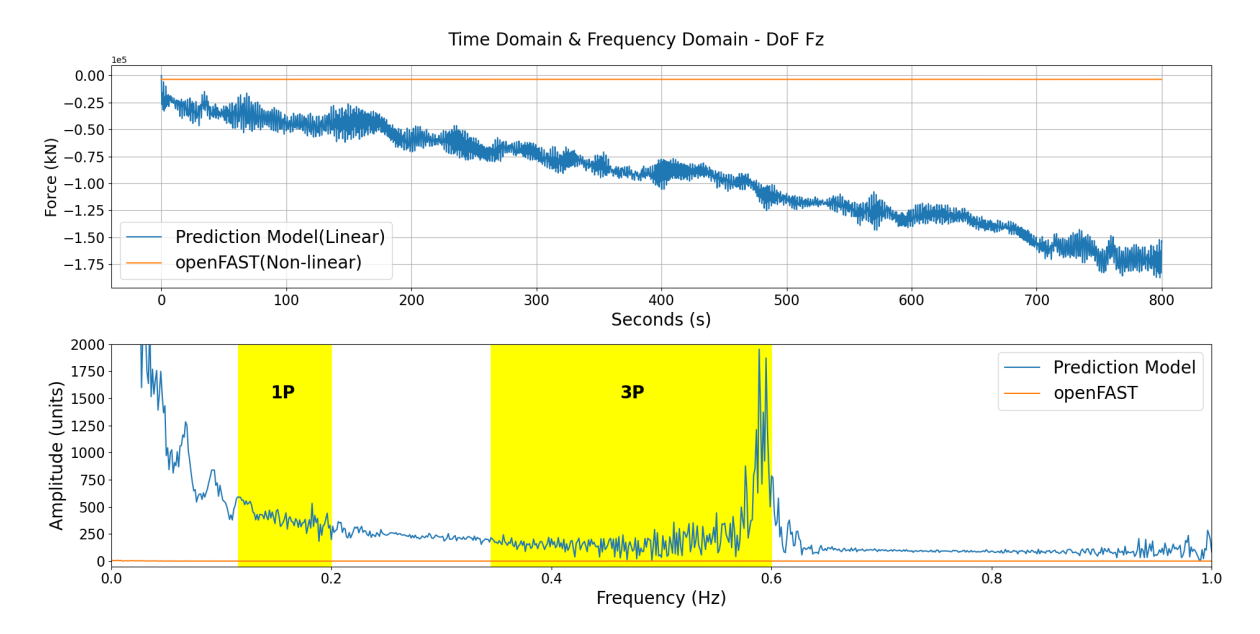


Figure G.6: Time Domain and Frequency Domain - DoF Fz

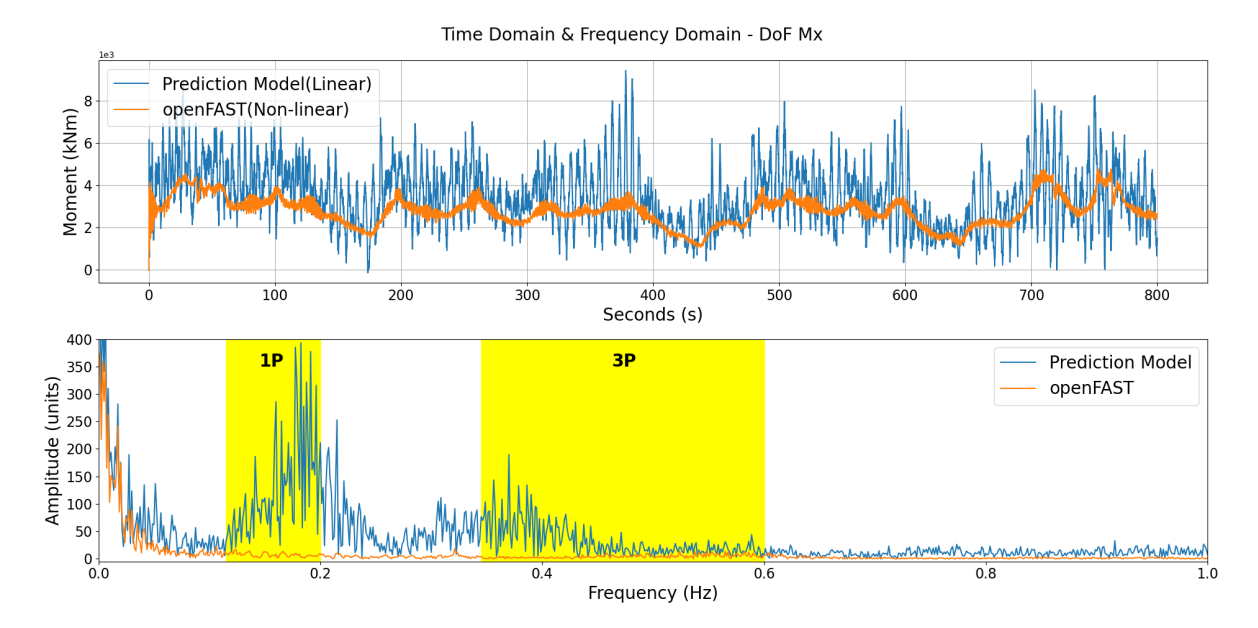


Figure G.7: Time Domain and Frequency Domain - DoF Mx

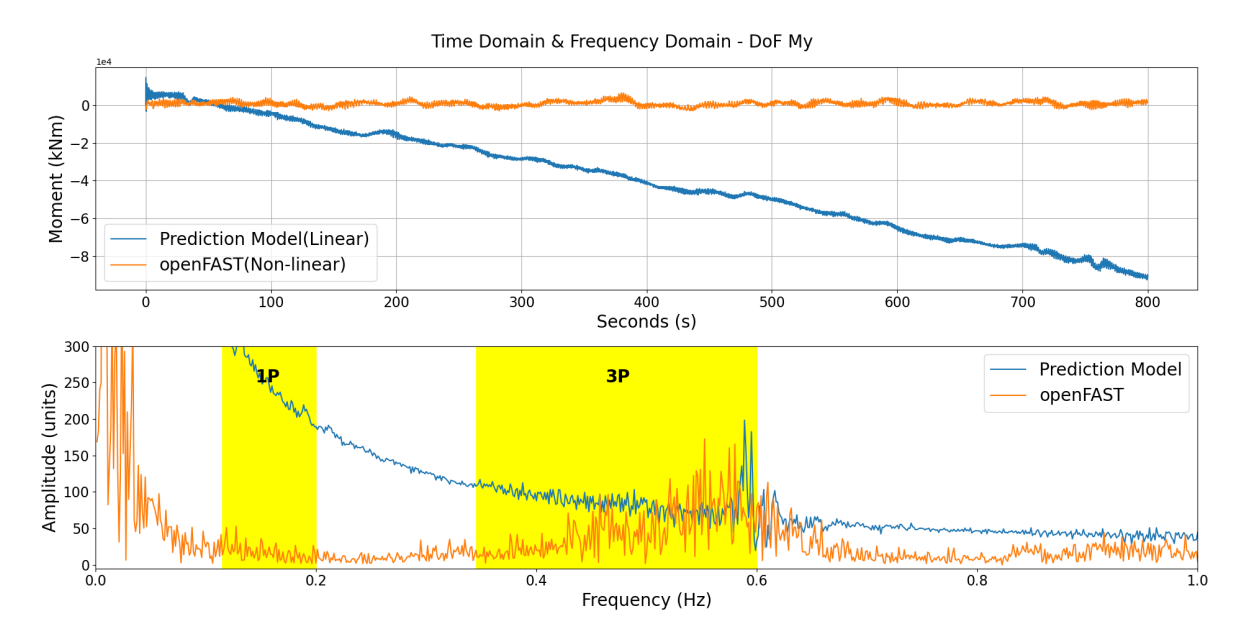


Figure G.8: Time Domain and Frequency Domain - DoF My

### G.3. Case 2.2: Average wind speed 23.64 m/s

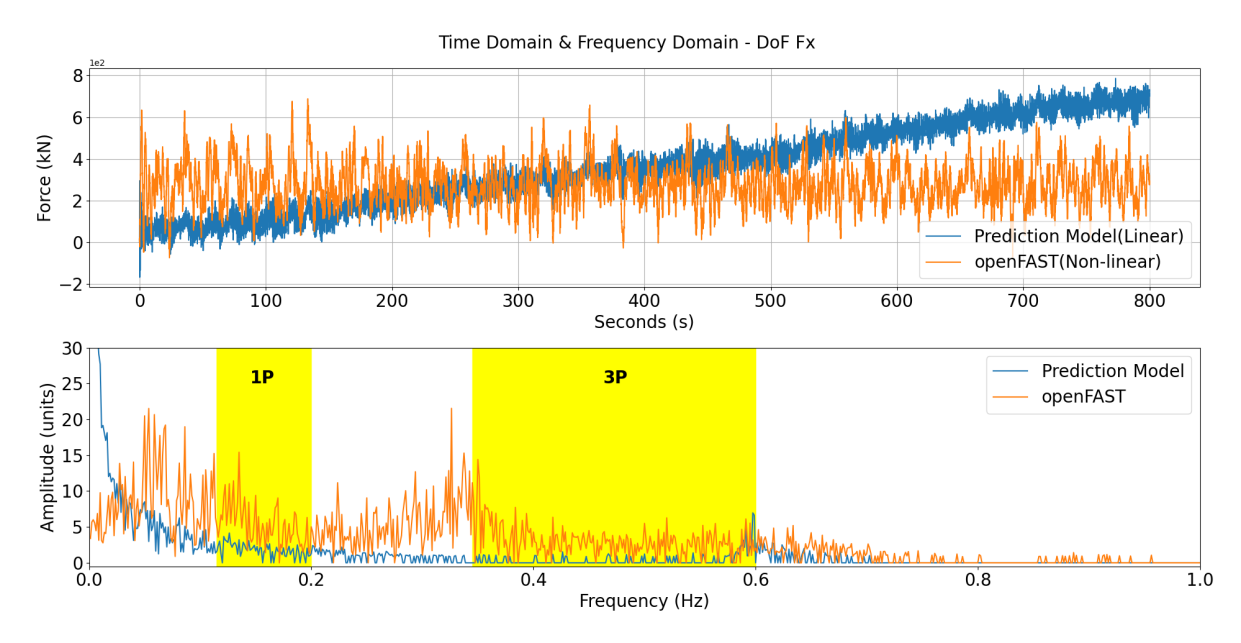


Figure G.9: Time Domain and Frequency Domain - DoF Fx

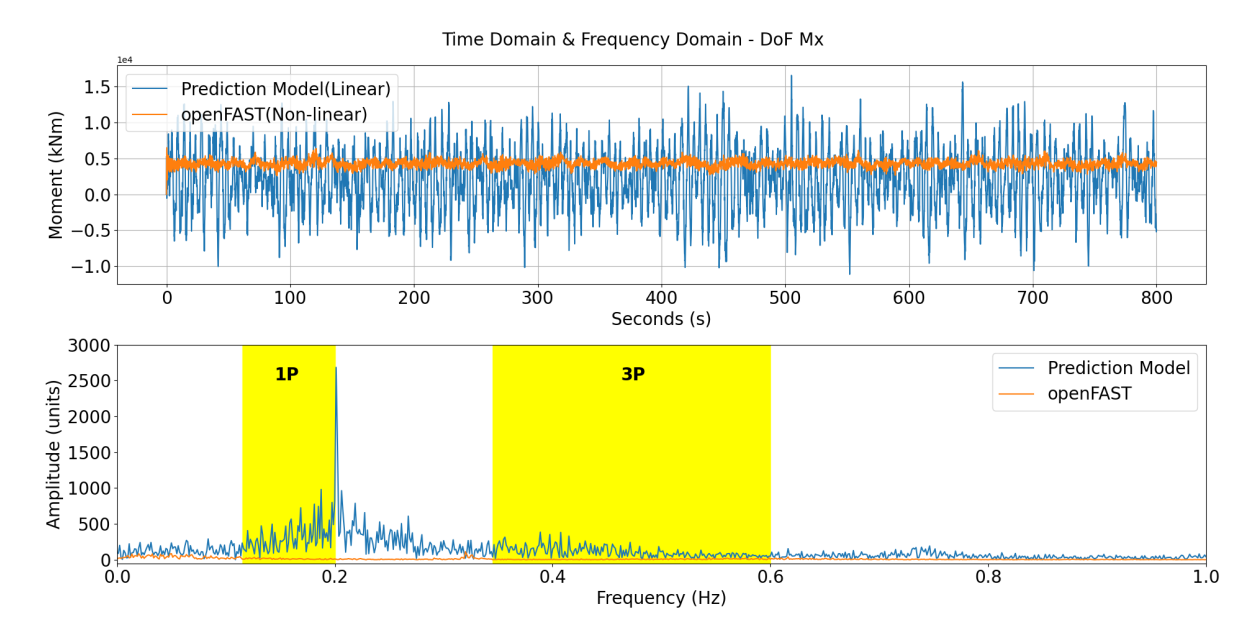


Figure G.10: Time Domain and Frequency Domain - DoF  ${\sf Mx}$ 

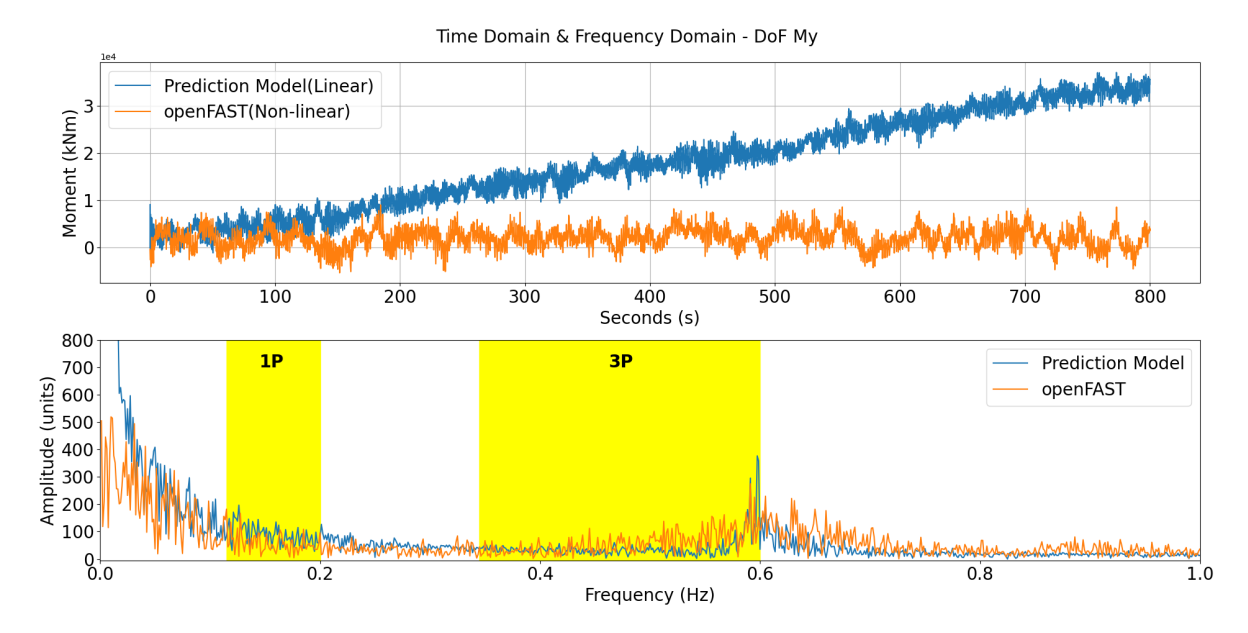


Figure G.11: Time Domain and Frequency Domain - DoF My

### G.4. Case 3.1 : Wind speed 16.40 m/s

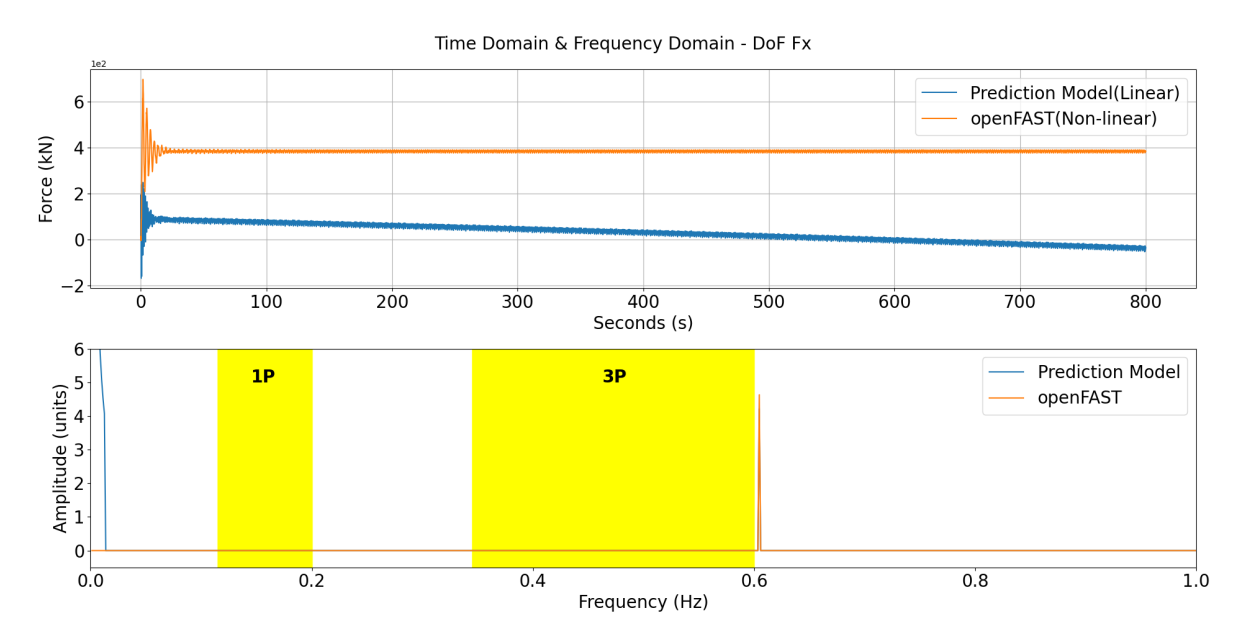


Figure G.12: Time Domain and Frequency Domain - DoF Fx

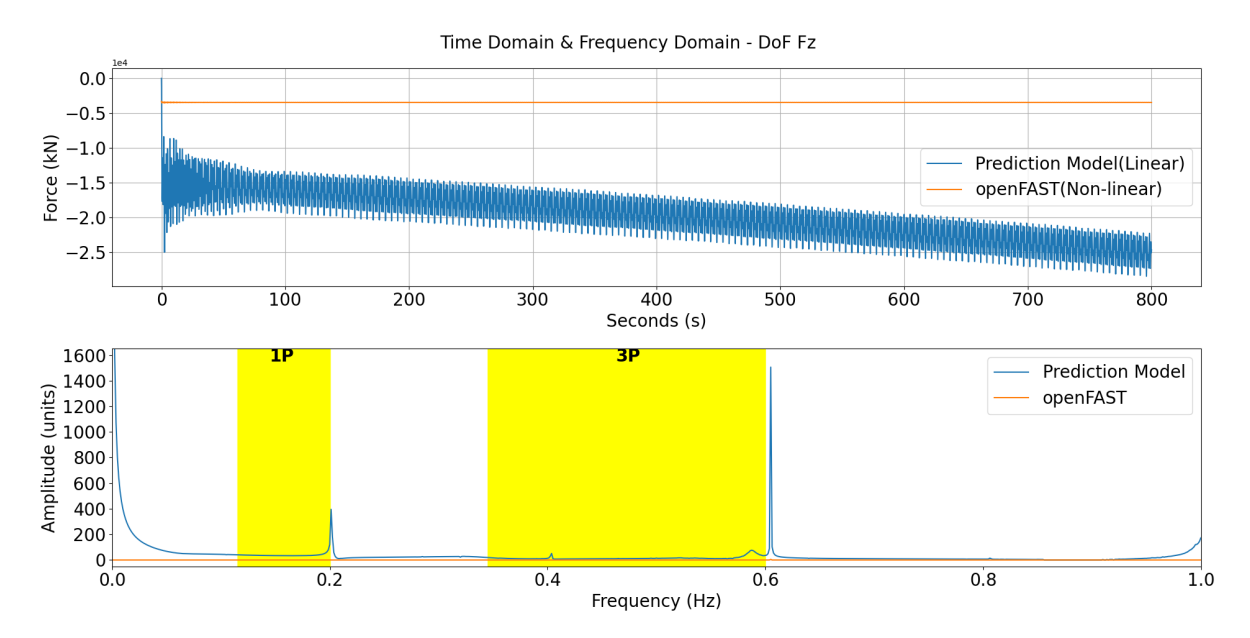


Figure G.13: Time Domain and Frequency Domain - DoF Fz

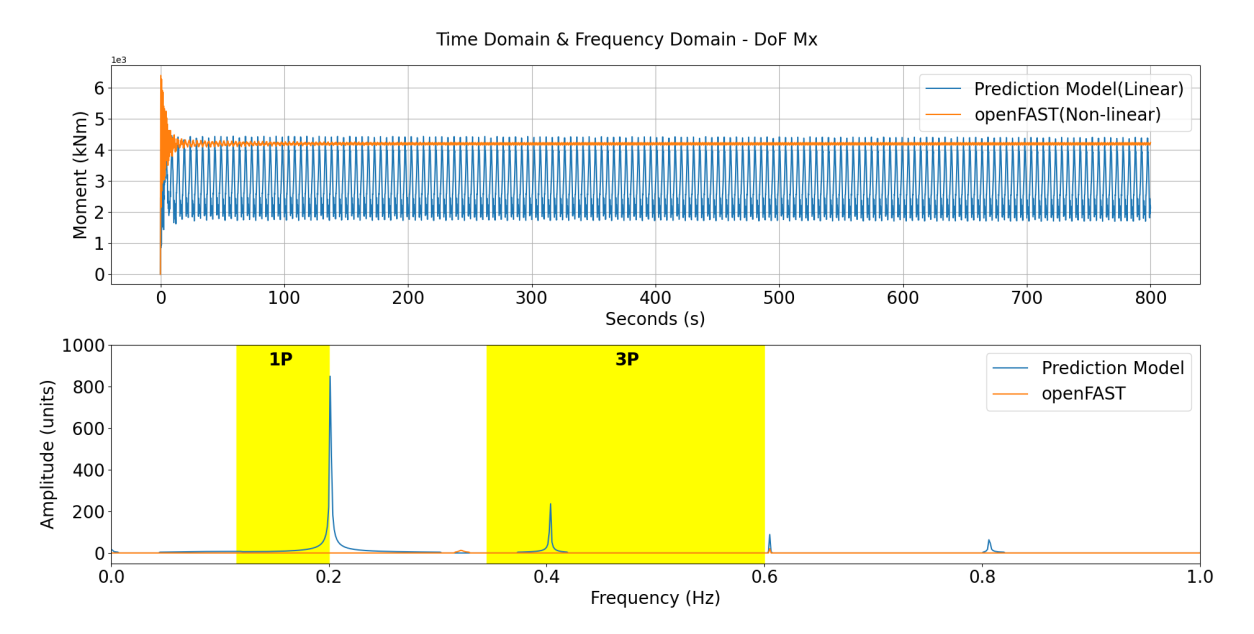


Figure G.14: Time Domain and Frequency Domain - DoF Mx

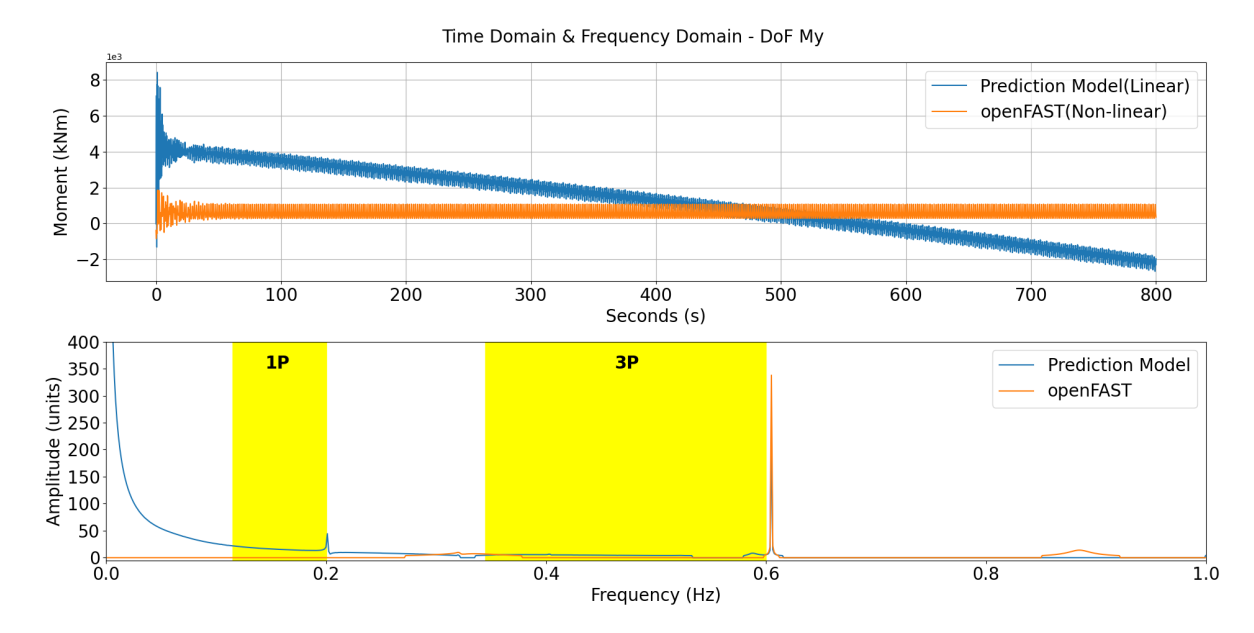


Figure G.15: Time Domain and Frequency Domain - DoF My